Ferroptosis spreads to neighboring cells via plasma membrane contacts

Inaugural-Dissertation

zur

Erlangung des Doktorgrades

der Mathematisch-Naturwissenschaftlichen Fakultät

der Universität zu Köln

vorgelegt von

Bernhard Röck

aus Zams/Österreich

Köln

2024

Berichterstatter:	Prof. Dr. Ana J. Garcia-Saez
(Gutachter)	Prof. Dr. Hamid Kashkar

Tag der mündlichen Prüfung: 31.10.2024

Hierbei handelt es sich um eine von der Mathematisch-Naturwissenschaftlichen Fakultät der Universität zu Köln im Jahr 2024 angenommene Dissertation.

Die vorliegende Arbeit wurde in Nature Communications publiziert:
Roeck, B.F., Lotfipour Nasudivar, S., Vorndran, M.R.H. et al. Ferroptosis spreads to neighboring cells via plasma membrane contacts. Nat Commun 16, 2951 (2025). https://doi.org/10.1038/s41467-025-58175-w

Abstract

Ferroptosis is a regulated cell death modality dependent on iron and characterized by excessive lipid peroxidation, which is affiliated with the spread of necrosis in diseased tissue by undetermined mechanisms. Through the exploitation of the temporal and spatial properties of a novel optogenetic approach that triggers ferroptosis by degrading the anti-ferroptotic enzyme GPX4, we showed that lipid peroxidation and ferroptotic cell death can spread to neighboring cells via their closely connected plasma membranes. We found that ferroptosis propagation depends on the proximity of cells that can be entirely halted by either disrupting α-catenin-dependent intercellular junctions or chelating extracellular iron. Strikingly, linking cells through a lipid bilayer or enhancing the contact area between adjacent cells facilitates ferroptosis spread. We uncovered that iron-dependent lipid peroxidation could be transmitted between directly contacting liposomes, revealing the involvement of a physicochemical mechanism. Our findings indicate that iron-dependent lipid peroxidation propagation occurs across adjacent plasma membranes of neighboring cells, contributing to ferroptotic cell death and subsequent necrosis spread in diseased tissues.

Zusammenfassung

Ferroptose ist eine regulierte Zelltodart, welche von Eisen abhängig ist und durch exzessive Lipidperoxidation gekennzeichnet ist. Sie steht im Zusammenhang mit der Nekroseausbreitung in erkranktem Gewebe durch noch unbekannte Mechanismen. Durch die Nutzung der zeitlichen und räumlichen Eigenschaften eines neuartigen optogenetischen Ansatzes, der Ferroptose durch den Abbau des anti-ferroptotischen Enzyms GPX4 auslöst, konnten wir zeigen, dass sich Lipidperoxidation und ferroptotischer Zelltod über Plasmamembrankontaktflächen auf benachbarte Zellen ausbreiten können. Wir fanden heraus, dass die Ferroptoseausbreitung von der Distanz zwischen Zellen abhängt, welche vollständig gestoppt werden kann, indem entweder α-Catenin-abhängige Zellverbindungen unterbunden oder extrazelluläres Eisen chelatisiert wird. Bemerkenswerterweise erleichtert das Verbinden von Zellen durch eine Lipiddoppelschicht oder die Vergrößerung der Kontaktfläche zwischen benachbarten Zellen die Ferroptoseausbreitung. Wir entdeckten, dass eisenabhängige Lipidperoxidation zwischen direkt in Kontakt stehenden Liposomen übertragen werden kann, was auf einen physikochemischen Mechanismus hinweist. Unsere Ergebnisse deuten darauf hin, dass die Ausbreitung der eisenabhängigen Lipidperoxidation über benachbarte Plasmamembranen erfolgt, was zum ferroptotischen Zelltod und zur anschließenden Nekroseausbreitung in erkranktem Gewebe beiträgt.

Acknowledgments

Completing this Ph.D. thesis has been a challenging yet rewarding journey, and I am deeply grateful for the support and encouragement I have received along the way.

First and foremost, I would like to express my sincere gratitude to my advisor, Prof. Ana J. Garcia-Saez, for her unwavering guidance, patience, and belief in my abilities. Her insightful advice and constructive feedback have been invaluable in shaping this research and in my growth as a scholar.

I would also like to extend my heartfelt thanks to the members of my TAC committee, Manolis Pasparakis and Hamid Kashkar, for their time, expertise, and thoughtful suggestions that have enriched this work. Your contributions have been crucial in refining and finalizing this thesis.

I am immensely thankful to my colleagues and friends within the AG Garcia for creating a collaborative and supportive environment. The stimulating discussions, shared frustrations, and collective moments of success have made this journey a memorable one.

My deepest appreciation goes to my family, particularly my parents and Andrea Ujevic, for their unconditional love, encouragement, and understanding. Their constant support has been my anchor throughout the highs and lows of this process.

To all those mentioned and the many others who have helped me along this path, I offer my sincere thanks.

Contents

List of Figures

List of Tables

List of abbreviations

PUFA – Poly unsaturated fatty acids

Fer-1- Ferrostatin-1

GPX4 – Glutathione peroxidase 4

NINJ1 – Ninjurin 1

LIP-1 - Liproxstatin-1

ROS – Reactive oxygen species

Ca^{2+} - Calcium

Na^{+} - Sodium

TRP - Transient receptor potential channel

H2O2 – Hydrogen-Peroxide

LOX - Lipoxygenase

COX - Cyclooxygenase

ESCRT-III - endosomal sorting complexes required for transport

GSH – Glutathione

LRP8 - Low-density lipoprotein receptor-related protein 8

FSP1 - Ferroptosis suppressor protein 1

ACSL4 - Long-chain-fatty-acid—CoA ligase 4

CoQH - Ubiquinol

IRP1 - Iron regulatory proteins 1

TFRC – Transferrin receptor 1

MFRN1 - Mitoferrin-1

YAP - Yes-associated protein 1

PAF - Platelet-activating factor

ChR - Channelrhodopsin

Cry2 – Cryptochrome 2

PhoCl – Photocleavable protein

LOV domain - Light-oxygen-voltage-sensing domain

AsLOV2 - Avena sativa LOV2

CIB1/CIBN - Cryptochrome-interacting basic-helix-loop-helix/ cryptochrome interacting basic helix-loop-helix protein, N-terminal region

FAD - Flavin-Adenin-Dinukleotid

IRES - Internal ribosome entry site

Introduction

Ferroptosis

Ferroptosis has been designated as a regulated, iron-dependent form of cell death[1]. Execution of ferroptosis requires the presence of polyunsaturated fatty acid (PUFA)-containing lipids, oxygen, and free intracellular iron or iron-containing enzymes. These components can react, e.g. via Fenton reactions, to generate high levels of lipid peroxides, a hallmark of ferroptosis[2]. Unlike other programmed cell death modalities such as apoptosis, pyroptosis, or necroptosis[3], ferroptosis does not seem to converge through distinct signaling pathways into a terminal executioner, although recently NINJ1 was proposed to play a role in the final steps of ferroptosis execution [4]. Therefore, ferroptosis can at the moment only be vaguely defined as a unique cell death form associated with high levels of membrane lipid peroxidation that is blockable by membrane lipid peroxidation inhibitors such as Ferrostatin-1 (Fer-1) and Liproxstatin-1 (Lip-1) that function as lipophilic radical-trapping antioxidants[5–7]. To counteract lipid peroxidation accumulation, cells have evolved potent redox defense systems that often work orchestrated to neutralize excessive lipid peroxides [7–11]. In line with this, dysregulated ferroptosis has been associated with a variety of diseases, including neurodegeneration, renal failure, or stroke[12–16]. Additionally, ferroptosis has been identified as a promising anticancer treatment for refractory cancers[17]. Therefore, it is of great interest to understand the underlying mechanism.

Emergence of the ferroptosis field

Ferroptosis research goes back to the pioneering work of Harry Eagle in the 1950s where he discovered that cysteine deprivation causes cell death and that endogenous cysteine synthesis renders cells resistant to this type of cell death[18–20]. In 1958 Goldberg and Smith injected mice with iron dextran causing the formation of peroxides in the adipose tissues, which was rescued by vitamin E and worsened when mice were fed with unsaturated fat, establishing the first link between iron and lipid peroxidation[21]. Another important puzzle piece for defining the basic principles of ferroptosis was discovered in 1982 by characterizing the selenoenzyme and phospholipid hydroperoxidase glutathione peroxidase 4 (GPX4)[22]. The identification of the system x_c^- cystine/glutamate antiporter in 1999 elucidated the intimate role of cellular cystine uptake, glutamate secretion and Glutathione biosynthesis[23]. Later in

2001 oxytosis, which is an oxidative-stress-induced cell death in neurons, was described[24]. Using a synthetic high-throughput screening to identify compounds that kill cancer cells, Dolma and colleagues identified that Erastin, an inhibitor of the x_c^- antiporter, induces a non-apoptotic cell death process[25]. A similar screen was performed in 2008, identifying RSL3, a GPX4 inhibitor, as an iron-dependent, non-apoptotic cell death inducer in cancer cells[26]. In the same year, the lab of Marcus Conrad reported that conditional GPX4 knockout induces non-apoptotic cell death driven by lipid peroxidation that could be attenuated by alpha-tocopherol and that overexpression of xc- components rescued HH514 BL cells from lipid-peroxidation-induced non-apoptotic cell death[27,28].

In a follow-up study in 2012, the Stockwell group termed this iron-dependent form of non-apoptotic cell death for the first time ferroptosis. Within this work, they also identified the first potent inhibitor of ferroptosis, which they called Ferrostatin-1[1]. This groundbreaking work has opened the way for a new field of research that has seen exponential growth ever since **(Fig.1)**. Two years later the Conrad group characterized Lip-1 as another potent ferroptosis inhibitor[5]. Hence, the ferroptosis field ultimately emerged from a series of high-throughput screenings aiming either to kill cancer cells or to identify potent inhibitors of ferroptosis. These screenings significantly contributed to unravel the underlying mechanism of ferroptosis and opened a starting point for the development of new strategies to combat human diseases[7].

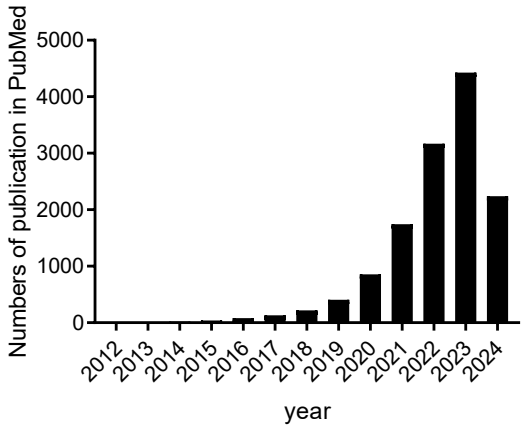

Fig. 1: The exponential growth of the ferroptosis research field since its founding in 2012 is illustrated by the cumulative number of ferroptosis related papers in the database PubMed.

Ferroptosis execution

Ferroptosis regulation and execution involve several lipid-centric mechanisms that govern cellular membrane integrity that are deeply interconnected with metabolic pathways[17]. Ferroptosis is driven by the accumulation of lipid peroxides and the formation of lipid hydroperoxides, either through imbalances in cellular metabolism or cellular redox defense systems that exceed their antioxidant buffering capacity and can be blocked by lipid peroxidation suppression or iron depletion in pharmacological and genetic means[17,29,30]. Lipid hydroperoxides can then react with iron to generate highly reactive lipid radicals that can be further modified and truncated contributing to ferroptosis execution[31]. Thereby, lipid hydroperoxides can either be formed in chemical reactions between PUFAs, reactive oxygen species (ROS) and iron or synthesized by lipoxygenase enzymes[32,33]. However, it is still unclear which of the two mechanisms is more important[7].

Until recently, downstream events of lipid peroxidation during ferroptosis execution have been elusive. A mechanism found by Hirata and colleagues and lately expanded by the Broz lab indicates that increased lipid peroxidation leads to an increased membrane tension, which activates Piezo1 and other transient receptor potential (TRP) mechanosensitive ion channels. This results in a net ion influx (Ca^{2+} and Na^{+}), that is further intensified by simultaneous inactivation of the plasma membrane Na^{+}/K^{+} ATPase, leading to the activation of NINJ1, by a yet unknown mechanism. NINJ1 activation causes NINJ1 to oligomerize, causing nanopores and over time membrane rupture **(Fig.2)** [4,34,35].

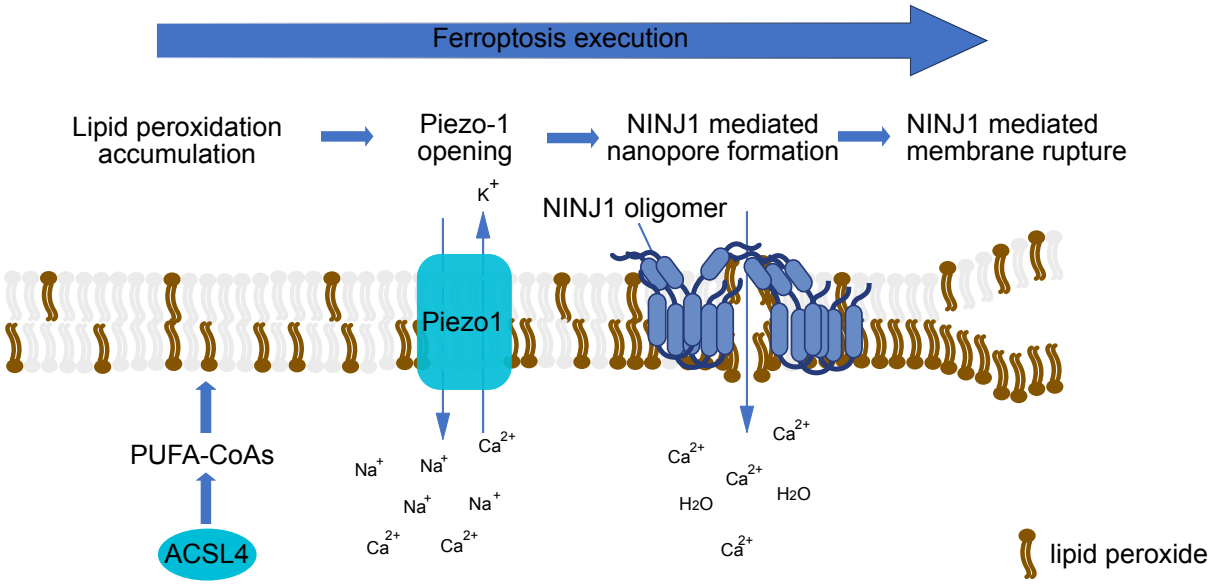

Fig. 2: Current model of ferroptosis execution. Accumulation of phospholipid peroxidation at the plasma membrane leads to increased membrane tension and in turn to the opening of mechanosensitive channels (Piezo-1 and TRP channels), resulting in a net ion influx of Ca^{2+} and Na^{+} and the release of K^{+}. Through an unknown mechanism, NINJ1 gets activated and oligomerizes, which causes nanopores and the additional instream of Ca^{2+} and H_2O. When the membrane damage is too severe, membrane rupture occurs in a probable NINJ1 dependent manner. Adapted from: [4,7]

However, these findings are in part contradictory with the model of ferroptosis execution that our lab proposed in 2021 **(Fig. 3)**[34]. In our model, cytosolic Ca^{2+} influx is the result of lipid peroxidation caused nanopores that is governed by osmotic pressure. Accordingly, we could not delay lipid peroxidation, but ferroptosis execution by utilizing osmoprotectants. However, it can be speculated that Piezo1 might contribute downstream of membrane pores to further facilitate Ca^{2+} influx. Cytosolic Ca^{2+} activates ESCRT-III components that counteract ferroptotic execution by actively contributing to the membrane repair. If the damage is too severe for reparation, plasma membrane disruption is caused by an imbalance in osmotic forces due to the opening of small nanopores.

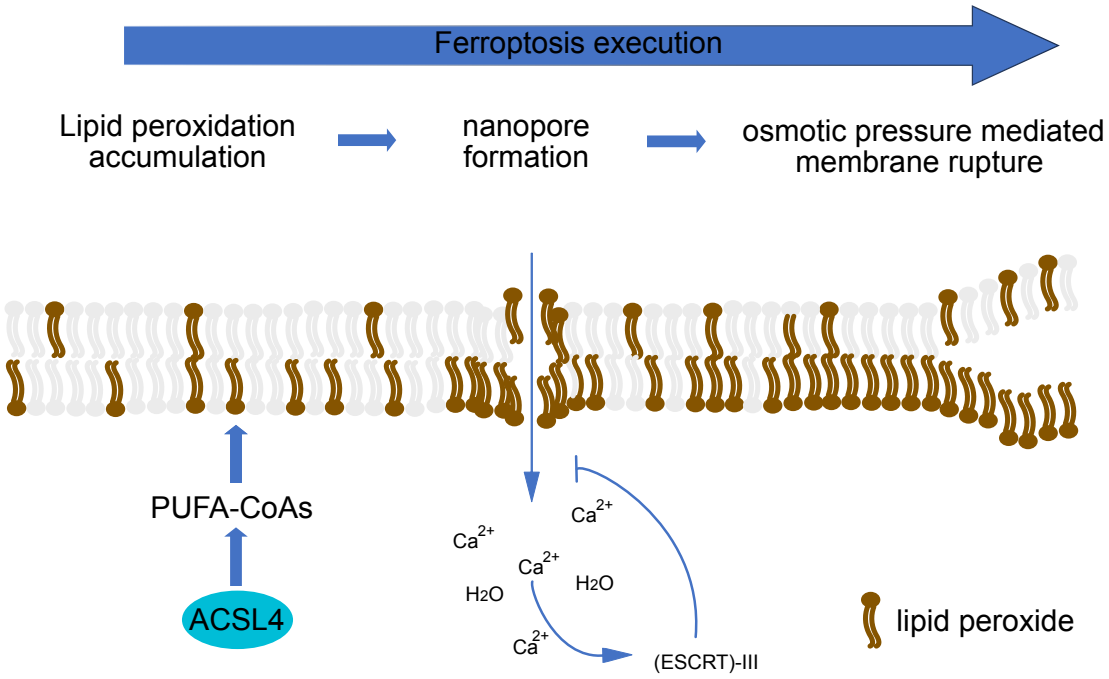

Fig. 3: Our model of ferroptosis execution[34]: Accumulation of phospholipid peroxidation at the plasma membrane leads to the formation of nanopores resulting in an influx of Ca^{2+} and H_2O. Ca^{2+} activates ESCRT-III components that participate in plasma membrane repair. Ion fluxes generate osmotic pressures that mediate plasma membrane rupture if the ESCRT-III system exceeds its repair capabilities.

Future studies are required to resolve the role of Piezo1 in Ca^{2+} fluxes and to clarify how NINJ1 gets activated, whether NINJ1 is required or facilitates nanopore formation and membrane rupture during ferroptosis execution.

Biochemistry of lipid peroxidation

Lipid peroxidation is a hallmark of ferroptosis that differentiates ferroptosis from other forms of regulated cell death[36]. Since cellular membranes consist of large amounts of polyunsaturated fatty acids, they are the primary target for free radical lipid peroxidation, because of their free cholesterol and esterification of phospholipids[37].

Therefore, the term lipid peroxidation implies oxygenation of lipids such as the formation of lipid hydroperoxides. However, the term does not differentiate whether products are formed spontaneously or through an enzyme catalyzed process[2]. However, independent of how lipid hydroperoxides are formed, they can serve in specific conditions as initiators to generate peroxide products under oxygen consumption. In these settings, lipid peroxidation can be understood as a chain reaction, consisting of initiation, propagation and termination phases **(Fig. 4A)** [2,37].

In the initiation step, a labile hydrogen atom gets subtracted from the substrate by an initiating radical. Thereby, initiator radicals stem from one-electron reduction of the hydroperoxide in a Fenton-like reaction forming either lipid alkoxyl or hydroxyl radicals. In a broader sense, a Fenton reaction is defined as a chemical reaction between iron and hydrogen peroxide (H2O2) yielding highly toxic free radicals, which in turn can spark lipid peroxidation. Reducing agents in these reactions can either be low-valent iron, copper or good one-electron donors such as ascorbate or hydroperoxyl radicals **(Fig. 4A)**.

This yields a carbon-centered radical that can react with O_2, giving a peroxyl radical capable of propagating a chain reaction by reacting with another substrate molecule[2]. Hereby, the propagation reactions are competing with termination. If two peroxyl radicals react with each other, the reaction stops by yielding an alcohol, a carbonyl compound and O_2. Polyunsaturated fatty acids (PUFA) are prone for undergoing autooxidation, because their bis-allylic hydrogen have in comparison to other lipid species low bond dissociation energies. This results in a relatively higher lipid peroxidation formation rate that was shown to drive ferroptosis **(Fig. 4B)**[2,29].

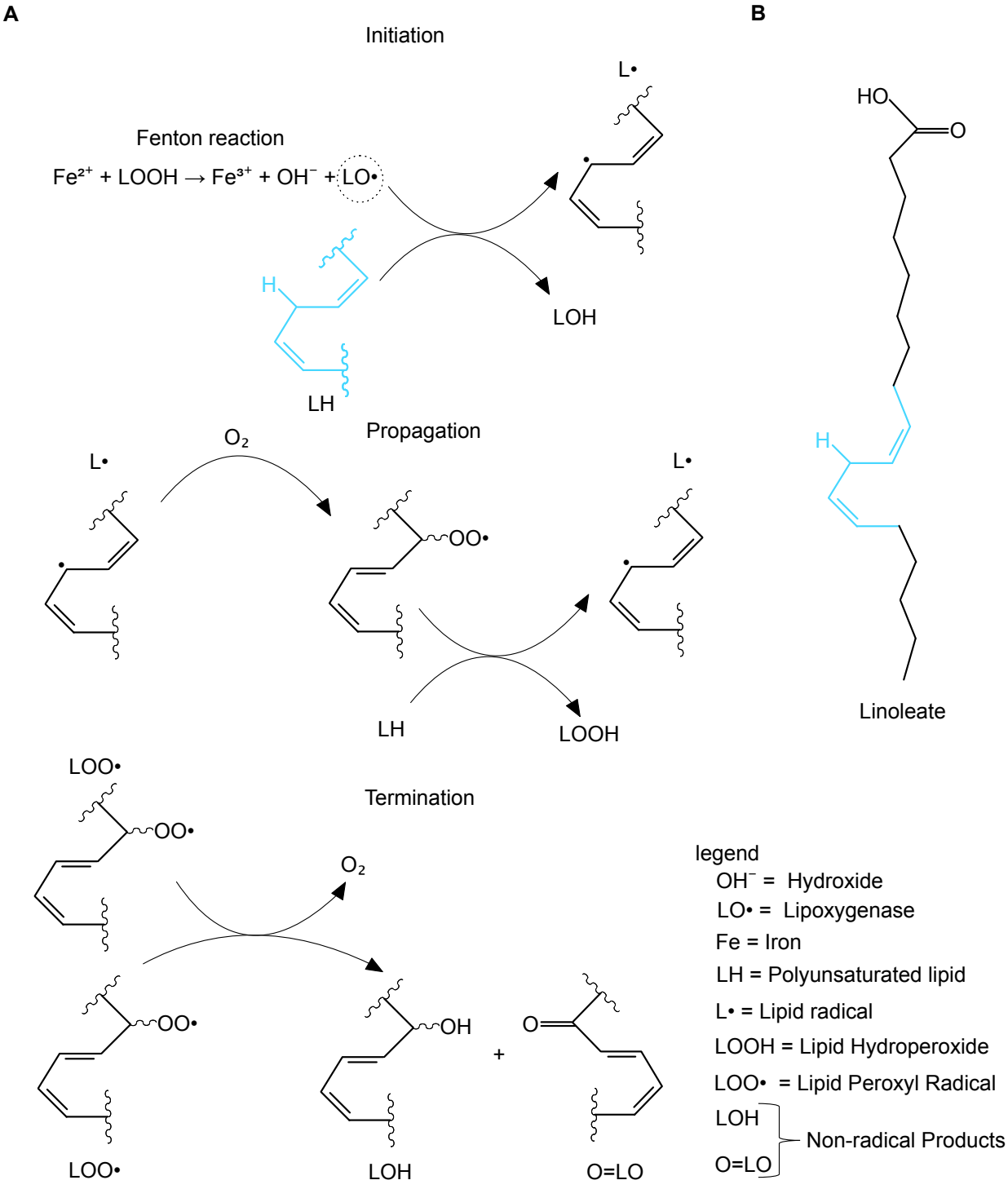

Fig. 4: Key steps in lipid peroxidation formation. A) Scheme showing how a bis-allylic moiety of a polyunsaturated lipid (blue) can be oxidized by a radical generated e.g. via a Fenton reaction, how this reaction can be propagated in a chain reaction to other bis-allylic moieties and how this chain reaction is terminated. **B)** Linoleate as an example of a polyunsaturated lipid. Bis-allylic moiety is illustrated in blue. Adapted from: [2,37]

Lipid peroxidation can also be enzymatically catalyzed by lipoxygenases (LOXs), non-heme iron dioxygenases or cyclooxygenases (COXs)[38]. LOXs catalyze the stereospecific insertion of molecular oxygen into arachidonic acid, resulting in hydroxy derivatives as end products, whereas COXs reside upstream a complex metabolic cascade that ultimately converts PUFAs into more bioactive lipids[39,40]. However, their role in initiating ferroptosis is controversial[29].

Starting point of ferroptosis

The specific cellular membranes that are crucial for the initial spark of lipid peroxidation required for ferroptosis execution are currently unknown. Also unknown is whether and how lipid peroxidation reaction spreads from this starting point within cells. Most cellular membranes/organelles have been linked to ferroptosis sensitivity regulation including the plasma membrane, mitochondria, ER, Golgi, nucleus, peroxisomes, lysosomes, lipid droplets etc. However, it is largely unknown how these different, often opposing functions, are harmonized into distinct decisions about whether ferroptosis is executed or not [7]. A model proposed by Dixon in 2023 suggests that every protein, metabolite or biomolecule that can alter iron, lipid or redox metabolism could have a quantitative effect on lipid peroxidation and thus ferroptosis sensitivity[33].

Ferroptosis execution vs. sensitivity

For the investigation of neighboring cell responses in the context of ferroptosis, it is crucial to differentiate mechanisms of ferroptosis execution from mechanisms that alter ferroptosis sensitivity. In short, ferroptosis execution includes all processes that lead to membrane lipid peroxidation, net ion influx through the plasma membrane, cell swelling and plasma membrane rupture[35]. Ferroptosis sensitivity on the other hand, describes the probability that a certain trigger causes ferroptosis execution. Therefore, ferroptosis sensitivity is tightly regulated by pathways controlling lipid metabolism, iron homeostasis and redox governance, etc. Hence, ferroptosis sensitivity is controlled by hundreds of enzymes and molecules in cells, that all influence in a complex interplay whether ferroptosis execution can occur[33].

Mechanisms controlling ferroptosis execution

The endosomal sorting complexes required for transport (ESCRT-III) system has been identified as an antagonist mechanism to limit membrane damage during regulated cell death programs including necroptosis, pyroptosis and ferroptosis[41–44]. In the ferroptotic context, lipid peroxidation can cause increased intracellular Ca^{2+} levels, which act as a recruiting signal for ESCRT-III components, to transport charged multivesicular body protein 5 (CHMP5) and CHMP6 to the plasma membrane where they participate in membrane repair **(Fig. 3)**. Accordingly, CHMP5, CHMP6 or CHMP4B knockdown was shown to increase ferroptosis vulnerability. However, this repair mechanism is ineffective when excessive lipid peroxidation occurs and cannot inhibit ferroptosis execution[34,42].

Mechanisms controlling ferroptosis sensitivity

Driven by high-throughput screenings for novel small-molecule anticancer therapies and subsequent counter-screenings, inducers and inhibitors of a new form of non-apoptotic, lytic cell death were identified. Investigation of the underlying mechanism identified that either the inhibition of the system xc- through Erastin or GPX4 by RSL3 induces ferroptosis **(Fig.5)**. Additionally, it was demonstrated that iron chelators and lipophilic radical-trapping antioxidants inhibited this cell death modality, showing the dependency on iron for this process[1,5,25].

GPX4-GSH system

The selenoprotein GPX4 is a member of the glutathione peroxidase (GPX) protein family that converts phospholipid hydroperoxides to phospholipid alcohols[27,45] and was therefore found to be the most important enzyme to hold lipid hydroperoxide levels in check in most cells[5,27]. GPX4 requires the catalytic selenocysteine residue of GPX4 and two electrons, which is provided by Glutathione (GSH), for its function to reduce phospholipid and hydroperoxides to their respective alcohols[18]. This crucial role is emphasized by the fact that GPX4 depletion or inhibition triggers ferroptosis[46]. GSH is a tripeptide consisting of glycine, glutamate and cysteine. Cysteine is the bottleneck in GSH synthesis and is mainly imported through the xc^- system as cystine, the oxidized form of cysteine[47,48]. Disruption of the cystine import through pharmacological inhibition of the xc^- system, e.g. with Erastin, or depletion of cystine from the cell culture media induced ferroptosis in various cancer cell lines[1,49]. Hence, the GPX4-GSH system is the most powerful anti-ferroptosis defense system and either direct GPX4 inhibition through RSL3 or indirect inhibition through cysteine deprivation by Erastin leads to excessive phospholipid hydroperoxides accumulation and subsequent ferroptotic cell death **(Fig. 4)**[17, 50].

As mentioned above, GPX4 has a selenocysteine within its active site. Although selenocysteine is not required for cell survival and proliferation of mammalian cells, selenolate- vs. thiolate-based catalysis has a clear advantage in its resistance to overoxidation. WT GPX4, in contrast to GPX4-Cys, was found to form a selenylamide intermediate in the absence or low levels of reducing equivalents (GSH), preventing its irreversible oxidation that is crucial for controlling lipid peroxidation and ferroptosis[51]. In settings with low selenium, GPX4 translation is distorted leading to early GPX4 translation termination by ribosome stalling and collisions, which causes increased vulnerability to ferroptosis[52]. Selenium can either enter the cell by selenium-containing carrier protein selenoprotein P, which is bound and subsequently endocytosed by receptors like the LDL receptor-related protein 8 (LRP8), or via conversion of inorganic selenium through a system xc- dependent process **(Fig. 6)**. Accordingly, LRP8 knockout was shown to sensitize cells to ferroptosis inducers in triple-negative breast cancer cells[52–55].

GPX4 exists in several isoforms localized in the cytosol, mitochondria or nucleus, whereby the cytosolic isoform is considered the most important for inhibiting ferroptosis[7].

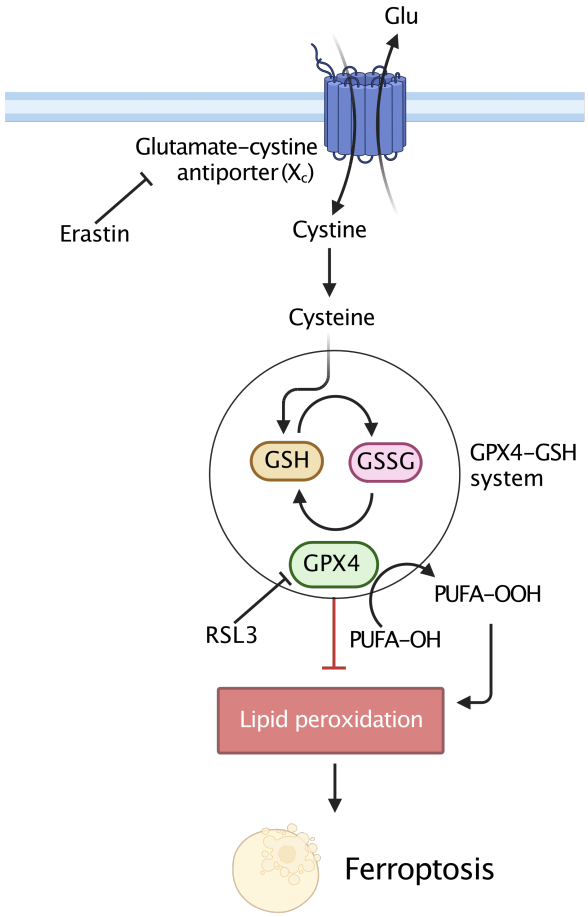

Fig. 5: x_C^--GSH-GPX4 pathway protects cells from phospholipid peroxidation by direct reduction of phospholipid hydroperoxides to their corresponding alcohols through GPX4. Chemical inhibition of GPX4 by RSL3 or x_C^- by Erastin results in excessive phospholipid hydroperoxides accumulation and subsequent ferroptotic cell death. Adapted from:[17] and created with BioRender.

ACSL4

Other players regulating ferroptosis have been identified via genome-wide haploid and CRISPR-Cas9-based screens. Acyl-CoA synthetase long-chain family member 4 (ACSL4) involvement in the ferroptosis process stems from its ability to ligate preferably long-chain PUFAs, including arachidonic acid (20:4) and adrenic acid (22:4) with coenzyme A. Subsequently several LPCATs can re-esterify those products into phospholipids. This increases the incorporation of long-chain PUFAs into cellular membranes[56–58]. Accordingly, depletion of ACSL4 leads to a substantial shift from long-chain PUFA to short-chain and monounsaturated fatty acid (MUFA) in cellular membranes, allowing the survival of ACSL4-deficient cells in a GPX4 deficient background[56,58,59]. Increased ACSL4 activity on the other hand showed indications of promoting ferroptosis in the context of ischemia-reperfusion injury and radiation responses **(Fig. 2)**[60].

FSP1-CoQH redox system

The FSP1-CoQH redox system was shown to inhibit plasma membrane peroxidation independent of GPX4. It consists of the NAD(P)H- and FAD-dependent oxidoreductase FSP1 and the coenzyme Q10 (CoQ). FSP1 reduces Q10 (CoQ) and vitamin K, whose reduced forms act as lipophilic radical-trapping antioxidants, capable of terminating lipid peroxidation chain reactions. FSP1 specifically localizes to the plasma membrane and lipid droplets, which was shown to be crucial for its anti-ferroptotic activity **(Fig. 6)**[61–63].

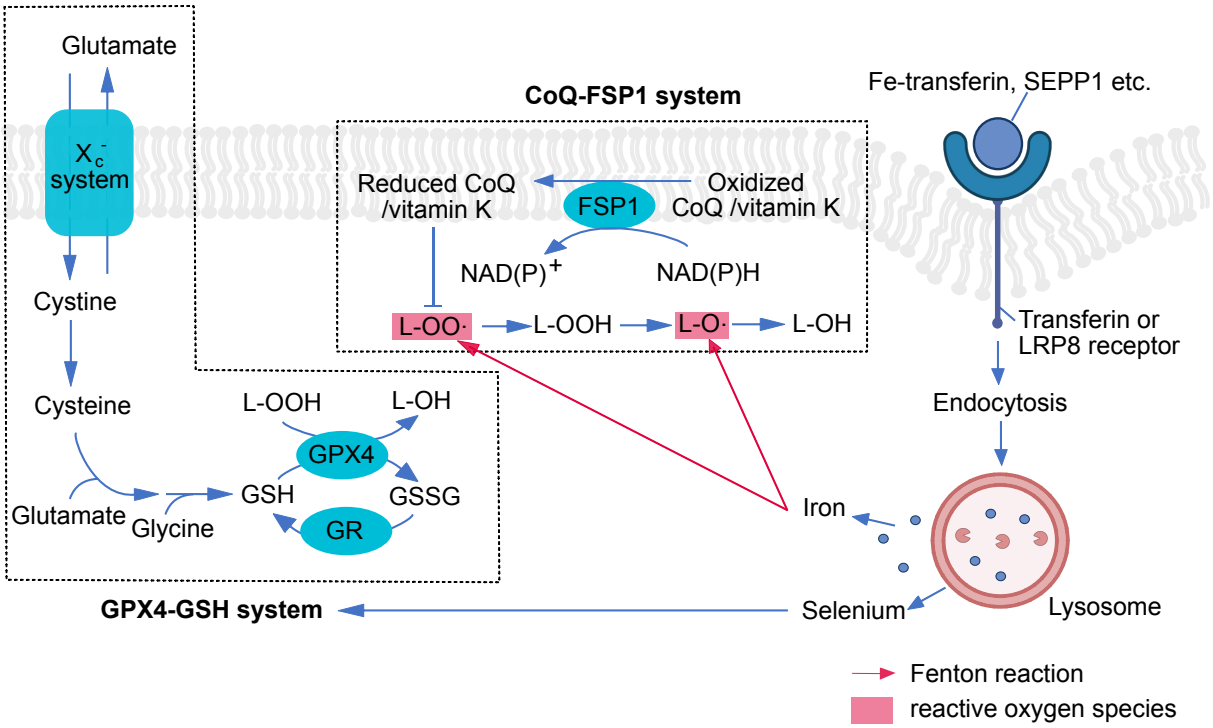

Fig. 6: Important ferroptosis defense systems. In the GPX4-GPX4 pathway, the xc- system imports cystine in exchange for glutamate. Cystine is then reduced to cysteine in the cytosol, where it is required for the synthesis of GSH. GSH acts as a cofactor for GPX4 to reduce toxic phospholipids (L-OOH) into their corresponding alcohols (L-OH). In the CoQ-FSP1 system, FSP1 regenerates under NAD(P)H consumption radical-trapping antioxidants such as coenzyme Q10 (CoQ) or vitamin K. Reduced CoQ/ vitamin K stops lipid peroxidation reactions by donating electrons to phospholipid peroxyl radicals (LOO•). Ferroptosis sensitivity is regulated by receptor-mediated endocytosis. Uptake of iron complexes via the transferrin receptor enhances ferroptosis sensitivity, whereas the uptake of selenium-rich protein SEPP1 by the LRP8 receptor suppresses ferroptosis sensitivity. Upon endocytosis iron and selenium are released from lysosomes. Released iron can interact with lipid peroxides to generate hydroxyl and alkoxyl radicals that promote lipid peroxidation. Released selenium can be used to synthesize GPX4. Adapted from: [7]

Other defense systems

Apart from Coenzyme Q (CoQ) and vitamin K, various other endogenous metabolites can act as ferroptosis suppressors by serving as lipophilic radical-trapping antioxidants, including tetrahydrobiopterin, vitamin E, vitamin A, and 7-dehydrocholesterol. The extent to which these metabolic ferroptosis inhibitors contribute seems to differ among different cell types[64–67].

Lipids metabolism and Ferroptosis

There is increasing evidence that the lipid composition of cells and the mechanism by which cells store, catabolize and synthesize different lipids have a great impact on defining their ferroptosis sensitivity[29,68,69]. Accordingly, cells can modulate their ferroptosis sensitivity through the control of abundance and localization of fatty acids with differing oxidation potential, by controlling their synthesis, trafficking and flux. However, it is not well understood how fatty acid trafficking to other compartments contributes to ferroptosis and how decisions for fatty acid conversions into other species are made[7]. One important nexus was identified with cytosolic acetyl-CoA carboxylase 1 (ACC1) synthesizing malonyl-CoA, because malonyl-CoA can either be used for the synthesis of long-chain saturated fatty acids through the fatty acid synthase (FASN) of for the elongation of imported PUFASs into different longer chain length products[70]. Another checkpoint in lipid metabolism lies in the ER, where fatty acids are activated by ACSL enzymes and build into phospholipids or TAGs by acyltransferases. Also, in the ER the desaturation of long-chain saturated fatty acids via FADS1, FADS2 and SCD1[7]. On top of that, signaling pathways were shown to render enzyme activity in different cancer-related settings[71–73].

Iron in Ferroptosis

As described above, iron is required for ferroptosis execution and is therefore a major ferroptosis regulator. Accordingly, cellular iron homeostasis is tightly regulated by post-transcriptional regulation of genes involved in iron storage/release and import/export through the iron-regulatory proteins IRP1 and IRP2[74,75]. Hence, all cellular processes that alter the accessibility of cellular labile iron content modulate ferroptosis vulnerability. On that account, the increase of cellular iron availability through autophagic ferritin degradation, which is an iron-storage protein, was shown to promote ferroptosis[76,77]. In line with this, ferroptosis can also be promoted by enhanced cellular iron import through transferrin and its receptor (TFRC)[78]. In this process, Fe^{3+}-transferrin complexes are imported through receptor-mediated endocytosis, whereafter these complexes are trafficked and liberated inside lysosomes **(Fig.6)**[7]. Accordingly, TFRC knockdown was shown to inhibit ferroptosis, by limiting cellular iron uptake[26,78,79]. Mitochondria, central hubs for iron use and metabolism, are also implicated in ferroptosis regulation. Increased mitochondrial iron uptake by mitoferrin1

(MFRN1) or disruption of mitochondrial Fe–S cluster biosynthesis was shown to enhance ferroptosis sensitivity[80,81].

Role of cell density in Ferroptosis

Another layer of ferroptosis regulation was discovered when studying ferroptosis in the context of high cell density. Wu et al. found that high cell density upregulates E-cadherin expression in certain cell types, making them more resistant to ferroptosis induction through cysteine deprivation and GPX4 inhibition[82]. In line with this, other reports found that extremely high cell densities allow the survival of GPX4 knock-out cells *in vitro*[27,83]. The found mechanism has been proposed to depend on the Hippo pathway and YAP signaling[82,84,85]. The Hippo-Yap pathway is an important nexus in various biological functions such as cell proliferation and organ size[86,87].

Ferroptosis propagation

Adding another layer of complexity, ferroptosis has been suggested to spread through cell populations *in vitro*, associated with the spread of necrosis in diseased tissues. Recently ferroptosis propagation was also linked to cell death events in physiological conditions during development[88]. In line with this, Erastin administration caused synchronous necrosis of renal tubules *ex vivo*, which could be rescued by ferroptosis inhibitors[89]. Moreover, *in vitro* ferroptosis induction has been observed in wave-like patterns, exhibiting distinct spatiotemporal characteristics compared to other forms of cell death[90–93]. A recent study found that Platelet activation factor (PAF) and its derivatives play a role in this process[94]. Another paper identified ROS trigger waves allowing ferroptosis propagation, which speed and progression can be modulated by ROS feedback loops through genetic and chemical means. However, the utilization of drugs to induce or hinder ferroptosis, potentially impacting all cells within the population in their ferroptosis sensitivity, has limited the investigation of ferroptosis spread between cells. Consequently, the concept of ferroptosis propagation remains contentious, with key open questions regarding its molecular mechanisms and its role in contributing ferroptosis sensitivity to tissues.

Ferroptosis in Disease

Ferroptosis has been associated as an important player in numerous pathogeneses and their progression. Pathologies implicated with ferroptosis are cancers, neurological disorders, cardiovascular disease, pulmonary conditions, gastrointestinal disorders, urogenital issues, endocrine dysfunctions, iron overload syndromes, musculoskeletal disorders, and autoimmune diseases[95]. While this long list of pathologies implicated with ferroptosis underpins the clinical significance and potential for therapeutic interventions, further research is needed to determine whether ferroptosis is causing the disease or ferroptosis occurs as a secondary effect. Hence, most observations so far reveal cell death in diseased tissues, which can be rescued using lipophilic radical-trapping antioxidants, limiting symptom severity. However, it will be necessary in the future to disentangle this chicken or the egg causality dilemma to elucidate ferroptosis's contribution to these pathologies. Therefore, the development of improved tools for studying ferroptosis is necessary including the identification of *in vivo* ferroptosis biomarkers[17].

Optogenetics

Optogenetics is a modern technique that combines genetic engineering with optics to control diverse cellular functions with light by utilizing genetically encoded protein switches with outstanding spatial and temporal resolution. This technology opens numerous areas of research, by enabling the investigation of biological questions that previously could not be addressed. On top of that, optogenetics holds the potential to be translated into powerful biomedical and therapeutical applications[96].

Emergence of the optogenetics field

Although light-sensitive photoreceptors have been studied for decades in the context of energy capture, storage and regulation of developmental processes in diverse organisms, they have only been recently systematically utilized to control cellular processes with light[97]. Hence, although Richard Fork already postulated in the year 1971 in a Science paper the significant impact of being able to specifically and reversibly activate individual neurons for studying cellular interconnections, it took until 2002 to use photoreceptors as actuators by expressing Drosophila rhodopsin and respective signaling proteins in neurons[98,99]. The technology was further boosted by the discovery of channelrhodopsin (ChR) in the green Algae *Chlamydomonas* since its light-absorbing chromophore (all-trans-retinal, a vitamin A derivate) is ubiquitously expressed in most organisms and hence can be exploited as a useful tool[97,100]. Further adaption of ChRs led to neuronal *in vivo* applications in chicken embryos, C. elegans, Drosophila, mice, zebrafish and non-human primates in the following years[101–106].

Optogenetics toolbox

Over the last 20 years, the optogenetics toolbox has constantly been expanded, which has had a tremendous impact not only on neuroscience but also recently a growing impact on other disciplines such as cardiology and cell biology in general. The toolbox includes actuators that can be activated by several specific wavelengths that enable the control of a wide array of cellular functions by light through their different modes of action[96]. Thereby, optogenetic actuators enable light control in specific

processes such as neuronal firing, but also manipulate other cellular processes such as protein-protein interactions, protein transcription, protein localization, protein degradation, etc. In the following, optogenetic systems are discussed that act as molecular switches and are of relevance in this thesis[107,108].

Molecular switches

Optogenetic switches are comprised of photoreceptors that undergo conformational changes upon illumination with a distinct wavelength. Depending on the activation mechanism of a protein of interest, different photoreceptors can be utilized to regulate its activity. For instance, if a protein of interest gets activated upon oligomerization, like most Caspases, molecular switches can be employed to facilitate homo- or heterodimerization of fusion partners. Another activation mode that can be exploited is the uncaging of a motif of interest like a nuclear import/export, or degron sequences, that make the motifs accessible through light induced intramolecular conformational changes[108].

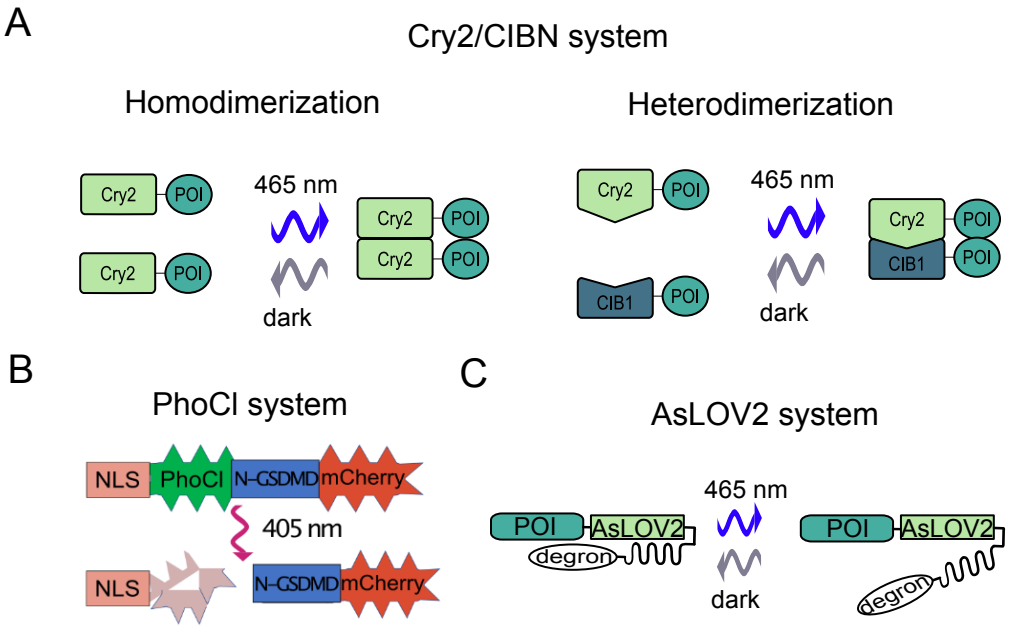

Fig. 7: Overview of selected optogenetic molecular switches. A) Cry2 forms homo-oligomers or interacts with CIBN to form heterodimers upon blue light illumination. **B)** UV illumination induced PhoCl cleavage leads to the release of N-GSDMD-mCherry[109]. **C)** Blue light illumination leads to the unwinding of the Jα-helix of AsLOV2, which thereby uncages in this case a degron sequence. Adapted from: [109,110]

The Cryptochrome 2 (Cry2) protein stems from *Arabidopsis thaliana,* which was shown to enable control by light of a protein of interest by tuning its protein-protein interactions, activity or intracellular localization. Cry2 is a flavoprotein receptor that binds to flavin adenine dinucleotide (FAD) non-covalently, mediating light-responsiveness with an absorption maximum of around 450 nm and, hence requiring no exogenous chromophore. Upon blue light exposure Cry2 changes its conformation, which enables it to either bind to its interaction partner cryptochrome-interacting basic helix-loop-helix 1 (CIB1), forming heterodimers, or to cluster with other Cry2 molecules to form homo-oligomers **(Fig. 7A)**[110–113].

The photocleavable protein (PhoCl), which is based on a green-to-red photoconvertible version of mMaple, undergoes an irreversible cleavage upon illumination with 400 nm, resulting in a bigger N-terminal and in a small C-terminal fragment[114]. This characteristic can be exploited to design optogenetic tools by cloning a fusion protein of a nuclear localization sequence (NLS) with PhoCl and a protein of interest. For instance, we recently designed a tool where, in the dark, the N-terminal GasderminD is trapped in the nucleus, but upon activation, N-GasderminD gets released out of the nucleus and induces pyroptotic cell death **(Fig. 7B)**[109].

Another widely used optogenetic system for various applications is based on the LOV2 domain of phototropin 1 derived from *Avena sativa* (AsLOV2). Intramolecular conformational changes upon blue light illumination lead to the unwinding of the Jα-helix into an open structure, making, for instance, nuclear import/export or degron sequences accessible for interactions with cellular partners **(Fig. 7C)**[115–117].

Advantages and limitations of optogenetic tools

Optogenetics has a distinct advantage over other methodologies in its ability to achieve high spatial resolution, allowing a fine-tuned control from the cell population scale to the single cell level and even specific subcellular cell areas such as individual mitochondria or plasma membrane sections, etc **(Fig. 8)**[110]. An example of this versatility was demonstrated in a study using a LOV2-domain based optogenetic tool for controlling local activation and recruitment of RhoA GTPase to the plasma membrane of epithelial cells, showing that it is possible to control protein activity in a

spatially controlled manner[118]. On the other hand, it is also possible to tune, for example, optogenetic-induced Caspase activation to either trigger dependent on the magnitude of the activation illumination (area, duration and intensity), sublethal Caspase activation or cell death **(Fig. 9)**[115,116].

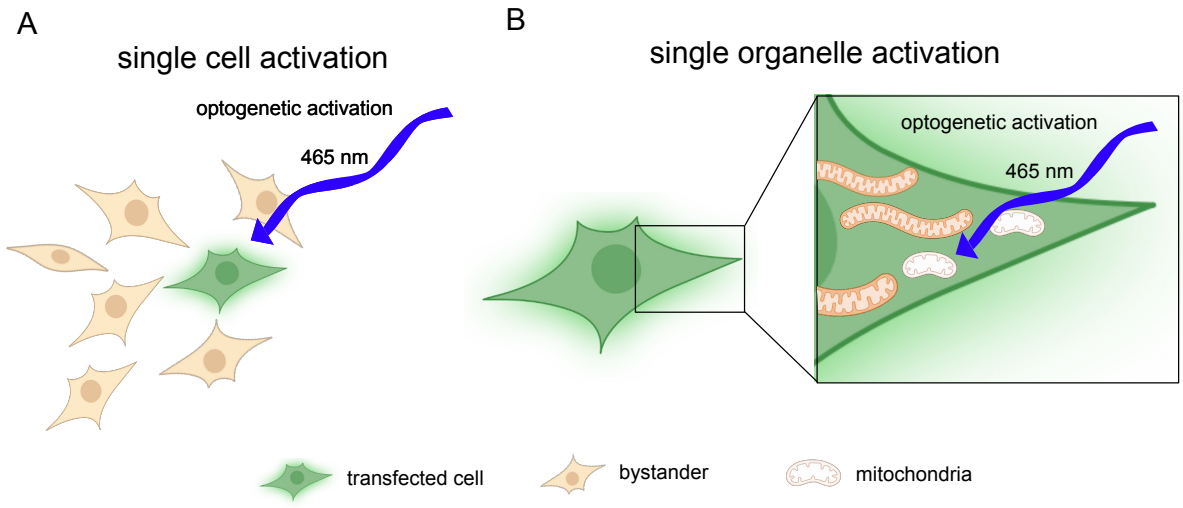

Fig. 8: Optogenetics allows regulation of protein activity on single cell- or subcellular level. Adapted from: [112]

The second distinct advantage of optogenetics over conventional chemical inducers is its unprecedented temporal resolution, enabling mimicking signaling events at every level of a given pathway, since light allows flexible ON-OFF switching of protein activity in a second-to-minutes time range. This allows the dissection of biological processes that lead to particular signaling events within the same signaling pathway[110]. For instance, Repina and colleagues showed in a study that it is possible to simulate Wnt signaling gradients that usually occur during development by applying different light intensities to activate a Cry2 based optogenetic tool to control the clustering of the low-density lipoprotein receptor-related protein 6 (LRP6). Further, they demonstrated that the longest illumination duration, led to the highest Wnt signaling[121]. In line with this, another Cry2/CIBN based tool to control TGF-β signaling showed a similar fine-tuning capability using different light intensities. By applying different illumination patterns with either single light pulses, several light pulses over time or continuous illumination, they achieved oscillating or sustained TGF-β signaling in single cells[110,122].

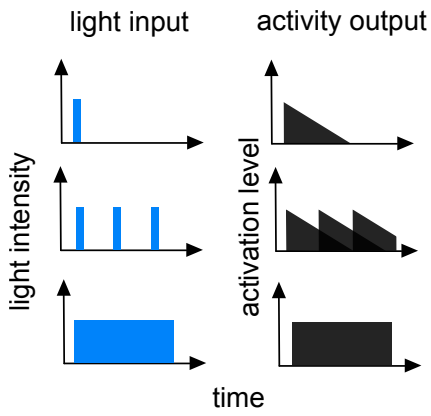

Fig. 9: Temporal resolution of optogenetics. Light input patterns correlate with protein activity output. Adapted from: [110]

Although optogenetic tools have, as described above, many advantages in comparison to conventional drug treatments, they also come with some challenges or limitations. One challenge is the complexity of the experiments, since additional controls for all experiments are required to rule out illumination caused phototoxicity. Another limitation is the low activation threshold of currently available optogenetic tools, which require cultivating cells in dark conditions. In order to avoid unwanted autoactivation, optogenetic tools have been expressed under inducible promoters, with the disadvantage of treating cells with chemicals, which could potentially cause off-target effects and hence also require additional controls[108].

Current optogenetic tool design often involves the generation of fusion proteins encoding for a protein of interest, a photo-activator and a fluorescence tag for the identification of optogenetic tool expressing cells. Accordingly, gene delivery can be challenging due to the size of the fusion protein, which often range from 5-10k base pairs. Depending on how easy cells acquire foreign DNA, optimizing transfection conditions might be required. Gene delivery to primary cellular systems requires the utilization of more sophisticated methods such as lenti- or retroviral transductions. Since most photoactivatable proteins stem from different species then the recipient cellular system or organism, complications regarding immunogenicity might arise.

In essence optogenetic tools are artificial overexpression systems that can face limitations regarding the localization, function and structure of the respective protein of interest[123]. Hence, all derived results should be complemented with alternative methodologies to rule out overexpression artefacts. This effect could potentially be

worsened due to the fluorescent tag of the fusion protein. To overcome these limitations, IRES element containing constructs could be designed that allow transfection tracking via a fluorescence signal without the need of tagging the protein of interest[124,125]. Additionally, when using a nanobody against a protein of interest instead the respective cDNA, this strategy could be used to control endogenous proteins. The downturn of this approach is the restricted availability of nanobodies, which would significantly limit the use cases.

Manuscript:

Ferroptosis spreads to neighboring cells via plasma membrane contacts

(currently under review)

Authors
Bernhard F. Roeck [1,2], Sara Lotfipour Nasudivar[1,2], Michael R. H. Vorndran [1,2], Lena Schueller[1,2], F. Isil Yapici[2,3,4], Matthias Rübsam[2,4,5], Silvia von Karstedt[2,3,4], Carien M. Niessen[2,4,5], Ana J. Garcia-Saez[1,2,6 *]

*Corresponding author

Affiliations

1. Institute for Genetics, University of Cologne, Joseph-Stelzmann- Straße 26, 50931 Cologne, Germany
2. CECAD Cluster of Excellence, University of Cologne, Joseph- Stelzmann- Straße 26, 50931 Cologne, Germany
3. Department of Translational Genomics, Center of Integrated Oncology Cologne-Bonn, Medical Faculty, University of Cologne, Joseph-Stelzmann-Straße 26, 50931 Cologne, Germany
4. Center for Molecular Medicine Cologne, Medical Faculty, University Hospital of Cologne, Robert-Koch-Straße 21, 50931 Cologne, Germany
5. Department Cell Biology of the Skin, Center for Molecular Medicine Cologne,University of Cologne, Cologne, Germany.
6. Max-Planck-Institute of Biophysics, Frankfurt, Germany.

Authors contribution

BFR performed experiments and analyzed data. MRHV built custom software and analyzed experiments. SLN and BFR designed and performed lipid bilayer experiments. SLN performed the experiments with GUVs. LS generated the HeLa α-catenin KO cells. FIY and SvK designed and conducted the supernatant experiment. All authors contributed to experimental design and manuscript writing. AJG-S conceived the project, supervised research and wrote the manuscript together with BFR. The derived thesis was entirely written by BFR.

I estimate my contribution to this manuscript to be 85%.

Objectives

Ferroptosis has been observed to spread through cell populations *in vitro* and is linked to the propagation of necrosis in diseased tissues and to cell death events during development[88]. For instance, Erastin administration caused synchronous necrosis of renal tubules *ex vivo*, which could be rescued by ferroptosis inhibitors[89]. Ferroptosis propagation was described to occur in a wave-like pattern that exhibits distinct spatiotemporal characteristics compared to other forms of cell death[90–93]. A recent study found that Platelet activation factor (PAF) and its derivatives contribute to this process[94], whereas another study proposed that trigger waves of reactive oxygen species enable ferroptosis propagation[88]. However, this process has only been studied using conventional drug interventions to induce or hinder ferroptosis, which potentially impacts all cells within the population in their ferroptosis sensitivity and hence has limited the investigation of ferroptosis spread between cells. Accordingly, in this thesis, we want to investigate the underlying mechanism of ferroptosis propagation without changing the ferroptosis sensitivity of the cell population with the following objectives:

- Development of an optogenetic tool that specifically induces ferroptosis.
- Characterization of key parameters of ferroptosis propagation.
- Uncover the underlying mechanism of ferroptosis propagation.

Results

Opto-GPX4Deg induces cell death via ubiquitin mediated proteasomal degradation of GPX4.

To study neighboring cell responses unbiasedly, we developed an optogenetic tool that enables us to trigger ferroptosis by light through the depletion of GPX4, which is currently known as the most potent strategy for inducing ferroptosis. Therefore, we designed a LOV2-based optogenetic tool as a fusion protein encoding for GFP, GPX4 and the photoactivatable LOVpepdegron. This LOV2 based fusion protein, which we named Opto-GPX4Deg, changes its conformation upon blue light illumination, by exposing an RRRG degron sequence for ubiquitin-mediated proteasomal degradation **(Fig. 1A)**[126,127]. A version of Opto-GPX4Deg without RRRG degron sequence that we called Opto-Ctrl was used throughout the study as a control for checking for illumination-mediated cytotoxicity. As a next step, we tested whether HeLa and HEK293 were suitable cellular systems to validate Opto-GPX4Deg by checking their ferroptosis sensitivity. Therefore, we treated HEK and HeLa cells with three structurally different ferroptosis compounds (RSL3, Erastin and FINO2) and acquired cell death kinetics by high-throughput live cell imaging. As expected, treatment with all compounds led to around 80 % cell death over the time course of 24h, with slightly slower kinetics for HeLa cells, which could be entirely inhibited when cotreating the cells with the antioxidant Fer-1, indicating that these cells are ferroptosis sensitive. Of note, RSL3 treatment of HeLa cells resulted in lower cell death induction compared to the other ferroptosis inducing compounds. Together this data shows that HeLa and HEK cells are ferroptosis sensitive and hence are suitable cellular systems to validate Opto-GPX4Deg **(Fig. S1A-F)**.

For testing Opto-GPX4Deg in a high-throughput optogenetics pipeline in a 96-well-plate format, we seeded HEK293 or HeLa cells the day prior to transfection with Opto-GPX4Deg or Opto-Ctrl and incubated them for 16h before treated or not with different Fer-1 concentrations. Then, we acquired pre-activation images to determine the potential autoactivation of Opto-GPX4Deg. Afterwards, we activated the optogenetic tools using the 465 nm LEDs of an optoPlate-96 [128,129] at 100 % for 30 min and assessed the cell death kinetics via life cell imaging **(Fig. 2B)**. As expected, upon optogenetic activation cell death induction of Opto-GPX4Deg expressing HEK293 and HeLa cells was significantly higher compared to Opto-Ctrl expressing cells. Optogenetically triggered cell death could be delayed with the administration of Fer-1

in a concentration-dependent manner and cell death induction was proportional to the illumination intensity **(Fig. 1C,D and Fig. S1G,H)**, which suggests that the cell death modality is ferroptosis.

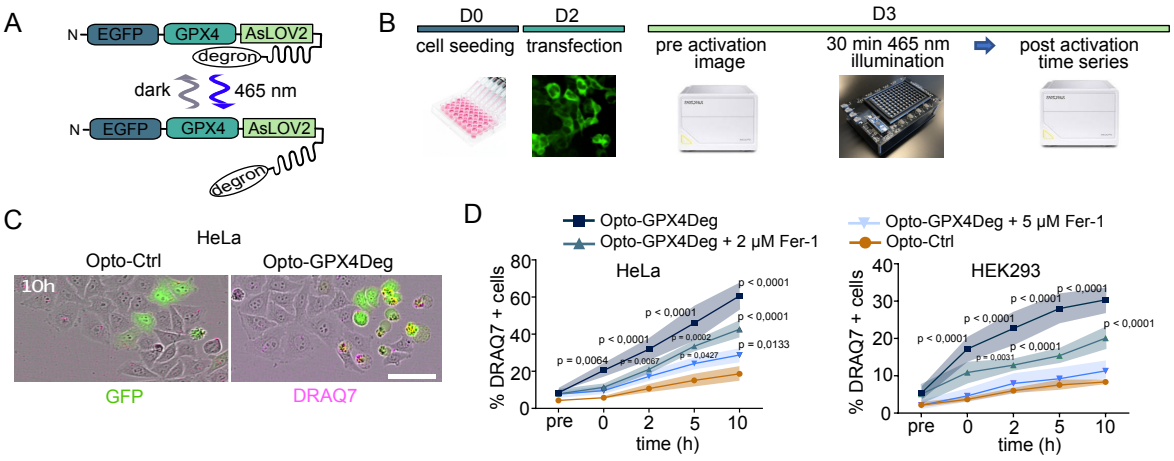

Fig. 1: Light-controlled cell death induction with Opto-GPX4Deg. (A) Design of Opto-GPX4Deg. Opto-GPX4Deg is designed as fusion protein encoding for GPX4 tagged with N-terminal EGFP and a C-terminal LOV domain with a degron sequence at the C-terminus, which only becomes accessible upon blue light illumination. **(B)** Experimental design of high-throughput optogenetic experiments: On day 0, 5000 HeLa or HEK293 cells per well were seeded into each well of 96-well plates. By day 2, the cells were transfected with either Opto-Ctrl or Opto-GPX4Deg. On day 3, a pre-activation image was taken before illuminating the cells for 30 minutes using 100% 465 nm LED intensity of an optoPlate-96. Afterward, a post-activation time series was captured using an S3-Incucyte. **(C)** Representative images of HeLa cells cell death analysis utilizing DRAQ7 (magenta) either expressing Opto-GPX4Deg or Opto-Ctrl (green) 10h post-illumination. Scale bar, 30 µm. **(D)** Cell death kinetics quantification upon optogenetic activation in HeLa and HEK293 cells transfected with Opto-GPX4Deg or Opto-Ctrl and treated or not with Fer-1. DRAQ7 positive cells were normalized to GFP positive cells. Statistical analysis by three-way ANOVA corrected for multiple comparisons using Tukey's multiple comparison test. Exact p-values are shown. All experiments were performed with three independent biological replicates (n=3).

To verify that the fusion construct Opto-GPX4 gets degraded upon optogenetic activation, we transfected HeLa cells with Opto-GPX4Deg or Opto-Ctrl and activated the cells with different illumination durations, whereafter the samples were processed for Western blotting (WB). As postulated, the fusion protein Opto-GPX4Deg got degraded in an illumination duration-dependent manner, which we showed via significantly reduced levels of GFP and GPX4 antibody stainings, but not the control construct. Remarkably, we observed the same trend for endogenous GPX4 **(Fig.**

2A,B). This finding could have different explanations including the existence of an orchestrated mechanism for GPX4 degradation via the proteasome or that the fusion protein might act as a dominant negative isoform that interacts through its degron sequence with endogenous GPX4. As an alternative approach for showing the degradation of the fusion protein, we assessed GFP intensities of individual cells pre-, post- and 24h post-activation, where we again detected a significant GFP intensity reduction in Opto-GPX4Deg expressing cells, but not in the Opto-Ctrl expressing cells **(Fig. 2C,D)**. As GPX4 is a potent anti-ferroptotic regulator, we assessed the GPX4 activity within the Opto-GPX4Deg fusion protein, showing that it maintains partial activity through its ability to hinder cell death in GPX4 KO cells during Fer-1 withdrawal or after tamoxifen-induced GPX4 depletion **(Fig. S1I-K)**. All in all, these findings suggest that Opto-GPX4Deg activation induces cell death via exogenous and endogenous GPX4 degradation.

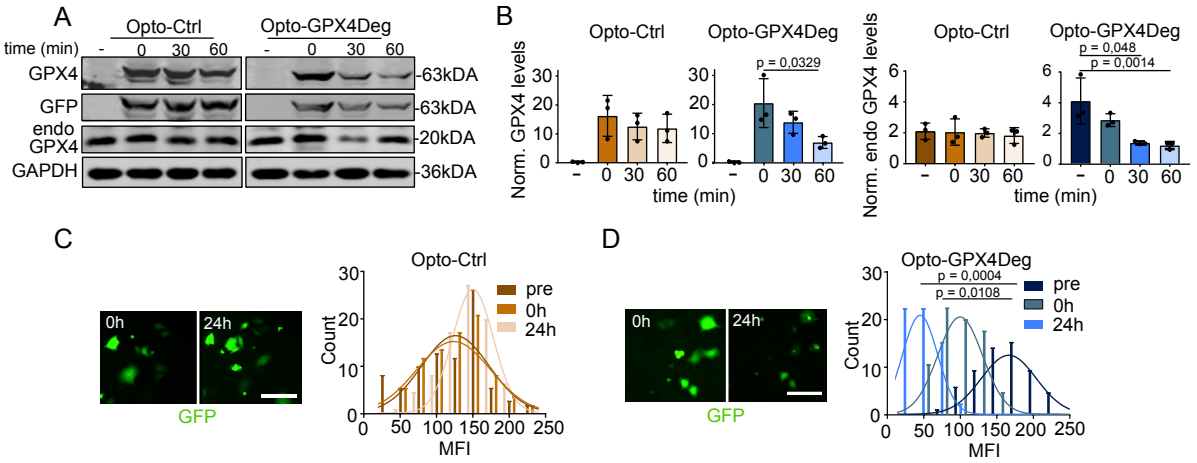

Fig. 2: Optogenetic activation results in the degradation of Opto-GPX4Deg. (A) WB analysis of Opto-GPX4Deg, Opto-Ctrl and endogenous GPX4 protein levels activated or not with indicated illumination times. GAPDH, loading control. **(B)** Quantification of WBs in **(A)**. Protein levels normalized to loading control. Values are displayed as mean ± SD. **(C,D)** Quantification of the Mean Fluorescence Intensity (GFP) in individual cells at indicated times, as a readout Opto-GPX4Deg degradation (8-bit greyscale). Statistical analysis by one-way ANOVA corrected for multiple comparisons using Tukey's multiple comparison test was performed for all experiments. Exact p-values are shown. All experiments were performed with three independent biological replicates (n=3). Error bars, ±SD.

Opto-GPX4 enables ferroptosis regulation at the single-cell level.

A major advantage of optogenetic tools in comparison to conventional drug treatments is next to their tunability and reversibility, the possibility of controlling signaling pathways in single cells without affecting neighboring cells. To test these properties in Opto-GPX4Deg, we adapted the experimental procedure to confocal live cell imaging at the single cell level. In short, we acquired a pre-activation image, whereafter individual Opto-GPX4Deg expressing cells were activated with the FRAP unit of the microscope with a 405 nm laser every 5 min for up to one hour. **(Fig. 3A)**. As expected, single cell activation of Opto-GPX4Deg expressing HEK293 cells robustly induced cell death that could be captured with high spatial and temporal precision **(Fig. 3B)**. As a quantitative readout of single cell death induction, we assessed the time till death using plasma membrane blebbing as a readout. On average, 17 minutes passed from activation to membrane blebbing, which occurred in a narrow distribution of around 13-20 minutes. Cell death induction occurred in activated Opto-GPX4Deg-expressing cells significantly faster compared to cells expressing negative controls, which indicates a specific cell death induction. The negative controls additionally functioned as proximation for photo-toxicity of the illumination conditions, confirming that the used illumination settings were not sufficient for inducing cell death in Opto-GPX4Deg expressing cells. In line with the high-throughput approach **(Fig.1)**, 3 µM Fer-1 administration inhibited cell death induction to control levels, indicating that the cell death modality in this setting is ferroptosis. Importantly, Fer-1 application did not alter the time till death in control samples, nor in an established optogenetics apoptosis setting **(Fig. 3B)** [130]. As an additional control for potential optogenetic tool expression and activation for bystander cells that fall below the fluorescence detection range, we activated seemingly non-transfected bystander cells in the Opto-Ctrl and the Opto-GPX4Deg expressing bulk. The percentage of blebbing cells was comparable between the condition, suggesting that those cells were not or not sufficiently expressing the optogenetic constructs at the time of activation **(Fig. 3D)**.

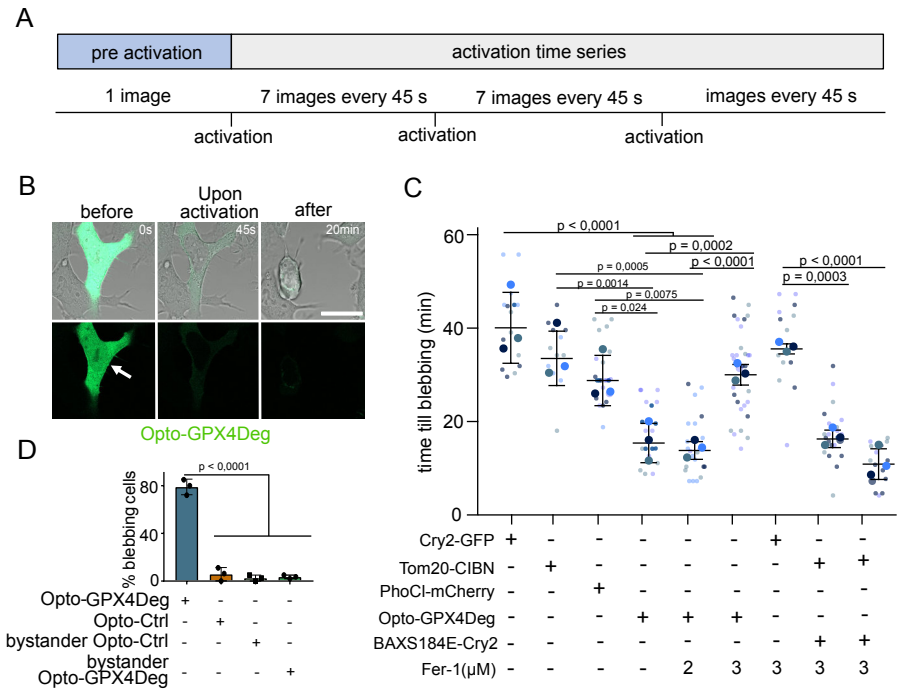

Fig. 3: Single-cell ferroptosis induction using Opto-GPX4Deg. (A) Activation regime of confocal optogenetics cell death experiments: Before optogenetic activation, one pre-activation image was acquired followed by the optogenetic activation using the FRAP unit with 70% intensity of a 405 nm laser with 100 iterations every 5 min for up to one hour. **(B)** Representative images of morphological changes in Opto-GPX4Deg expressing cells upon activation (white arrow). Scale bars, 10 µm. **(C)** Quantification of the time till blebbing as a proxy for cell death induction for the indicated optogenetic constructs, treated with Fer-1 as indicated**.** Big dots represent the replicate averages, small dots represent single-cell measurements in individual replicates. **(K)** Quantification of the percentage of blebbing cells from **(C)** at 25 min after illumination. Bystander refers to non-expressing bystander cells exposed to activating illumination within populations transfected with Opto-GPX4Deg or Opto-Ctrl. Statistical analysis by one-way ANOVA corrected for multiple comparisons using Tukey's multiple comparison test was performed for all experiments. Exact p-values are shown. All experiments were performed with three independent biological replicates (n=3). Error bars, ±SD.

Opto-GPX4Deg activation induces lipid peroxidation in cellular membranes.

To further validate that the Opto-GPX4Deg-induced cell death modality is ferroptosis, we assessed lipid peroxidation, a hallmark of ferroptosis, in cellular membranes. Therefore, we transfected HEK293 cells or not with Opto-GPX4Deg. On the next day, the cells were labeled with C11-Bodipy, a standard method for assessing lipid peroxidation in live cells. Upon oxidation, this membrane-bound, ratiometric fluorescent dye alters its emission properties and is frequently utilized as an indicator for ferroptosis-induced lipid peroxidation[7]. Afterwards, we assessed C11-Bodipy ratios upon optogenetic activation at time points 5 min and 65 min post-activation. We found that single activated Opto-GPX4Deg expressing- and non-transfected bystander cells exhibited detectable levels of lipid peroxidation 5 min post-activation, which returned to normal levels after 1h in non-transfected bystander cells, but activated Opto-GPX4Deg expressing cells at least maintained their elevated C11-Bodipy oxidation ratio, probably due to high activation laser intensity exposure **(Fig. 4A,B)**. The elevated C11-Bodipy ratios of activated Opto-GPX4Deg expressing cells were accompanied by characteristic morphological changes of lytic cell death, whereas non-transfected cells did not change their morphology over time **(Fig. 4A)**. We could also confirm these results using our high-throughput optogenetic pipeline **(Fig. 4C,D)**. Together these results indicate that the light exposure to optogenetically activate Opto-GPX4Deg might contribute to lipid peroxidation and hence to specific ferroptosis induction.

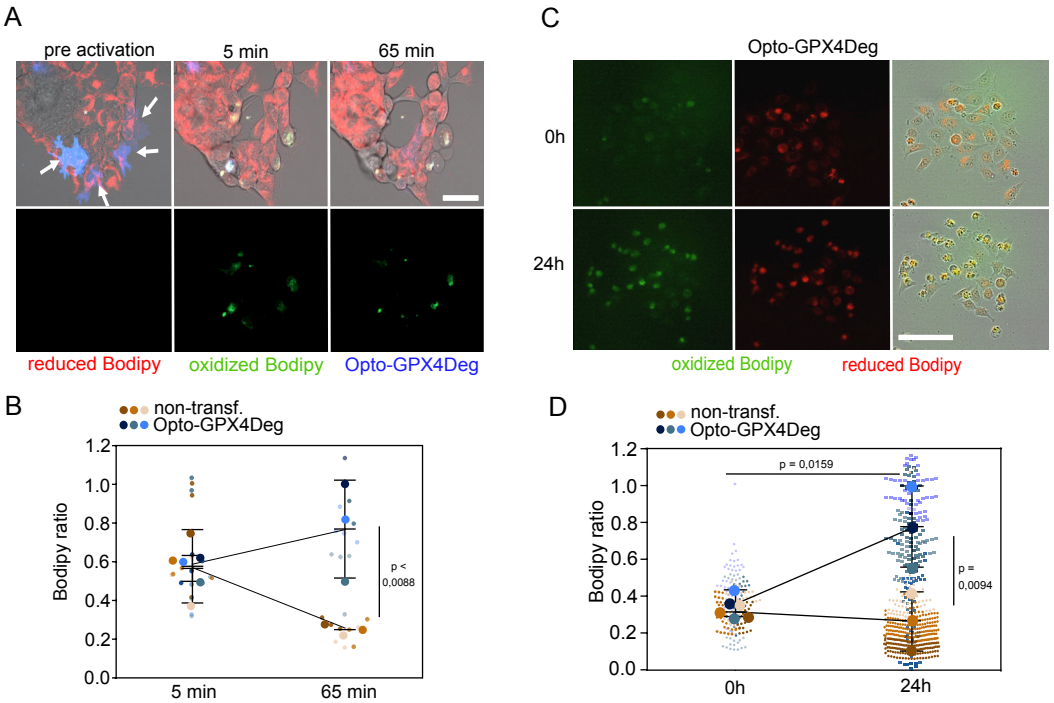

Fig. 4: Optogenetic activation of Opto-GPX4Deg increases lipid peroxidation assessed by C11-Bodipy oxidation. (A) Images showing the emergence of green (oxidized) C11-Bodipy fluorescence upon illumination of individual cells. Reduced C11-Bodipy is shown in red. White arrows, activated Opto-GPX4Deg cells. White asterisk, activated, non-transfected control cells. Scale bar, 50 µm. **(C)** Images of C11-Bodipy oxidation (green) upon bulk illumination of expressing or not Opto-GPX4Deg. Reduced C11-Bodipy is shown in red. Scale bar, 80 µm. **(B,D)** C11-Bodipy oxidation ratio calculated by normalizing green with green + red C11-Bodipy fluorescence signal. Big dots represent replicate averages, small data dots represent single-cell measurements in individual replicates. Values are displayed as mean ± SD. Statistical analysis by one-way ANOVA corrected for multiple comparisons using Tukey's multiple comparison test. Exact p-values are shown. All experiments were performed with three independent biological replicates (n=3).

As an alternative approach for testing specific ferroptosis induction upon Opto-GPX4Deg activation, we measured lipid peroxidation by lipidomics analysis. Therefore, we upscaled the high-throughput pipeline to a 6-well-plate format and incubated the cells upon transfection for two days before activating or not Opto-GPX4Deg- or Opto-Ctrl expressing bulks, after which the samples were processed for lipidomics analysis or WB. Western blotting was performed as quality control and showed as in Fig. 2A,B a significant reduction in Opto-GPX4Deg levels and endogenous GPX4, but not in the Opto-Ctrl transfected bulk. Consistent with the C11-Bodipy experiments, mass spectrometry analysis also revealed a significant increase in oxidized lipid species in the Opto-GPX4Deg samples, but not in the negative controls, whereby we detected the highest enrichments in oxidized phosphatidylcholine (PC) species, which is in line with previous work performed in HeLa cells **(Fig. 5D)**[131]. Moreover, fatty acids mass spectrometry uncovered a global reduction in fatty acid species **(Fig. 5E)**. Together, these findings show that Opto-GPX4 induced cell death is coincident with increased lipid peroxidation levels, which further proves that the cell death modality is ferroptosis.

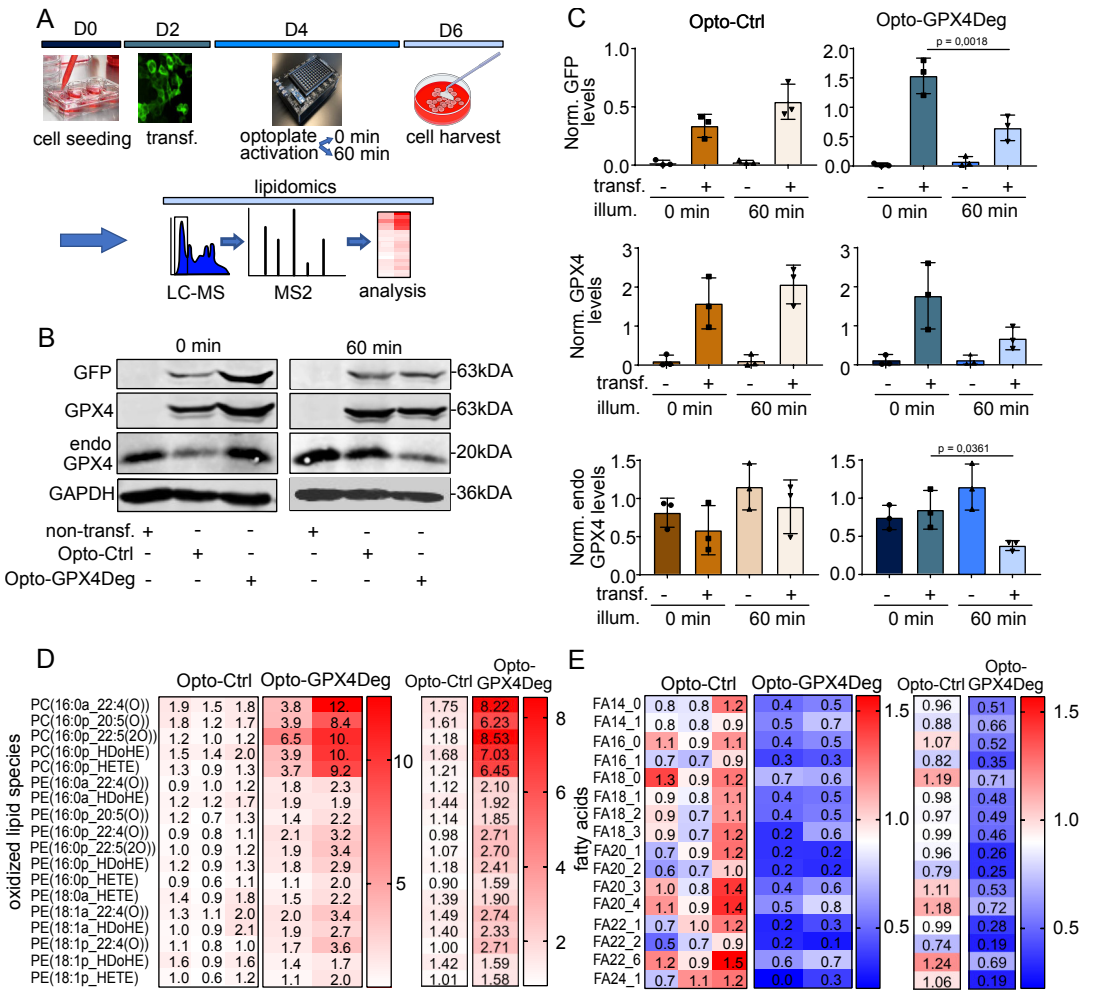

Fig. 5: Optogenetic activation of Opto-GPX4Deg increases lipid peroxidation assessed by mass spectrometry. (A) Workflow of lipidomic experiments: On day 0, 1x10^5 HeLa cells/well were seeded into 6-well plates. By day 2, HeLa cells were transfected either with Opto-Ctrl, Opto-GPX4Deg or not transfected. Transfected cell populations were illuminated or not for 60 min with 100% 465 nm LED intensity using an optoPlate-96. After 48h, the cells were harvested, and samples were prepared for WB and lipidomics. **(B)** Representative WB shows the illumination-dependent degradation of the Opto-GPX4Deg construct. GAPDH, loading control. **(C)** Protein levels quantification of GFP, GPX4 and endogenous GPX4 of the WB in **(B)**. Protein levels normalized to loading control. –, non-transfected, or transfected as indicated with Opto-Ctrl or Opto-GPX4Deg. Statistical analysis by one-way ANOVA corrected for multiple comparisons using Tukey's multiple comparison test (rest) or parametric t-test (endo GPX4). Exact p-values are shown. All experiments were performed with three independent biological replicates (n=3). Values as mean ± SD. **(D,E)** Mass spectrometry analysis of oxidized lipids and fatty acids, respectively. Fold change in the heat map was calculated by dividing lipid species upon illumination by the non-illuminated control for the individual replicates (left) and average (right). All experiments were performed with at least two independent biological replicates (n=3).

Ferroptotic cells are capable of inducing ferroptosis in neighboring cells.

An increasing number of studies report that ferroptosis can spread within cell populations *in vitro* and contribute to the propagation of necrosis in diseased tissues[89,90], but recently a study also demonstrated that ferroptosis propagation can play a role in normal physiology during development[88]. However, all those studies investigated ferroptosis propagation in the context of cell populations with altered ferroptosis sensitivities due to conventional drug interventions that can affect all cells in the population. We hypothesized that our Opto-GPX4Deg system could circumvent these limitations and enable the study of ferroptosis propagation in a more physiologically relevant setting. Strikingly, we observed that after a lag time of around three hours not only activated Opto-GPX4Deg cells but also non-transfected cells, which we call from here on bystander cells, started to die, which did not occur in the Opto-Ctrl transfected cell populations **(Fig. 6)**. Importantly, we ruled out that cells expressing Opto-GPX4Deg below the fluorescence detection range at the activation time point contributed to this phenomenon **(Fig. 3D)**.

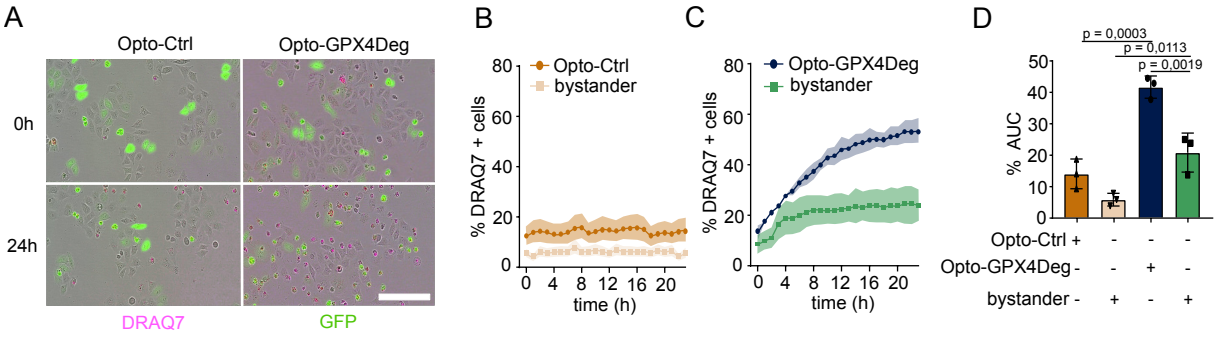

Fig. 6: Ferroptotic cells induce ferroptosis in bystander cells. (A) Images showing cell death (DRAQ7, magenta) in bystander HeLa cells (GFP negative) at 0h and 24h post-illumination in Opto-GPX4Deg and Opto-Ctrl samples. **(B-D)** %DRAQ7 positive cells over time for indicated cell populations from experiments in **(A)**. **(D)** To facilitate statistical comparison of the different experimental settings, we calculated the % Area Under the Curve (AUC) for the cell death kinetics graphs of the different cell populations. One-way ANOVA corrected for multiple comparisons using Tukey's multiple comparison test. Exact p-values are shown. All experiments were performed with three independent biological replicates (n=3). Values as mean ± SD.

These results indicate that activated Opto-GPX4Deg-expressing cells die first, followed by bystander cells. If there were a causal connection between those events, one would expect a heterogeneous distribution of cell death within the bystander cell population. Accordingly, we assessed the clustering tendency of our dataset via Hopkins statistics. In short, Hopkins statistics assesses data clustering by comparing the distance between real data points to their nearest neighbors with the distance from random points to the nearest real data points. When the data is not clustered, the distances from real points to each other and from random points to real points are similar, resulting in a Hopkins statistic of around 0.5. In tightly clustered data, real points are much closer to their neighbors than random points are to real points, yielding a statistic close to 1.0[132]. Intriguingly, Hopkins analysis of our data set revealed that cell death in activated Opto-GPX4Deg expressing cell populations mainly occurred in clusters (value = 0.67), whereas cell death in the Opto-Ctrl transfected populations was randomly distributed (value = 0.43) **(Fig. 7A)**. As a consequential analysis, we investigated whether Opto-GPX4Deg activation induces cell death preferentially in bystander cells that are in close proximity. Indeed, our analysis showed, to our surprise, that the distance from dead Opto-GPX4Deg expressing cells to dead bystander cells was significantly shorter compared to those distances in Opto-Ctrl transfected populations **(Fig. 7B)** and the measured distance was consistent with the average diameter of HeLa cells of around 23 µm **(Fig. 7D,E)**. This result hinted at the direction that cells undergoing Opto-GPX4Deg triggered ferroptosis were able to induce cell death in bystander cells in their close vicinity. We could not observe a similar behavior in an optogenetics apoptosis setting, which indicates that the propagation of cell death to neighboring cells is a specific trait of ferroptosis **(Fig. 7C)**.

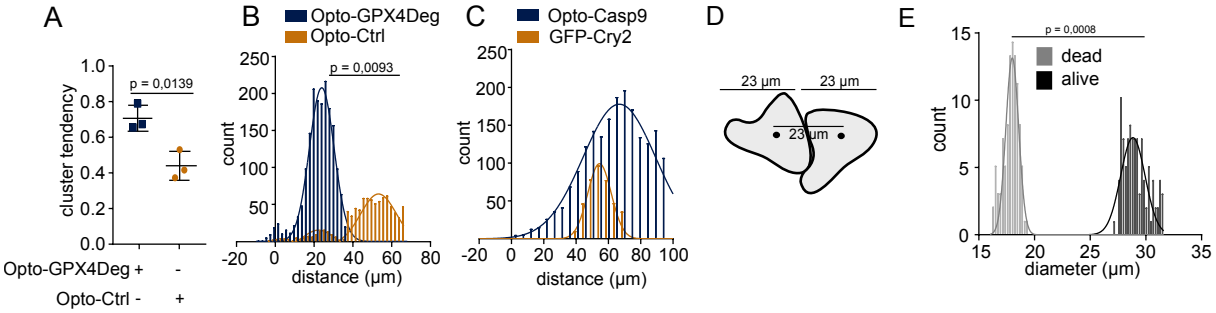

Fig. 7: Direct adjacent bystander cells to activated, dead Opto-GPX4Deg expressing cells undergo cell death. (A) Hopkins statistical analysis was used for assessing the clustering tendency of the data sets. Statistical analysis by parametric t-test. **(B)** Distribution of distances between dead cells expressing Opto-GPX4Deg or Opto-Ctrl to dead, bystander cells from experiments in **(Fig. 6)**. **(G)** Same as in **(F)** but using Opto-Casp9 for light-driven apoptosis induction and respective control construct. Statistical analysis by parametric t-test. Values are displayed as mean ± SD. **(D)** Scheme showing the average diameter of HeLa cells as well as the average distance between neighboring HeLa cells. **(E)** Distribution of cell diameters of living and dead HeLa cells derived from Fig. 6. Statistical analysis by parametric t-test. Exact p-values are shown. All experiments were performed with three independent biological replicates (n=3). Values are displayed as mean ± SD.

We next aimed to elucidate the cell death modality by which adjacent bystander cells die upon Opto-GPX4Deg triggered ferroptosis. To this aim, we designed a more complex experimental setup that allowed us to simultaneously assess the kinetics of membrane oxidation and cell death using a modified Opto-GPX4Deg version, where we exchanged GFP with BFP2, in combination with C11-Bodipy staining. Membrane oxidation and cell death kinetics in activated Opto-GPX4Deg expressing cells showed first an accumulation of oxidized C11-Bodipy, followed by plasma membrane rupture and cell death. Bystander cells directly adjacent to these ferroptotic cells also accumulated oxidized lipids with a delay and eventually died. Subsequently, we could observe increased lipid ROS and cell death in their direct neighboring cells over time. Importantly, Fer-1 treatment directly upon Opto-GPX4Deg activation was, as expected, not sufficient to hinder ferroptosis in Opto-GPX4Deg expressing cells, but largely diminished lipid oxidation and cell death in bystander cells **(Fig. 8A-E)**. In line with that, control samples only exhibited insignificant amounts of lipid peroxidation and no cell death propagation **(Fig. S2 and S3A)**. Intriguingly, we measured a mean distance between dead bystander cells, which again corresponded to that of neighboring cells. Our results therefore suggest that bystander cells that were directly adjacent to cells that died by Opto-GPX4Deg activation also underwent ferroptosis. Furthermore, ferroptotic bystander cells were able to pass lipid oxidation and ferroptosis on to other

directly adjacent bystander cells. Collectively, our data demonstrates that ferroptosis can propagate across cell populations.

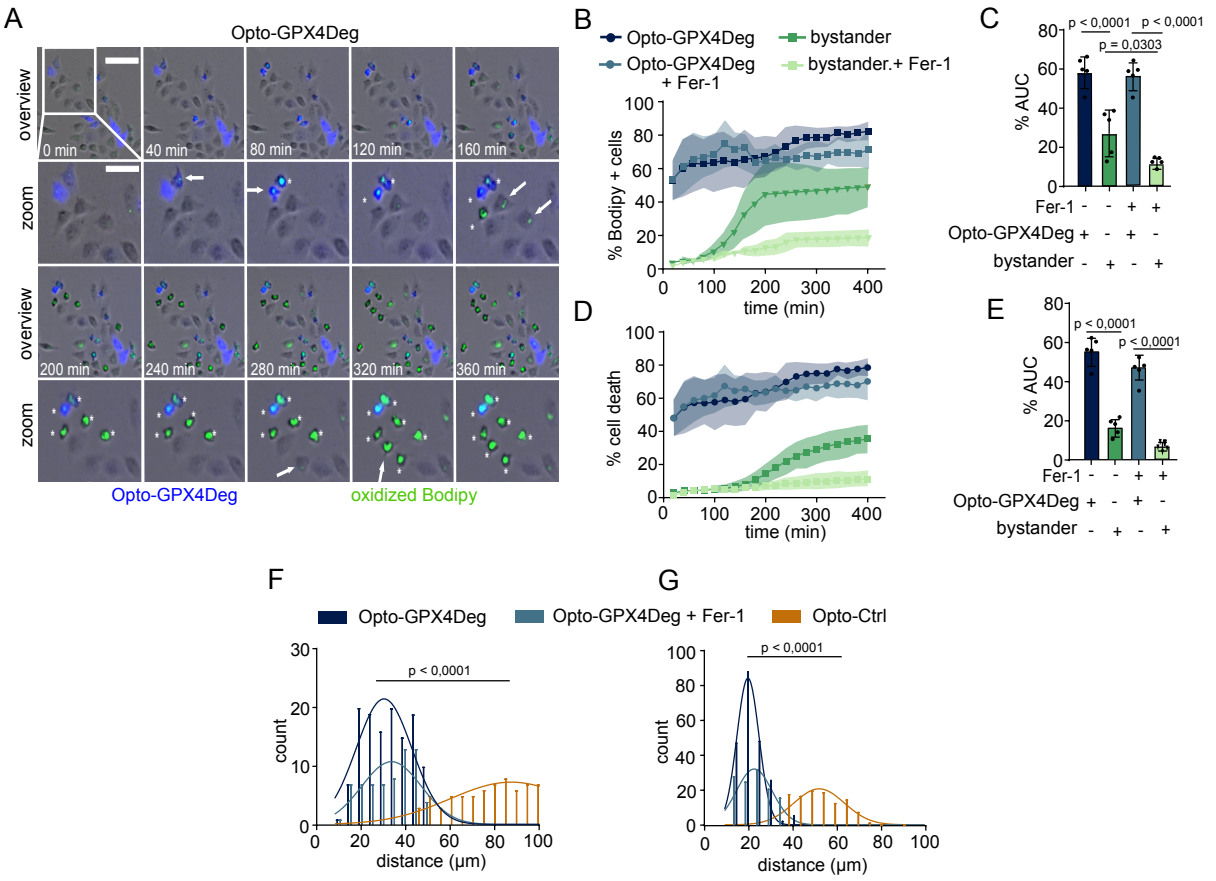

Fig. 8: Bystander cells adjacent to ferroptotic cells die by ferroptosis and are capable of propagating ferroptosis to their neighbors. (A) Lipid peroxidation spread and cell death time series analysis. Opto-GPX4Deg, blue; oxidized C11-Bodipy, green. White arrows, cells with C11-Bodipy oxidation. White asterisks, dead cells. Scale bars, 100 µm for overview and 50 µm for zoom. **(B,D)** %C11-Bodipy positive (oxidized C11-Bodipy) cells **(B)** and %cell death **(D)** over time in the indicated populations treated or not with 5 µM Fer-1. **(C,E)** %AUC of the different cell populations in **(B,D)**. Statistical analysis by one-way ANOVA corrected for multiple comparisons using Tukey's multiple comparison test. Values are displayed as mean ± SD. **(F,G)** Distance distribution between dead, Optp-GPX4Deg expressing cells and dead, bystander cells **(F)**, and distance distribution between dead, bystander cells **(G)**. Statistical analysis by one-way ANOVA corrected for multiple comparisons using Tukey's multiple comparison test. Exact p-values are shown. All experiments were performed with three independent biological replicates (n=3) except in **(B-E)** five independent biological replicates (n=5) were performed. Values are displayed as mean ± SD.

Given that proximity is a key parameter for ferroptosis propagation, we hypothesized that increasing cell confluency should render bystander cells more sensitive to ferroptosis. Intriguingly, we could confirm this notion by finding that bystander HeLa cells were indeed more susceptible to cell death induced by neighboring cells that died by Opto-GPX4Deg activation **(Fig. 9A,B)**. Additionally, we could also show an increased sensitivity towards ferroptosis in RSL3-treated HeLa cells at higher cell confluency **(Fig. 9C,D)**. Consistent with previous reports that extremely high cell densities promote the survival of GPX4 (KO) cells[27], we also observed a desensitization to ferroptosis induction by Opto-GPX4Deg and RSL3 at 100% confluency.

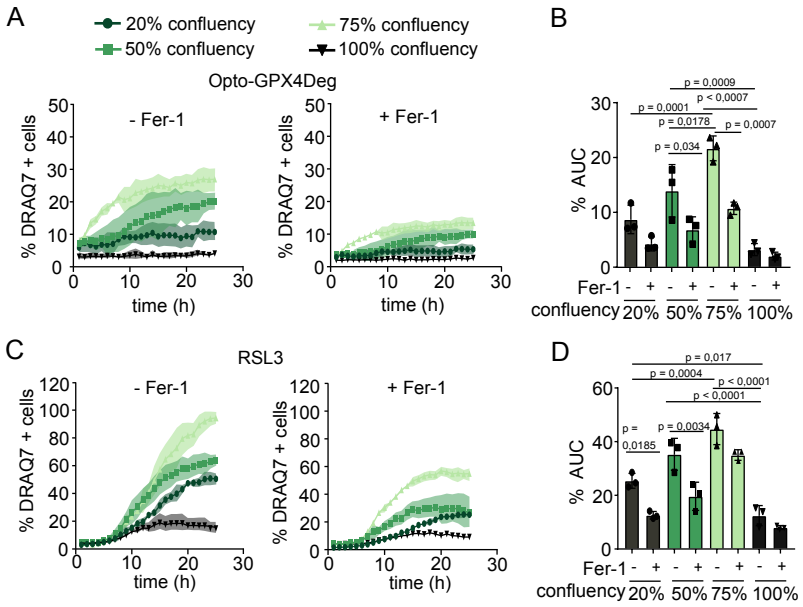

Fig.9: Higher cell confluency renders HeLa cells more sensitive to ferroptosis. (A) %DRAQ7 positive HeLa cells upon optogenetic activation over time transfected with Opto-GPX4Deg and seeded at the indicated confluency, treated or not with 5 µM Fer-1. **(B)** %AUC for the populations in **(A). (C)** %DRAQ7 positive cells over time for HeLa cells seeded at indicated confluency and treated with 4 µM RSL3 and 5 µM Fer-1 as indicated. **(D)** %AUC for the different populations in **(C)**. Statistical analysis by one-way ANOVA corrected for multiple comparisons using Tukey's multiple comparison test. Exact p-values are shown. All experiments were performed with three independent biological replicates (n=3). Values are displayed as mean ± SD.

Since our previous results established a requirement of close cell proximity in ferroptosis spread, we wondered whether physical contact between neighboring cells might be directly involved in ferroptosis propagation. To test this, we transferred as part of a collaboration with F. Isil Yapici conditioned medium of ferroptotic cells from two different genetic systems onto healthy MEF cells. For the SCLC GPX4 KO systems, ferroptosis was induced by Fer-1 withdrawal, whereas the tamoxifen-inducible GPX4 KO Pfa1 system was treated with tamoxifen to trigger ferroptosis. In line with our notion that physical contact might be necessary for ferroptosis spread, conditioned medium containing molecules released from ferroptotic cells was not sufficient as a death signal in recipient cells. However, we cannot discard that instability of molecules in the supernatant or local concentration differences of molecules are responsible for the lack of ferroptosis induction by the conditioned media **(Fig. 10)**.

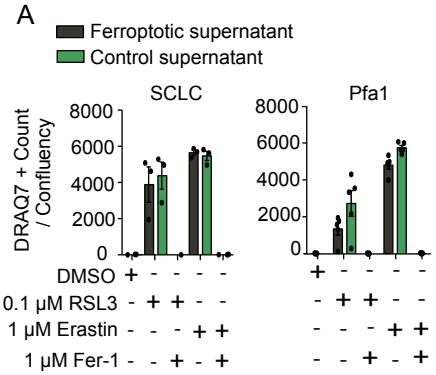

Fig. 10: Ferroptotic supernatant does not result in a death signal in recipient cells. (A) Supernatants were obtained from either ferroptotic or control cells derived from murine small cell lung cancer (SCLC) GPX4 knockout cells under Fer-1 withdrawal (left) or from MEFs with inducible GPX4 knockout (Pfa1) treated with 1 µM 4-hydroxytamoxifen for 72 hours (right panel). These supernatants were transferred onto WT MEFs, which were subsequently treated as indicated. Cell death was assessed by DRAQ7 staining and quantified by dividing the DRAQ7 object count by confluency. One-way ANOVA corrected for multiple comparisons using Tukey's multiple comparison test. All experiments were performed with three independent biological replicates (n=3). Values are displayed as mean ± SD.

Because cytosolic calcium fluxes were shown to be crucial for ferroptosis execution [41,90], and have been observed in ferroptosis propagation that was induced by conventional drug treatments, we wondered whether calcium could also act as a local trigger for ferroptosis propagation to neighboring cells when the cell populations have not been sensitized to ferroptosis before. Although we could replicate our

previous work[41] by finding that Opto-GPX4Deg cells undergoing ferroptosis exhibit increased cytosolic calcium measured with the calcium indicator Fluo-4-AM, we failed to detect with our system significant calcium influx in adjacent bystander cells during the time window in which they maintained their integrity, indicating that paracrine calcium fluxes are not involved in ferroptosis propagation **(Fig. 11A,B)**. However, removing extracellular calcium prevented ferroptosis propagation without altering the cellular intrinsic ferroptosis susceptibility as Opto-GPX4Deg expressing cells cell death levels did not change in comparison to the control condition **(Fig. 11C,D and Fig. S3B,C)**, suggesting that extracellular calcium plays a role in ferroptosis propagation. This finding is of particular interest as calcium was found to be crucial for the formation of adhesive cell-cell contacts mediated by cadherins, with extracellular calcium depletion abolishing adhesive cell-cell contacts and thereby likely disturbing spatial distance between cells.

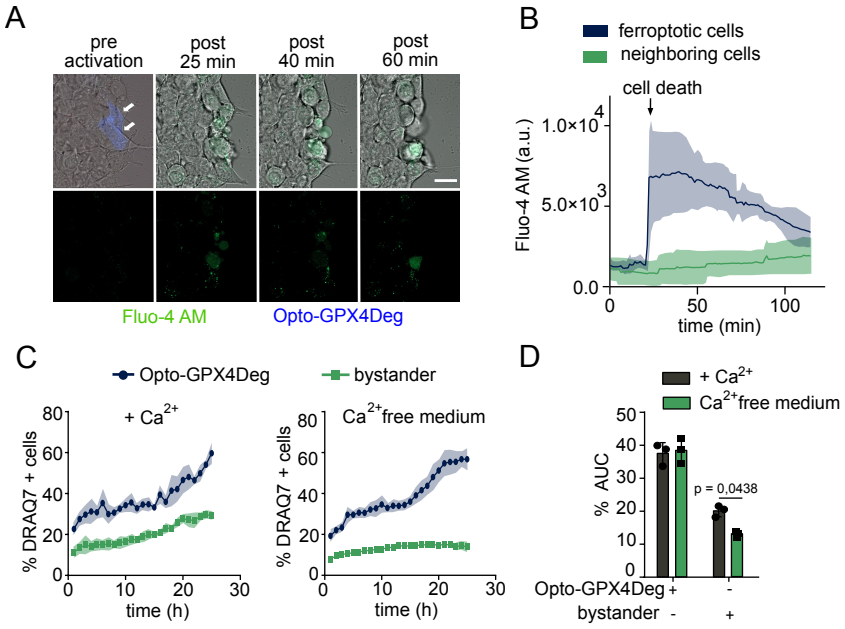

Fig. 11: Extracellular Ca^{2+} plays a role in ferroptosis propagation. (A) Time series of cytosolic Ca^{2+} fluxes in HEK293 cells transfected with Opto-GPX4Deg (white arrows) and stained with 1 µM Fluo4-AM (green). Scale bar, 50 µm. **(B)** Single-cell analysis of the Fluo4-AM mean fluorescence intensity in **(A)**. n= 5 ferroptotic and 40 neighboring cells. a.u., arbitrary units. **(C)** %DRAQ7 positive HeLa cells for indicated cell populations with (left) or without Ca^{2+} (right) in the medium over time. **(D)** %AUC for the populations in **(C)**. **(D)** parametric t-test was performed. Exact p-values are shown. All experiments were performed with three independent biological replicates (n=3).

Following up on these results, we next investigated the role of cell-cell contacts in ferroptosis propagation through the disruption of Ca^{2+}-dependent adhesive cell-cell contacts by α-catenin depletion, which is a crucial component of cadherin complexes[133]. Strikingly, experiments of light-induced Opto-GPX4Deg activation in HeLa cells revealed that ferroptosis propagation from Opto-GPX4Deg expressing cells to bystander cells was fully inhibited in α-catenin knockdown (KD) populations, but not in control bulks that were transfected with scrambled siRNA **(Fig. 12A,B and Fig. S4A)**. We could recapitulate these findings when repeating the α-catenin KD experiment in SCLC cells **(Fig. 12C,D and Fig. S4B)**. In contrast, we only observed limited ferroptosis propagation in HT-29 WT cells **(Fig. 12E,F and Fig. S4B)**. Interestingly, we observed a correlation between E-cadherin expression levels and the ability of these cell lines to sustain ferroptosis propagation, which is in accord with previous reports that attribute a protective role to E-cadherin in ferroptosis **(Fig. 12G,H)**. To get a better understanding of the paradox between E-cadherin's role in preventing ferroptosis propagation and its function in forming cell-cell contacts, we aimed to explore the underlying mechanism in more detail.

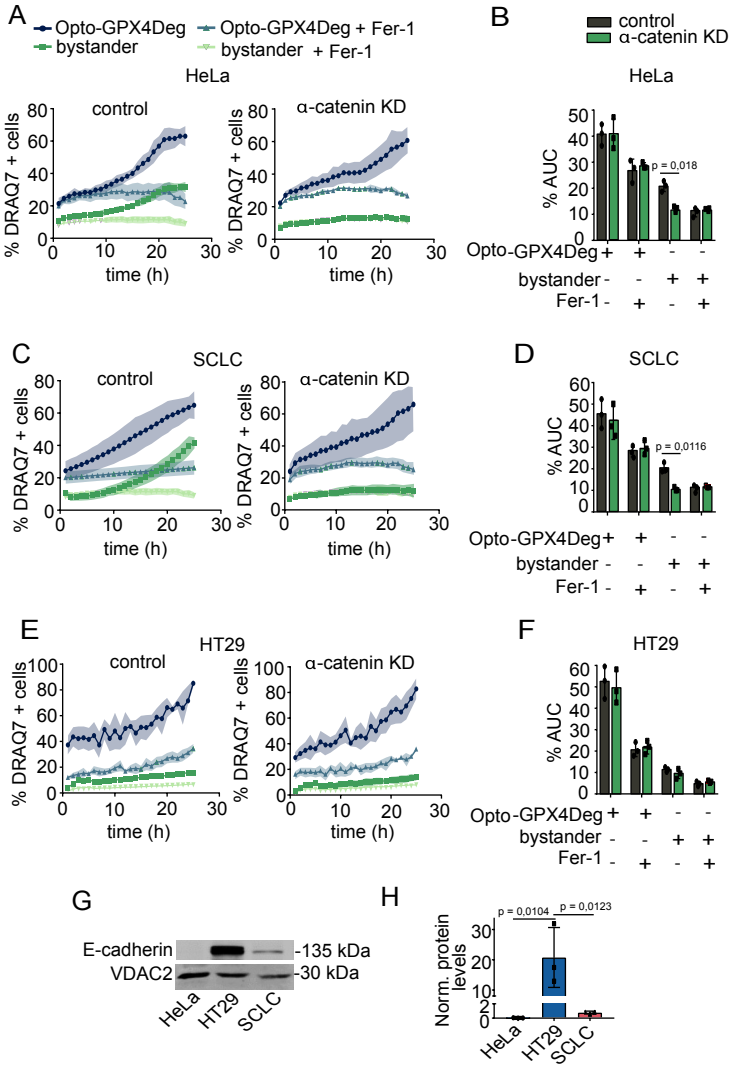

Fig.12: Disruption of cell-cell contacts by α-catenin depletion abrogates ferroptosis propagation. Opto-GPX4Deg and bystander HeLa **(A,B),** SCLC **(C,D)**, or HT29 **(E,F)** cells were transfected with either siRNA against α-catenin or scramble siRNA (control), and treated or not with 5 µM Fer-1. **(A, C, E)** %DRAQ7 positive cells in α-catenin KD and control samples over time. **(B, D, F)** %AUC for indicated populations. Statistical analysis by one-way ANOVA corrected for multiple comparisons using Tukey's multiple comparison test. Exact p-values are shown. All experiments were performed with three independent biological replicates (n=3). Values are displayed as mean ± SD.

As expected, exogenous E-cadherin expression completely abrogated ferroptosis propagation in HeLa cells, while not altering the sensitivity of Opto-GPX4Deg expressing cells undergoing light-induced ferroptosis. However, overexpression of other classical cadherins including P- and N-cadherin failed to protect from ferroptosis propagation to bystander cells, suggesting that E-cadherin exclusively, but not other cadherins, has a specific role in preventing ferroptosis spread, while not altering the intrinsic ferroptosis sensitivity of individual cells. Surprisingly, an E-cadherin mutant lacking the catenin binding domain (CBD), which is defective in sustaining cell-cell adhesion by being unable to bind α-catenin, was still sufficient to hinder ferroptosis propagation **(Fig. 13)**.

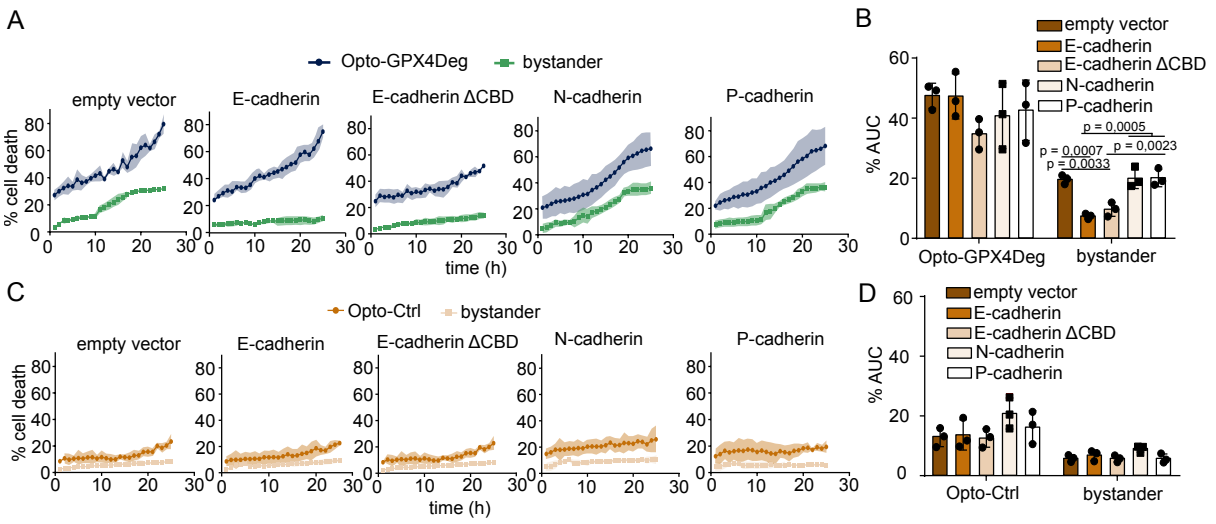

Fig.13: The signaling function of E-cadherin is required for inhibiting ferroptosis. Cell death kinetics in Opto-GPX4Deg **(A)** or Opto-Ctrl **(C)** expressing HeLa cells transfected with RFP-tagged empty vector, WT E-cadherin, E-cadherin ΔCBD mutant, WT N-cadherin or WT P-cadherin. **(B,D)** %AUC for the cell populations in **(A,C)**. Statistical analysis by one-way ANOVA corrected for multiple comparisons using Tukey's multiple comparison test. Exact p-values are shown. All experiments were performed with three independent biological replicates (n=3). Values are displayed as mean ± SD.

A recent study found that the depletion of E-cadherin increases ferroptosis sensitivity by disturbing the cadherin adhesion complex, which in turn would activate the transcription factor YAP and subsequently upregulate pro-ferroptosis factors like ACSL4 and TFRC. In this scenario, we were interested in how YAP is regulated in our α-catenin KD system, where the cadherin adhesion complex is also disrupted[82]. We found that α-catenin KD also activated YAP[134], which we demonstrated by increased nuclear YAP alongside a reduction in phosphorylated YAP. But in contrast to this model, YAP activation resulted in the abrogation of ferroptosis propagation. Furthermore, we detected increased protein levels of GPX4 and/or FSP1, both known for their ferroptosis protective function **(Fig. 14)**. Interestingly, overexpression of the CBD E-cadherin mutant also resulted in YAP activation in HeLa cells while inhibiting ferroptosis propagation **(Fig. S5)**. Together these data uncover that the role of E-cadherin in ferroptosis is cell-cell adhesion independent and can likely be ascribed to its signaling functions[135,136].

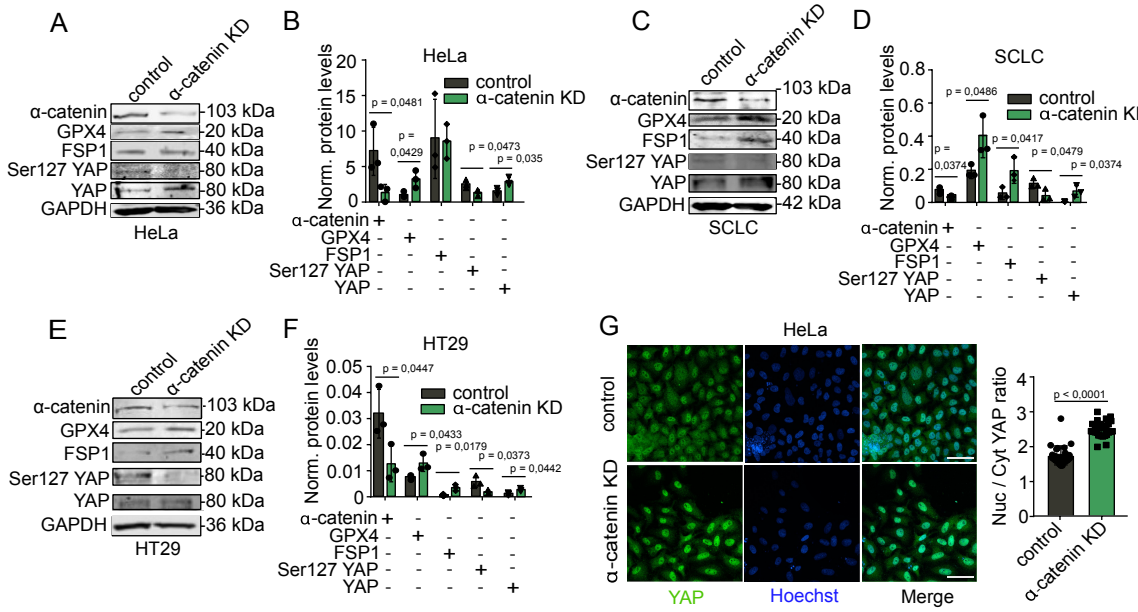

Fig.14: α-catenin KD leads to YAP activation. HeLa, SCLC, or HT29 cells were transfected with either siRNA against α-catenin or scramble siRNA (control). **(A, C, E)** WB analysis of indicated protein levels in α-catenin KD and control cells. **(B, D, F)** Quantification of WB in **(A, C, E).** Protein levels normalized to loading control. **(G)** Immunofluorescence staining of YAP in α-catenin KD or control HeLa cells. Nuclear translocation quantification by comparison of nucleus/cytosol (Nuc/Cyt) YAP ratio in α-catenin KD or control HeLa cells. Green, YAP; blue, Hoechst as nuclear staining. Statistical analysis by parametric t-test. Exact p-values are shown. All experiments were performed with three independent biological replicates (n=3). Values are displayed as mean ± SD.

To validate the findings from the α-catenin KD experiments and to demonstrate the necessity of α-catenin for ferroptosis propagation, we created α-catenin knockout (KO) HeLa cells and performed reconstitution experiments, in which we reintroduced them with exogenous wild-type (WT) and mutant versions of α-catenin. We utilized mutants lacking the vinculin binding site (ΔVBS), the β-catenin binding site (Δβ-catenin), or the F-actin binding site (ΔF-actin) to either fully or partially disrupt cadherin-dependent cell-cell contacts. The Δβ-catenin and ΔF-actin mutants entirely abolish adhesive cell-cell contacts as the complex that mediates the connection of cadherins to the cytoskeleton is disrupted, whereas the ΔVBS mutant partially retains adhesive cell-cell contacts, because its direct F-actin binding function, but not to vinculin, stays intact. We could recapitulate the results from the α-catenin KD experiments, meaning that we found that ferroptosis propagation did not occur in α-catenin KO cells **(Fig. S6)**. Furthermore, WT α-catenin reconstitution resulted in complete reestablished ferroptosis propagation, whereas the Δß-catenin or ΔF-actin mutants were incapable of rescuing ferroptosis spread. However, reconstitution with the ΔVBS mutant resulted in partial restoration of ferroptosis propagation **(Fig. 15)**. These data demonstrate that the disturbance of α-catenin-mediated cell-cell contacts by genetic means blocks ferroptosis propagation.

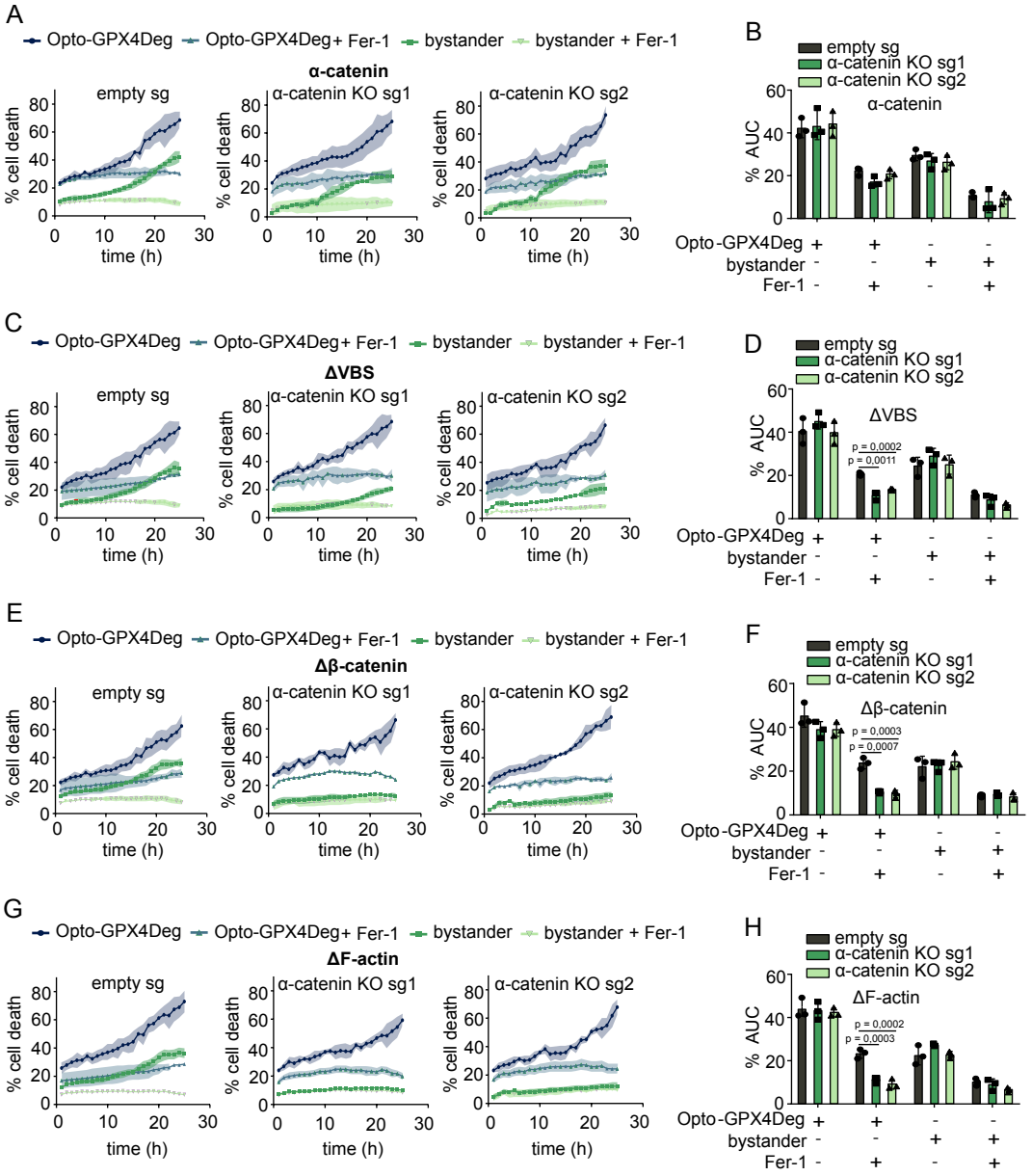

Fig. 15: Reconstitution with α-catenin rescues ferroptosis propagation in α-catenin KO HeLa cells. (A, C, E, G) Cell death kinetics for activated Opto-GPX4Deg and bystander HeLa KO clones (sg1, sg2) or CRISPR control (empty sg) reconstituted with exogenous WT or mutant α-catenin treated or not with 5 µM Fer-1. **(B, D, F, H)** %AUC for indicated cell populations. Statistical analysis by one-way ANOVA corrected for multiple comparisons using Tukey's multiple comparison test. Exact p-values are shown. All experiments were performed with three independent biological replicates (n=3). Values are displayed as mean ± SD.

Our data so far indicated that the spread of lipid peroxidation between adjacent cells, which is required for ferroptosis propagation, is strictly dependent on the close proximity of their plasma membranes. Accordingly, increasing membrane contact areas by chemical means should result in ferroptosis propagation restoration in α-catenin-depleted cells. To test this hypothesis, we utilized blebbistatin to increase

cellular volumes by inhibiting their cortex contractility, causing so increased contact areas between cells. Intriguingly, blebbistatin indeed restored ferroptosis propagation in light-activated α-catenin-depleted Opto-GPX4Deg samples and further enhanced ferroptosis propagation in the scrambled siRNA bulk due to increased cell-cell proximity **(Fig. 16 and Fig. S8)**.

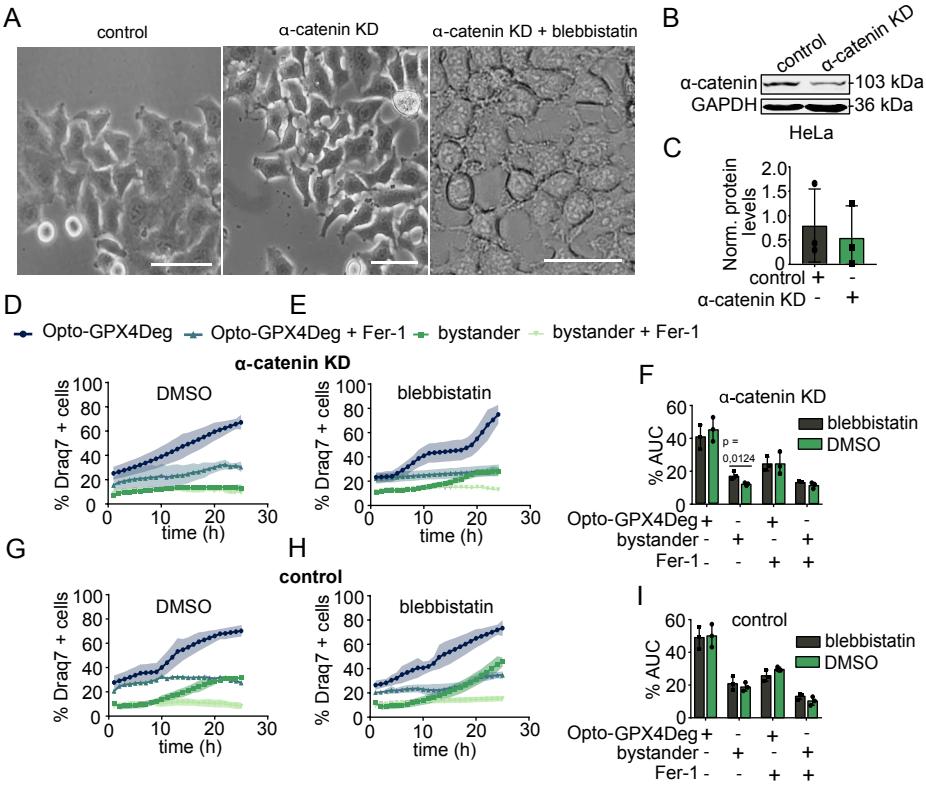

Fig. 16: Increasing cell-cell contact areas promote ferroptosis propagation. (A) Representative images of HeLa cells transfected with a control siRNA or against α-catenin treated or not with 10 µM blebbistatin for one hour. Scale bar, 30 µm. **(B)** WB analysis showing α-catenin KD. **(C)** Quantification of WB in **(B)**, normalized to loading control. Statistical analysis by parametric t-test. **(D,E,G,H)** Kinetics of cell death for activated Opto-GPX4Deg (D,E,G,H) and bystander HeLa cells transfected with siRNA against in α-catenin or scrambled siRNA (control), and treated or not with 5 µM Fer-1 and/or 10 µM blebbistatin. **(F,I)** %AUC for the indicated populations in **(D,E,G,H)**. Statistical analysis by one-way ANOVA corrected for multiple comparisons using Tukey's multiple comparison test. Exact p-values are shown. All experiments were performed with three independent biological replicates (n=3). Values as mean ± SD.

Iron-dependent lipid peroxidation spread across apposed membranes mediates ferroptosis propagation

Alternatively, bridging the distance between cells by utilizing a membrane containing oxidizable unsaturated lipids that enable the sustained spread of lipid peroxidation should also enhance ferroptosis propagation **(Fig. 17A)**. Therefore, we seeded HeLa cells on a lipid bilayer or glass with the same density and induced light-controlled ferroptosis via Opto-GPX4Deg. Intriguingly, we found that both the propagation of lipid peroxidation and ferroptotic cell death was accelerated in cells seeded on the lipid bilayer compared to cells seeded on glass, without altering the intrinsic ferroptosis sensitivity of individual cells **(Fig. 17B-I)**.

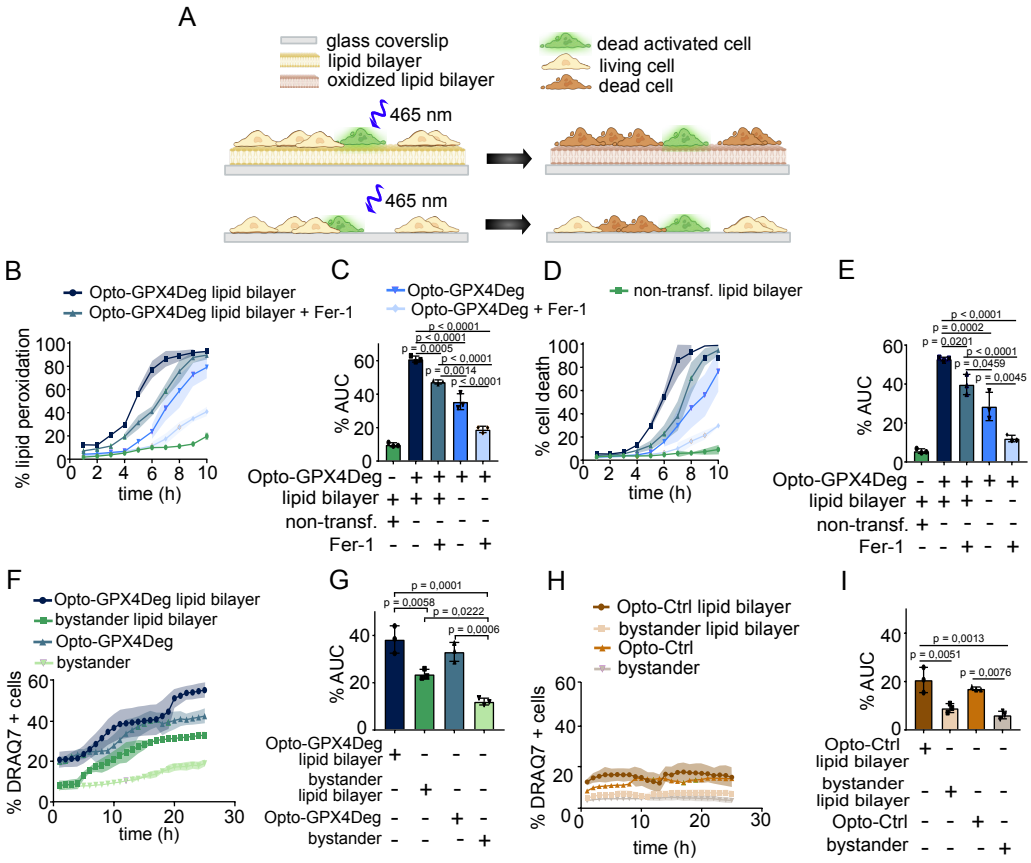

Fig.17: Bridging HeLa cells via a lipid layer renders them more susceptible to ferroptosis propagation. (A) Illustration of experimental design. HeLa cells were transfected with Opto-Ctrl or Opto-GPX4Deg and seeded on a supported lipid bilayer or directly glass and subsequently exposed to activating illumination. The lipid bilayer facilitates the diffusion of oxidized lipids by acting as a membrane bridge between cells. **(B-E)** Kinetics of C11-Bodipy oxidation **(B)** and cell death **(D)** for activated Opto-GPX4Deg and bystander HeLa cells grown on glass or a supported lipid bilayer and treated or not with 5 µM Fer-1. **(C, E)** %AUC for the indicated cell populations. Kinetics of cell death for activated Opto-GPX4Deg **(F)** or Opto-Ctrl for the indicated HeLa cell populations grown or not on a lipid bilayer and treated or not with 5 µM Fer-1. **(G,H)** %AUC for the indicated cell populations. Statistical analysis by one-way ANOVA

corrected for multiple comparisons using Tukey's multiple comparison test. Exact p-values are shown. All experiments were performed with three independent biological replicates (n=3). Values are displayed as mean ± SD.

Repeating the same experiment in a confocal setting, where only individual Opto-GPX4Deg-expressing cells were activated, resulted in the oxidation of the lipid bilayer by the light-induced ferroptotic cell and subsequent diffusion through the lipid bilayer plane, reaching a new cell that had not been activated to undergo ferroptosis, and promoted its lipid oxidation and cell death **(Fig. 18)**. Accordingly, these experiments demonstrate that lipid peroxidation can propagate between cells over a distance, provided that an oxidizable lipid membrane connects them.

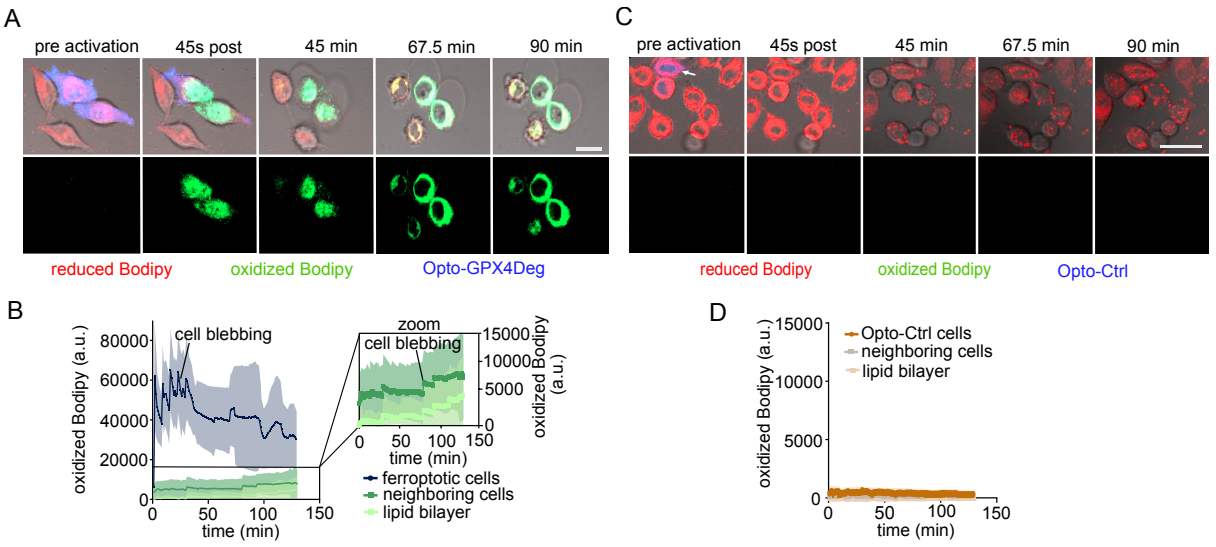

Fig.18: Single-cell ferroptosis induction results in lipid peroxidation spreading and cell death in neighboring cells. (A,C) Time series of C11-Bodipy oxidation and cell death in activated Opto-GPX4Deg **(A)** or Opto-GPX4 **(C)** HeLa cells and bystander neighboring cells grown on a lipid bilayer. Opto-GPX4Deg, blue; oxidized Bodipy, green; reduced Bodipy, red. Scale bar, 30 µm. **(B,D)** Quantification of oxidized C11-Bodipy in single cells and the lipid bilayer over time in the activated Opto-GPX4Deg **(B)** and Opto-Ctrl bulk **(D)**.

These findings suggest the occurrence of iron-dependent lipid oxidation reactions on the extracellular side of plasma membranes during ferroptosis propagation. To test their relevance, we treated the cells with deferoxamine (DFO), a clinically relevant chelator of extracellular iron. Remarkably, DFO treatment completely abrogated ferroptosis propagation, while not affecting the intrinsic sensitivity of individual cells to ferroptosis, whereas the chelation of extracellular and intracellular iron by 2,2-dipyridyl blocked ferroptosis in both bystander cells and cells expressing Opto-GPX4Deg **(Fig. 19)**. As additional control, we also assessed whether potential endosomal uptake and accumulation of DFO interfere with the intrinsic ferroptosis sensitivity of the cells but found that also after prolonged pretreatment (4h and 8h) DFO did not affect the cell death levels of activated Opto-GPX4Deg expressing cells compared to the DMSO control **(Fig. S9)**. Together, these findings suggest that iron-dependent lipid peroxidation reactions are necessary for ferroptosis propagation to occur.

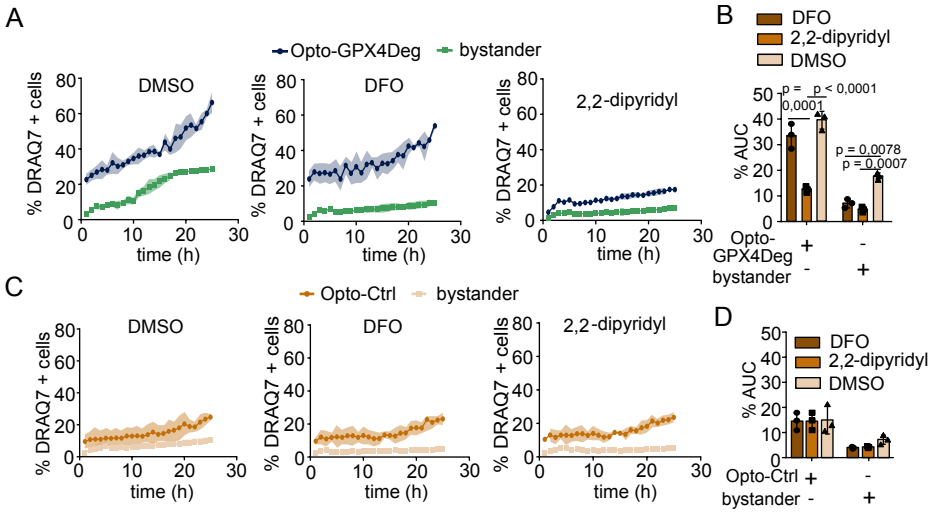

Fig. 19: Lipid peroxidation reactions on the outer leaflet are required for ferroptosis propagation. (A,C) Kinetics of cell death for activated Opto-GPX4Deg **(A)** or Opto-Ctrl **(C)** and bystander HeLa cells treated with DMSO, 100 µM DFO or 100 µM 2,2dipyridyl as indicated. **(B,D)** %AUC for the indicated cell populations. Statistical analysis by one-way ANOVA corrected for multiple comparisons using Tukey's multiple comparison test. Exact p-values are shown. All experiments were performed with three independent biological replicates (n=3). Values are displayed as mean ± SD.

To ultimately demonstrate that lipid peroxidation can spread between apposed plasma membranes, we employed as part of a collaboration with Sara Lotfipour Nasudivar a chemically controlled minimal system. Therefore, we generated Giant Unilamellar Vesicles (GUVs) supplemented with C11-Bodipy. Donor GUVs additionally contained a photosensitizer DMMB and were labeled with DiD, whereas acceptor GUVs were prepared without DMMB and DiD. Via biotinylated lipids in their composition and streptavidin in the external medium donor and acceptor were brought into contact, whereafter donor GUVs photosensitizer was activated by illumination to induce membrane oxidation[137,138]. We then assessed the appearance of oxidized C11-Bodipy over time. Intriguingly, we could quantify increased levels of oxidized C11-Bodipy fluorescence in contacting acceptor GUVs, which we showed to be dependent on iron in the external medium. Importantly, GUV imaging without photoactivation did not result in an increase in the C11-Bodipy fluorescence ratio (not shown). These findings prove that mere proximity is sufficient for the spread of iron-dependent lipid peroxidation between membranes without the need for other cellular components or pathways **(Fig. 20)**.

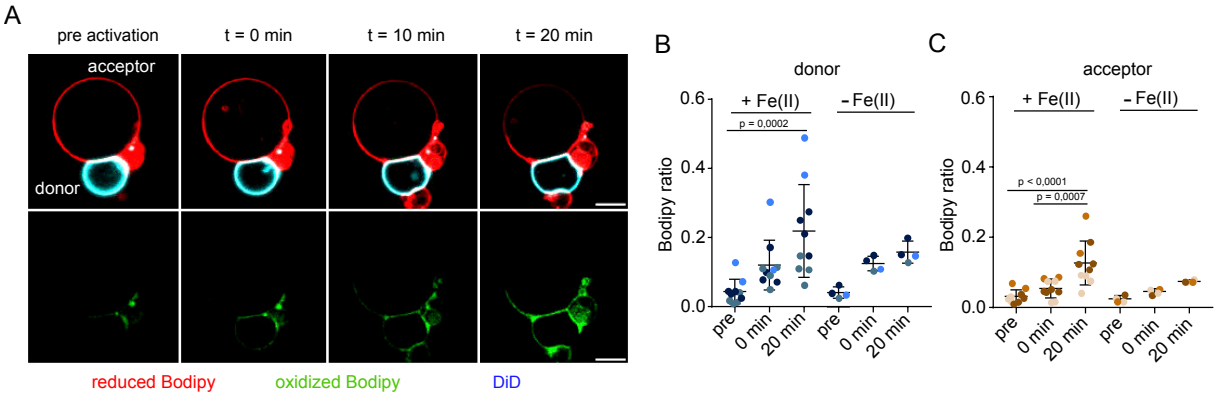

Fig. 20: Lipid peroxides can spread between proximal plasma membranes. (A) Time series of C11-Bodipy oxidation (green) in a “donor” GUV stained with DiD (cyan) and supplemented with a photosensitizer lipid (DMMB). Lipid peroxidation spread to an attached “acceptor” GUV lacking DMMB was observed via oxidized C11-Bodipy staining. Reduced C11-Bodipy is shown in red. **(B,C)** Quantification of the C11-Bodipy ratio between (oxidized/reduced) donor and acceptor GUVs over time in the absence or presence of 10mM iron (II) perchlorate. Statistical analysis by one-way ANOVA corrected for multiple comparisons using Tukey's multiple comparison test. Exact p-values are shown. All experiments were performed with three independent biological replicates (n=3). Values are displayed as mean ± SD.

Overall, these findings uncover a mechanism for ferroptosis propagation across cell populations, which is driven by the physicochemical transfer of iron-dependent lipid peroxidation reactions between neighboring membranes.

Discussion

The goal of this study was to investigate the dynamics of ferroptosis and their consequences on bystander cells at the single cell level. Therefore, we developed a novel optogenetic tool termed Opto-GPX4Deg to control ferroptosis induction by light. By exploiting the currently most potent strategy for inducing ferroptosis, namely GPX4 depletion, Opto-GPX4Deg irreversible disrupts the GPX4-GSH redox defense system. Opto-GPX4Deg is constructed as a fusion protein encoding for GFP, GPX4 and a photoactivatable AsLOV2 domain with a RRRG degron sequence at its C-terminal end that becomes accessible for ubiquitin mediated proteasomal degradation of the fusion protein upon blue light illumination[126,127].

Accordingly, upon illumination cell death could be induced in cells expressing Opto-GPX4Deg and when cotreating the cells with the antioxidant Fer-1 cell death could be abolished in a dose dependent manner. Importantly, we could show on single cell level that seemingly non-transfected bystander cells are indeed below the required expression level of the fusion protein at the activation time point. Hence, those cells don't undergo cell death when activated by light, making Opto-GPX4Deg a suitable tool for studying bystander cell responses with a simple transfection protocol. By WB and fluorescence analysis, we confirmed the light-induced degradation of the GPX4 fusion protein over time. Strikingly, not only the level of the fusion protein but also the endogenous GPX4 levels was reduced, which either indicates the involvement of a coordinated process that regulates GPX4 levels or that the fusion protein might act as a dominant negative interactor via its degron sequence with endogenous GPX4, leading to sufficient disturbance of the GPX4-GSH defense system for causing ferroptosis execution. However, because of the partial enzymatic activity of GPX4 within the fusion protein, it can also be speculated that overexpression of Opto-GPX4Deg might lead in addition to inefficient substrate processing, which could lead to the accumulation of lipid peroxides.

Additionally, we observed that light-induced cell death induction was accompanied by elevated levels of peroxidized lipids, a hallmark of ferroptosis, which we detected by C11-Bodipy staining and lipidomics analysis. Concretely, lipidomics analysis revealed highly increased levels of several oxidized species including phosphatidylehanolamine (PE) and phosphatidylcholine (PC), which are the most abundant lipid species in plasma membranes[139], upon cell death induction with Opto-

GPX4Deg. Currently, phospholipid oxidation is considered as a semi-specific process where different lipid species are differently prone to undergo lipid peroxidation[36]. Accordingly, as reported poly-unsaturated PEs are the primary target for lipid peroxidation and thus were upregulated in our data [139,140]. However, PCs showed the highest upregulation, which agrees with lipidomics data of HeLa treated with ferroptosis inducing compounds[131]. Most likely the aberrant result in comparison to other cell types can be attributed to differences in lipid composition[139]. The upregulation of oxidized lipid species was accompanied by a general loss of fatty acids. Another study reported similar results, where HT-1080 cells were treated with Erastin. Concretely, the study found that several mono-unsaturated fatty acids were depleted, indicating that they might be peroxidized downstream of the initial spark of poly-unsaturated lipid peroxidation[141,142]. Altogether our thorough characterization demonstrated that Opto-GPX4Deg light-triggered cell death is ferroptosis since it can be blocked with the antioxidant Fer-1. Further activated Opto-GPX4Deg expressing cells have increased levels of phospholipid peroxides, a hallmark of ferroptosis, which we measured via C11-Bodipy staining and mass spectrometry and exhibited characteristic morphological features of lytic death.

With the Opto-GPX4Deg tool in hand, we could for the first time investigate in an unbiased fashion, whether ferroptosis spreads through cell populations and dissect the mechanisms underlying the spread of ferroptosis. Concretely, our approach, in contrast to conventional drug administration, allowed us to study the response of bystander cells without changing their ferroptosis sensitivity. Intriguingly, we could recapitulate cell death spread with our optogenetic tool of activated Opto-GPX4 expressing cells to non-transfected bystander cells. In this context, we found that Opto-GPX4 induced cell death propagation was, in contrast to optogenetic apoptosis induction, distance-dependent with a clear preference for cell death induction in adjacent cells, indicating that proximity could be a crucial factor for ferroptosis spread. Further through direct visualization, we could demonstrate that activated Opto-GPX4Deg expressing cells accumulate lipid peroxides and die, followed by the spread of lipid peroxidation and subsequent death to non-transfected bystander cells. Since bystander cell death could be inhibited by Fer-1, the mechanism by which they die could be identified as ferroptosis. Hence, our data confirms previous studies that proposed ferroptosis spread through cell populations[90,91].

Ca^{2+} has been identified as a critical element in ferroptosis execution. As such, cytosolic Ca^{2+} and lipid peroxides accumulate in cells before bursting [41,90]. Concretely, work from our lab suggested that following lipid oxidation, the membrane integrity gets compromised by small pores that cause calcium influx [41]. We could confirm these findings with our optogenetic approach, showing us, that indeed cytosolic calcium increased in Opto-GPX4 activated cells until membrane bursting, whereafter Ca^{2+} gets diluted into the medium. However, other than suggested in a previous study[90], we found no indication that Ca^{2+} plays a role in paracrine calcium fluxes in ferroptosis propagation because we did not measure significant cytosolic Ca^{2+} changes in bystander cells. Nevertheless, we established a role for extracellular Ca^{2+} in ferroptosis propagation in the context of cell-cell contacts, since cadherins, calcium-dependent adhesion molecules, get cleaved in the absence of extracellular calcium via extracellular domain unfolding [143].

Following our hypothesis that proximity is a key parameter in ferroptosis spread, we could validate in HeLa cells that higher cell confluency correlated with higher cell death in non-transfected bystander cells. However, we observed that 100% confluent cells lose their ferroptosis sensitivity, which is in accordance with previous reports showing that very high cell densities lead to increased survival of GPX4 KO cells[27]. The result that increased cell confluency resulted in higher cell death was a surprising finding because so far high cell density was associated with decreased ferroptosis sensitization[82,84,85]. In 2019 Wu and collogues proposed a model, in which E-cadherin, which is an important player in adhesive cell-cell contacts, gets upregulated in response to increased cell densities. This leads to the activation of NF2 and the Hippo signaling pathway rendering cells less susceptible to ferroptosis. Inactivation of this signaling axis by chemical or genetical means was shown to activate the transcriptional co-activator YAP, which in turn promotes the upregulation of pro-ferroptosis regulators such as ACSL4 and TFRC and thus increases ferroptosis susceptibility[82]. In line with this model, we found that ferroptosis propagation did not occur in HT-29 cells, which have high E-cadherin levels, whereas we could observe ferroptosis propagation in cells with no (HeLa) or low (SCLC) E-cadherin expression. Furthermore, exogenous expression of E-cadherin abolished ferroptosis propagation in HeLa cells, whereas N- and P-cadherin were not protective. However, in contradiction to the proposed model, our data suggest that disruption of YAP activity alone is insufficient to explain the protective role of E-cadherin, because both E-cadherin overexpression and α-catenin

depletion[134], as previously reported, resulted in YAP activation, but had different outcome in ferroptosis susceptibility. Additionally, we showed that the expression of E-cadherin ΔCBD mutant, which is defective in its cell-cell contact function but retains intact E-cadherin signaling, was sufficient for the protective function of E-cadherin, despite activated YAP. Altogether, our results indicate that cell-cell contacts sensitize cell populations/tissues for ferroptosis propagation. However, as an additional regulatory layer, the anti-ferroptosis signaling function of E-cadherin might have been developed in the context of high-cell densities for maintaining tissue integrity.

By disrupting the cadherin adhesion complex and hence cell-cell contacts via α-catenin depletion, we ultimately demonstrated that ferroptosis propagation requires cell-cell contacts. Furthermore, reconstitution experiments with WT α-catenin revealed the specificity of α-catenin in this process by fully restoring ferroptosis propagation in bystander α-catenin KO HeLa cells. In contrast to that, reconstitution of different α-catenin mutants that lack binding a site to other components of the cadherin adhesion complex in α-catenin KO HeLa cells, failed to rescue ferroptosis propagation, because of their inability to form adhesive cell-cell contacts. In addition to genetic manipulation of cell-cell contacts via α-catenin depletion, we also demonstrated that increasing cell-cell contacts by chemical means fully restores ferroptosis propagation in α-catenin-depleted HeLa cells and further enhances it in control cells by blebbistatin administration. Further, we found that the removal of extracellular iron via DFO administration was sufficient to completely abolish ferroptosis propagation without changing the ferroptosis sensitivities of activated Opto-GPX4Deg expressing cells. These findings further underline that the transfer of iron-dependent lipid peroxidation reactions to neighboring cells requires close plasma membrane proximity between cells that are facilitated by cell-cell contacts and that iron-mediated lipid peroxidation reactions on the extracellular leaflet of plasma membranes are crucial for ferroptosis propagation.

To further establish that iron-dependent lipid peroxidation reactions are the key drivers for ferroptosis propagation, we bridged the distance between cells using an oxidizable artificial lipid bilayer that connects cellular membranes and is capable of spreading lipid peroxidation. Intriguingly, we could demonstrate that facilitated by this bilayer lipid peroxidation spread and subsequent cell death is indeed significantly enhanced between cells. However, to unambiguously prove that the mechanism based

on ferroptosis propagation is of a physicochemical nature that is based on lipid peroxidation reactions, we wanted to demonstrate that lipid peroxides can propagate between contacting lipid membranes. For this purpose, we directly visualized, using minimal reconstituted systems that are based on purely synthetic membrane models, that lipid peroxidation can spread between apposed membranes. This minimalistic approach allowed us to eliminate all additional factors of previously used, more complex cellular systems and therefore enabled us to elucidate the physicochemical mechanism that drives ferroptosis propagation via lipid peroxidation spread between contacting plasma membranes.

In recent years ferroptosis spread was associated with several diseases or their progression through necrotic tissue formation including intestinal epithelium [144], heart tissue [145–147], excitotoxicity in the brain [148] and renal tubules[89], which underlines the pathophysiological importance of ferroptosis propagation. Since we discovered in this work the underlying mechanism of ferroptosis propagation, it is now possible to leverage this knowledge to develop strategies to combat human diseases either by blocking or enhancing ferroptosis propagation. Accordingly, a recent study showed that ferroptosis propagation can be exploited as cancer treatment, where even deep-seated tumor cells undergo ferroptosis, while exhibiting a sustained high immunogenicity promoting an anti-tumor immune response[149]. On the other hand, our results demonstrated that ferroptosis propagation can be specifically blocked by genetic and chemical means. Especially the treatment with the clinically approved drug DFO for iron overload[150] seems promising since we showed that this extracellular iron chelator specifically abolishes ferroptosis propagation. This is of particular interest because DFO treatment has been shown to mitigate ischemic heart and brain injury in rodents[151–155]. Further, DFO demonstrated in clinical studies to reduce oxidative stress without reducing heart infarct size[156], to protect the myocardium against reperfusion injury during coronary artery bypass[157] and to delay the progression of Alzheimer's disease-associated dementia [158], which further underscores the involvement of ferroptosis propagation in numerous diseases. Also, in accord with our findings, inducible α-catenins double knockout mice exhibit an improved cardiac function after myocardial infarction compared to WT mice[159]. Hence, the identification of the molecular mechanism that drives ferroptosis propagation has the potential to guide novel therapeutic strategies for ferroptosis-associated pathologies.

Finally, our newly developed optogenetic tool presented here enables for the first time the investigation of the physiological significance of ferroptosis propagation in diverse *in vivo* settings. These studies will improve our understanding of how ferroptosis modulators can be exploited in future treatments.

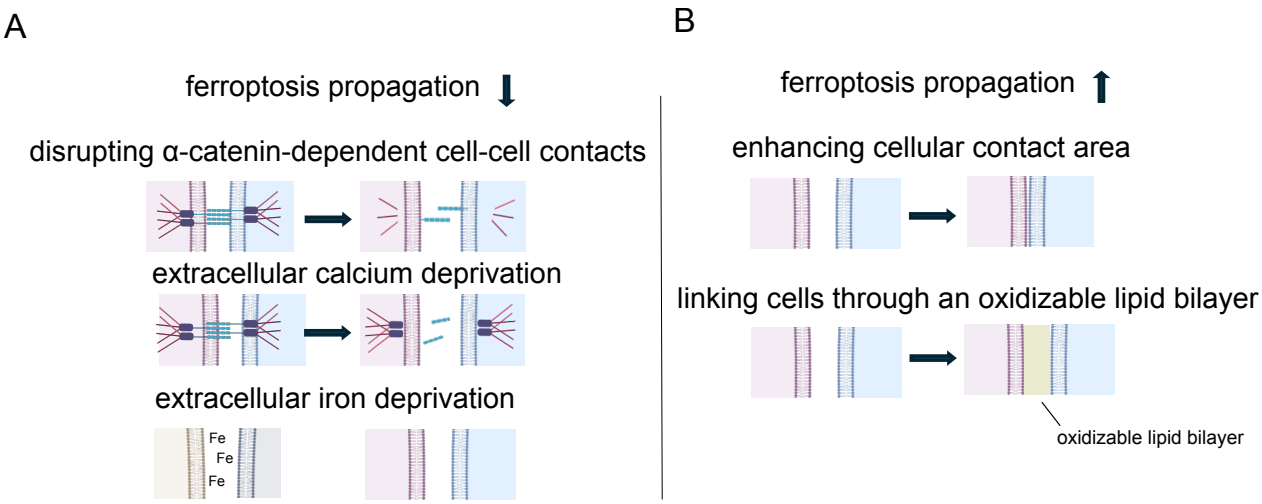

Fig. 1: Factors for modulating ferroptosis propagation. (A) Ferroptosis propagation is inhibited when α-catenin dependent cell-cell contacts are abrogated either by α-catenin KD or KO or by extracellular calcium deprivation. Extracellular iron is required for lipid peroxidation reaction on the outer leaflet of the plasma membrane enabling ferroptosis propagation. **(B)** Ferroptosis propagation can be enhanced by increasing cellular contact areas using blebbistatin or when cells are linked through an oxidizable lipid bilayer.

Conclusions

The following conclusions can be derived from this thesis:

- Via our novel optogenetic tool for light-controlled induction of ferroptosis, we demonstrate that lipid peroxidation and ferroptotic cell death can propagate to neighboring cells in close contact.
- Ferroptosis propagation occurs through the transfer of iron-dependent lipid peroxidation reactions between closely apposed plasma membranes at cell-cell contacts.
- Ferroptosis propagation can be abolished genetically or with extracellular iron chelators, opening up new therapeutical opportunities for specifically targeting ferroptosis spread.

Materials and methods

Reagents

Product	Provider	Catalog no.
Erastin-1	Biomol	Cay17754-5
RSL3	Biomol	Cay19288-5
Nec-2	Biomol	Cay20924-5
Fer-1	Biomol	Cay17729-5
zVAD	APEXBIO	A1902
C11-BODIPY 581/591	Thermo Fisher Scientific	D3861
Flou-4-AM	Thermo Fisher Scientific	F14201
FINO2	MedChemExpress	HY-129457
Draq7	Invitrogen	D15106
Blebbistatin	Cayman Chemicals	13013
DFO	Sigma-Aldrich	D9533
2,2-Bipyridyl	Sigma-Aldrich	D216305
DiD	Thermo Fisher Scientific	D7757
Hoechst33342	Thermo Fisher Scientific	H3570
Ponceau S	Carl Roth	5938.2
PBS	Sigma	D8537
Optimem	Thermofisher	31985070
Paraformaldehyde	VWR	PIER28908
Nitrocellulose membrane	Sigma	GE10600006
FBS	Thermofisher	10270106
Q5 High-Fidelity DNA Polymerase	NEB	M0491 L
PEI	Polyscience	24885
penicillin–streptomycin	Thermo Fisher Scientific	15140122
Coomassie brilliant blue G-250 dye	Bio-Rad	5000001

Table 1: List of reagents used in this study.

Antibodies

Antibody	reactivity	Dilution	Provider	Catalog no.
Anti-ß-tubulin G8	mouse	1 /1000	Santa Cruz	sc-55529
Anti-GPX4 [EPNCIR144]	rabbit	1 /1000	Abcam	AB125066
Anti-α-catenin	rabbit	1 /1000	Sigma-Aldrich	C2081
Anti-α-E-Catenin (D9R5E)	rabbit	1 /1000	Cell Signaling	36611S
Anti-FSP1	rabbit	1 /1000	PTG Lab	20886-1-AP
Anti-YAP (D8H1X)	rabbit	1 /1000	Cell Signaling	14074
Anti-phospho-YAP (Ser127) (D9W2I)	rabbit	1 /1000	Cell Signaling	13008
Anti-GAPDH	mouse	1 /200	Santa Cruz	sc-47724
Anti-VDAC2	rabbit	1 /1000	PTG Lab	11663-1-AP
Anti-ß-Actin (C4)	mouse	1 /1000	Santa Cruz	sc-47778
Anti-mCherry (E5D8F)	rabbit	1 /1000	Cell Signaling	43590

Table 2: Primary antibody used in this study.

Antibody	reactivity	Dilution	Provider	Catalog no.
IRDye 800CW	rabbit	1 / 5000	LI-COR	926-32213
IRDye 680RD	mouse	1/ 10000	LI-COR	926-68070
Anti-mouse (H+L) Alexa Flour 488	goat	1 /1000	Thermo Fisher Scientific	A32723

Table 3: Secondary antibody used in this study.

Buffer

Name	Composition
6x Loading buffer	4% SDS, 10% ß-mercaptoethanol, 20% glycerol, 0.004% bromophenol blue, 0.125 M Tris HCl pH 6.8
PBS buffer	2.7 mM KCl, 1.5 mM KH2PO4, 8 mM Na2HPO4, and 137 mM NaCl, pH 7.2
RIPA	50 mM Tris, pH 7.5, 150 mM NaCl, 0.1% SDS, 0.5% sodium deoxycholate and 1% Triton X-100, supplemented with 1x protease inhibitor cocktail
TBST	5 mM sodium acetate, 1 mM EDTA, 20 mM Tris HCl, 135 mM NaCl, 1 M HCl pH 7.6, 0.1% Tween 20
HEPES buffer	20mM HEPES, 140mM NaCl, pH 7.0
DMMB	5 mol% - DMMB was dissolved in ethanol (5mM), Iron (II) percholarte in deionized water (10mM)
Antibody Dilution Buffer	diluted in 1X PBS / 1% BSA / 0.3% Triton™ X-100 buffer
Blocking buffer	5 % milk in PBS-T (0.1 % Tween)
CaCl2	dissolved in distilled water 3 mM
Blocking buffer (IF)	1X PBS / BSA / 0.3% Triton™ X-100

Table 4: Composition of buffers used in this study.

Plasmids

Cloning strategy

The following plasmids were cloned via restriction digest cloning as follows:

Plasmids	Cloning steps	Backbone	cDNA	Restriction sites
Opto-GPX4Deg	1	pcDNA™3.1 (+) (Invitrogen)	pMTG02-Amp-FRT plasmid (Addgene #128271) to amplify LOVpepdegron	ApaI and XhoI
	2	pcDNA3.1-LOVpepdegron	GPX4 (Addgene #38797)	EcoRI and NotI
	3	pcDNA3.1-GPX4-LOVpepdegron	pGFP-Cytochrome C (Addgene #41181) to amplify EGFP	HindIII/EcoRI
Opto-Ctrl	1-3 Opto-GPX4Deg		pMTG02-Amp-FRT plasmid (Addgene #128271) to amplify LOVpep (without RRRG sequence); rest as 2-3 Opto-GPX4Deg	
Opto-GPX4Deg (BFP2)	1	Opto-GPX4Deg	mTagBFP2-TOMM20-N-10 (Addgene #55328) to amplify mTagBFP2	HindIII/EcoRI
Opto-Ctrl (BFP2)	1	Opto-Ctrl	mTagBFP2-TOMM20-N-10 (Addgene #55328) to amplify mTagBFP2	HindIII/EcoRI
Opto-Casp9	1	GPF-Cry2 (Garcia lab)	pET23b-Casp9-His (Addgene #11829)	NheI/KpnI
pCS2+P-cadherinRFP	1	pCS2+EcadRFP	pcDNA3 P-cad (Addgene #47502) to ampflify P-cadherin	HindIII/XbaI
pCS2+N-cadherinRFP	1	pCS2+EcadRFP	pCCL-c-MNDU3c-PGK-EGFP (Addgene #38153) to amplify N-cadherin	HindIII/XbaI
pmCherry α-catenin ΔF-actin	1	pmCherry α-catenin WT (#178646)	amplifying WT α-catenin 1-864	SacI/MfeI
pmCherry α-catenin Δß-catenin	1	pmCherry α-catenin WT (#178646)	α-catenin 259-906	SacI/MfeI

Table 5: Used cloning strategy for the indicated plasmids.

Plasmids	Provider
GPF-Cry2	Garcia lab
Cry2(1-531)-mCh-BAXS184E (#117238)	Addgene
pcDNA-NLS-PhoCl-mCherry (#87691)	Addgene
Tom20-CIB-GFP (#117242)	Addgene
pcDNA3-mRFP (#13032)	Addgene
pCS2+EcadRFP	Niessen lab
pCS2+Ecad ΔCBD-RFP	Niessen lab
pmCherry (#165828)	Addgene
pmCherry α-catenin WT (#178646)	Addgene
pmCherry α-catenin DVBS (#178649)	Addgene

Table 6: Plasmids used in this study.

For the cloning the following protocol was utilized:

- Respective cDNAs were amplified by PCR with the following settings:

Reagents	Volume
Nuclease free water	To 50µl
5x Q5 reaction buffer	10µl
5x Q5 High GC Enhancer	10µl
20µM Forwardprimer	1,25µl
20µM Reverseprimer	1,25µl
1,5µl dNTPs(10mM)	1,5µl
Template DNA	100ng
Q5 High-Fidelity DNA Polymerase	1µl

Table 7: PCR reaction composition.

Step	Temperatur	Time
Initial denaturation	98°C	30s
	98°C	30s
35 cycles	50-72°C	30s
	72°C	30s - 2 min
Finalextension	72°C	2min

Table 8: PCR settings. Annealing temperatures were adapted to the respective primers.

- PCR products were separated with an agarose gel electrophoresis. Specific bands were cut out and purified with a PCR Clean-up kit (Catalog no. 740609.50).
- Backbone and purified PCR products were digested according to Table 5 for 30 min at 37°C.
- Digested backbone and PCR products were ligated using a T4 ligase (New England Biolands Catalog no. M0202) with a 1:3 ratio over night at 16°C.

- DH5α bacteria were transformed with ligation products for 45s at 42°C and subsequently incubated at 37°C on agar plates with respective antibiotics.
- Single colonies were picked and cultivated over night at 37°C in antibiotics containing LB medium. Plasmids were purified with Omega Bio-tek kit (Catalog no. M6399-00) and sent to sequencing for verification.

Cell culture

All cell lines were cultured at 37°C in a humidified atmosphere containing 5% CO_2. DMEM and RPMI-1640 were supplemented with 10% fetal bovine serum (FBS) and 1% penicillin–streptomycin (P/S).

Cell lines	Provider	Medium	Medium Provider	Catalog no.
HeLa	A. Villunger, Med. Univ. Innsbruck	DMEM	Sigma-Aldrich	D6046
HT-29	F. Essmann, Univ. Tübingen	DMEM	Sigma-Aldrich	D6046
HEK293	F. Essmann, Univ. Tübingen	DMEM	Sigma-Aldrich	D6046
Pfa1	M. Conrad, Helmholtz Center Munich	RPMI-1640	Thermo Fisher Scientific	11875093
SCLC	S. von Karstedt, Univ. Cologne	RPMI-1640	Thermo Fisher Scientific	11875093
GPX4 KO SCLC	S. von Karstedt, Univ. Cologne	RPMI-1640	Thermo Fisher Scientific	11875093

Table 9: List of used cell lines and respective media.

Cell transfection

Cell transfection was performed according to Table 10 with a PEI concentration of 1 mg/mL in a 3:1 ratio. The DNA/PEI mixture was resuspended and incubated for 20 min at room temperature. Then the transfection mix was added dropwise to the wells and incubated at 37°C for 16h wrapped in aluminum foil.

Culture vessel	Surf. area/well	Vol. plating medium	Vol. Optimem	DNA	PEI
8-well chamber	1 cm^2	200 µl	2 x 25 µl	0,24 µg	1,2 µl
96-well	0.3 cm^2	100 µl	2 x 25 µl	0.2 µg	0.6 µl
24-well	2 cm^2	500 µl	2 x 50 µl	0.4 µg	1.2 µl
6-well	10 cm^2	2 ml	2 x 250 µl	1,5 µg	4,5 µl

Table 10: List of transfection conditions.

Silencing experiments

For every 6-well-plate-well 20 pmol of siRNA targeting α-catenin (GGAGCCAGCUAGAUAUUAA, SiTools Biotech) or control/non-targeting siRNA (D-001810-0120, SiTools Biotech) was premixed in 100 µM Optimem and subsequently mixed in a 1:1 ratio with PEI diluted in 100 µl Optimem. Then the mixture was incubated at room temperature for 25 min, whereafter the mixture was dropwise added to the cells. 48h prior to optogenetic tool transfection siRNA transfection was performed or for 72h before harvesting cells for WB. Endogenous protein levels were assessed by WB.

CRISPR/Cas9 cell line generation

HeLa α-Catenin KO cells were generated via CRISPR/Cas9 technology. Therefore, oligonucleotides containing gRNA sequences (Table 11) were cloned, using the restriction site BbsI, into the pU6-(BbsI)sgRNA CAG-Cas9-venus-bpA construct (Addgene #86986).

Name	gRNA sequence
hCTNNA1_sgRNA#1FWD	CACCGTTTATCGATGCTTCCCGCC
hCTNNA1_sgRNA#1REV	AAACGGCGGGAAGCATCGATAAAC
hCTNNA1_sgRNA#2FWD	CACCGTCACGTAGTCACCTCAGAGA
hCTNNA1_sgRNA#2REV	AAACTCTCTGAGGTGACTACGTGAC

Table 11: gRNA sequences used in this study.

7 x 10^5 HeLa WT cells were seeded in a six-well plate and transfected with 1,5 µg CRISPR construct and 6 µl PEI. After 16h incubation single CRISPR expressing cells (GFP positive) were sorted into 96 well plates and cultured for validation. KO clones were validated by WB.

Confocal live cell imaging

5,000 cells were plated into removable 8-well chambers (Cat. No: 80841 ibidi) with a glass cover slip suitable for confocal microscopy (VWR Cat. No: 631-0146). All confocal experiments were conducted using a Confocal Laser Scanning Microscope LSM 980 with Airyscan 2 and multiplex, GaAsP (4x), PMT (2x), T-PMT, and external BiG.2 Type B 980 detector (Carl Zeiss Microscopy). For image acquisition, a 40x/1.2 W C-Apochromat objective, diode lasers with the wavelengths of 405 nm, 455 nm, 488

nm, and 561 nm (all 30 mW), GaAsP and transmitted light (T-PMT) detectors, and main LSM beamsplitters (MBS 405 and MBS 488/561/633) were used. All experiments were conducted at 37°C with 5% CO2 using an integrated incubation module (Carl Zeiss Microscopy). The microscope was equipped with the ZEN Image analysis software (Carl Zeiss Microscopy). The following settings were used for confocal image acquisition:

- Field of view was set to 512x512 pixels.
- Acquisition speed was set to maximum using line-wise bidirectional scanning and 4x averaging in the Repeat per Line Mode.
- For imaging fluorescent signals (GFP, mCherry or BFP2) the respective settings were used:
    - GFP: 6.5 µW for the 488 nm laser.
    - mCherry: 79 µW for the 561 nm laser.
    - BFP2: 13.8 µW for the 445 nm laser.
- Brightfield images were captured utilizing the 561 nm laser at 79 µW and a transmitted light (T-PMT) detector.

Optogenetic activation in confocal microscopy

Confocal optogenetic experiments were conducted according to Fig. 1. Concretely, ROIs were drawn using the ROI bleaching function that cover the entire cell area of optogenetic tool expressing cells and non-transfected bystander cells. As a control for autoactivation of optogenetic tools, not all cells expressing the optogenetics tools within the field of view were activated. To optogenetically activate cells, the 405 nm laser was used at 456 µW intensity, by setting up a time series acquiring one pre-activation image, before activating selected ROIs with 100 iterations every 7 images or with the indicated activation rounds of the respective experiment. For C11-Bodipy quantification three rounds of activation were performed, after which confocal images were acquired 5- and 65 min post activation. Images for the Ca^{2+} experiments were acquired every 45 s upon four optogenetic activation rounds.

As a quality control, only experiments were considered for analysis if all of the following controls worked:

- Illumination of bystander cells to rule out phototoxicity of the illumination conditions.
- Non-illumination of transfected cells to check for potential self-activation or construct toxicity.
- Non-illumination of bystander cells to check for phototoxicity of the live cell imaging time series acquisition (= background cell death).

If one of the controls died (used cell blebbing as a proxy for cell death induction) during the experiments, the experiment was excluded from further analysis.

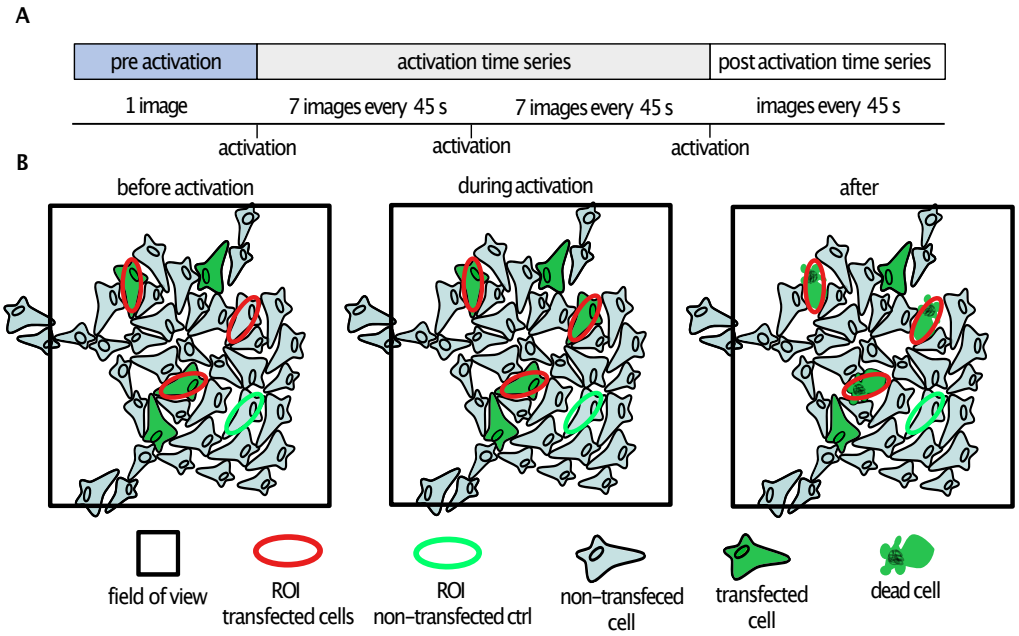

Fig. 1: Experimental design of confocal optogenetic experiments. Adapted from: [109]

High-throughput optogenetic experiments

For optogenetic tool activation in the high-throughput approach, an optoPlate-96 was used [128]. To program the optoPlate-96, we used the optoConfig-96 software [129]. To activate our optogenetic tools, we utilized the 465 nm LEDs with the following settings:

LED intensity (%)	mW/cm^2
100	5
80	4
60	3
40	2
20	1
0	0

Table 12: Used LED intensities.

Cell death kinetics were acquired using a S3 IncuCyte (Sartorius). At least three images per well were acquired with a 400 ms exposure for both channels (red and green). For the high-throughput assessment of C11-Bodipy kinetics an ImageXpress Micro 4 (MD) was used. The microsope was equipped with a 10x Plan Flour 0.3 NA objective and an Andor Cycla 5.5 (CMOS) camera. The following channels were used with autocorrection:

Channel	exposure(ms)
TI-20	2
DAPI	50
FITC	200
TRITC	100

Table 13: Used channels settings.

Lipids

Product	Provider	Catalog no.
egg-PC	Avanti Polar Lipids	131601
DOTAP	Avanti Polar Lipids	890890
PAPC	Avanti Polar Lipids	850459
biotin-PE	Avanti Polar Lipids	860562
DMMB	Sigma-Aldrich	341088-1G

Table 14: Used lipids or lipids staining in this study.

Lipid bilayer experiments

To generate bilayers, small unilamellar vesicles were prepared as follows:

- Egg-PC and DOTAP were mixed in a 70:30 ratio in chloroform, whereafter chloroform was evaporated for 4- to 14h and exposed to an argon flux for a long-term storage as dry film at -20°C.
- Dry films were hydrated with PBS to a final concentration of 10 mg/ml.
- Aliquots were diluted in HEPES buffer (140 µl per 10 µl liposome solution and sonicated in an ultrasonic bath for 20 min.

Confocal lipid bilayer experiments

- 8-well ibidi chambers and plasma cleaned glass slides (length 75 mm, thickness 1.5) were sterilized by 70% ethanol.
- 150 µl liposome solution was added per well and filled up with HEPES buffer to a total volume of 500 µl.
- $CaCl_2$ to a total concentration of 3 mM was added and incubated for 10 min at 37°C.
- Floating vesicles were washed out by removing and adding 150 µl HEPES buffer for at least 10 times.
- 400 µl of HEPES buffer was removed and replaced with 300 µl cell suspension containing $2.5x10^4$ cells.
- Cells were transfected via reverse transfection.
- Upon 16h after transfection 1 µM C11-Bodipy was added before optogenetic activation.

Incucyte lipid bilayer experiments

- 75 µl liposome solution per 96 well plate was added and filled with buffer to a final volume of 200 µl.
- $CaCl_2$ to a total concentration of 3 mM was added and incubated for 10 min at 37°C.
- Floating vesicles were washed out by removing and adding 100 µl HEPES buffer for at least 10 times.
- 150 µl HEPES buffer was removed and refilled with 100 µl cell suspension containing $1.5x10^4$ cells.

- Cells were transfected via reverse transfection.
- Upon 16h after transfection 1 µM C11-Bodipy or 1:500 DRAQ7 was added before optogenetic activation.

Preparation and oxidation of giant unilamellar vesicles

- Lipid composition was egg-PC, PAPC and biotin-PE in a 90:5:5 ratio.
- Chloroform dissolved lipid mixture (2.5 mg/mL) was spread on platinum wires of the electroformation chamber where it dried. Afterwards it was immersed in 300 µL of 300 mM sucrose.
- Electroformation was executed using an alternating power generator at 10 Hz, 1.4 V for 2 h, followed by 45 min at 2 Hz, 1.4 V.
- Oxidation was initiated by addition of DMMB 5 mol%, tracked with C11-Bodipy 2 mol%. For distinguishing oxidation from donor GUVs to acceptor GUVs with the same lipid mixture supplemented with C11-Bodipy 2 mol%, but without the photosensitizer, donor GUVs were additionally stained with DiD.
- PBS buffer was mixed with 0.75 µmol streptavidin for anchoring to biotin-PE and 80 µmol iron (II) perchlorate for a continued lipid radical production.
- 50 µl of acceptor and donor GUV suspension was added to get a final volume of 250 µl in an 8-well-ibidi chamber.

Samples were imaged by confocal fluorescence microscopy using an infinity line scanning microscope (Abberior Instruments) equipped with a UPlanX APO 60x Oil/1.42 NA objective. Donor GUVs were activated by a 640 nm laser at 20% laser power in a time interval of 1 min (30 x every 2 sec). Oxidation propagation was acquired with the following settings:

laser (nm)	intensity(%)
488	2
561	1
640	0,5

Table 15: Used laser settings for the GUV oxidation experiments.

Additional negative controls in presence or absence of iron, but without photosensitizer activation were performed.

Image analysis

Image analysis of confocal experiments was performed in Fiji, where activation- and post activation time series were concentrated into one time series. Brightness and contrast of all channels were adjusted. Afterwards the time till blebbing of transfected cells, illuminated bystander cells, non-illuminated transfected cells and non-illuminated bystander cells was manually assessed.

A custom-made software was used for assessing the percentage of transfected-, bystander- or oxidized C11-Bodipy positive cells of the high-throughput optogenetics experiments [160]. Concretely, the number of transfected-, bystander- and cell death-marker positive cells was assessed and normalized by the total number of transfected/bystander cells divided by the number of double positive cells. The position and fluorescence levels of single cells were obtained by image segmentation of our custom-made software. Distances between cells were acquired through vector calculations that were based on coordinates of single cells.

Lipid peroxidation experiments

5000 cells were seeded the day before transfection. 16h post transfection cells were stained with 1 µM C11-Bodipy for one hour and treated with 10 µM zVAD. Subsequently, cells were activated as described in the optogenetic activation in confocal microscopy section. C11-Bodipy fluorescence levels of individual cells were assessed 5- and 65-min post-activation and corrected for cell size and local background subtraction was performed. The oxidation ratio was calculated as follows:

$$oxidation\ ratio = \frac{red + green\ flouresence}{green\ flouresence}$$

red = reduced C11-Bodipy fraction

green = oxidized C11-Bodipy fraction

Reduced and oxidized C11-Bodipy fractions were determined on the fluorescence intensity per pixel from the red and green channel of the fluorescence images using Fiji or our custom-made software.

Ca^{2+} wave measurements

Ca^{2+} fluxes were acquired as described in the optogenetic activation in confocal microscopy section. Activation- and post activation time series were imported to Fiji and concentrated into one time series. Subsequently, ROIs of cells undergoing optogenetically triggered ferroptosis and their neighboring cells in the first to the third rows were manually drawn. Afterwards, the green fluorescence signal was measured at the ROIs for all time points using Fijis multi measure function.

Immunofluorescence staining

$3x10^4$ cells were seeded on an ethanol sterilized 12mm cover slip. On the following day the cells were transfected with a siRNA or expression plasmid, whereafter they were incubated for 48h before fixation in 4% formaldehyde for 15 min at room temperature. Then the samples were washed three times in PBS before they were blocked for 60 min in blocking buffer. Afterwards the blocking buffer was removed, and the samples were incubated at 4°C over night in Antibody Dilution Buffer supplemented with Anti-YAP antibody. On the next day the specimens were rinsed three times with PBS and then incubated in Antibody Dilution Buffer supplemented with secondary antibody for 1h protected from light. Then the samples were washed three times in PBS and counterstained with Hoechst33342 for 5 min, where after the samples were again washed 3 times with PBS and subsequently mounted for imaging. For buffer or antibody details see Table 4.

Immunoblotting

Cells were lysed in RIPA buffer and protein concentrations were determined by Bradford assay. 40 µg protein per sample was loaded and separated for 1.5h with 125 V via 12 % SDS-PAGE, followed by the transfer onto a nitrocellulose membrane using the Turboblot (BioRad) or a wet transfer system (BioRad) according to the manufactures instructions. Membranes were blocked with blocking buffer for 1 hour at room temperature and incubated over night with primary antibodies. Membranes were washed five times for 5 min in PBS-T and incubated with the secondary antibody at room temperature, protected from light, for one hour. Afterwards membranes were washed with PBS-T and the fluorescence signal was captured by an Odyssey DLx (LI-

COR), whereafter the Western Blots were quantified using the Image Studio Lite Software.

Quantification of oxidized glycerophospholipids

Oxidized phosphatidylcholine (PC) and phosphatidylethanolamine (PE) species were quantified by Liquid Chromatography coupled to Electrospray Ionization Tandem Mass Spectrometry (LC-ESI-MS/MS) as follows[62]:

- 1 – 2 million cells were resuspended in 300 µl of an ice-cold solution of 100 µM PBS supplemented with diethylenetriaminepentaacetic acid (DTPA).
- Per 100 µl of the cell suspension, 2.4 ml of an ice-cold solution (1.5 mg/ml triphenylphosphine and 0.005 % butylated hydroxytoluene in methanol) was added and incubated for 20 min on a shaker at room temperature.
- Then, 1 ml of the 100 µM DTPA in PBS solution, 1.25 ml of chloroform and internal standards (10 pmol 1,2-dimyristoyl-sn-glycero-3-phosphocholine (DMPC) and 10 pmol 1,2-dimyristoyl-sn-glycero-3-phosphoethanolamine (DMPE)) were added to the samples.
- Samples were vortexed for 1 min and subsequently incubated at -20 °C for 15 min.
- 1.25 ml of chloroform and 1.25 ml of water were added and vigorously vortexed for 30 s, after which the samples were centrifuged at 4000 g for 5 min at 4°C to separate layers.
- The organic phase was moved to a fresh tube, where it was dried under a stream of nitrogen. Afterwards, the remaining's were resolved in 150 µl of methanol and moved to autoinjector vials.
- LC-MS/MS analysis was performed as previously demonstrated [161,162].
- MultiQuant 3.0.2 software was used to integrate the LC chromatogram peaks of oxidized PC and PE species and internal standards.
- Quantification of oxidized PC and PE species was achieved by normalizing their peak areas to those of the internal standards, whereafter the normalized peak areas were normalized to the protein content of the cell suspension.
- Fold changed were calculated as follows:

$$Fold\ change = \frac{\frac{Area\ ratio}{\mu g\ protein}\ upon\ illumination}{\frac{Area\ ratio}{\mu g\ protein}\ of\ non-illuminated\ Ctrl}$$

Quantification of fatty acids

- 1 – 2 million cells were resuspended in 300 µl of an ice-cold solution of 100 µM PBS supplemented with diethylenetriaminepentaacetic acid (DTPA).
- Per 50 µl cell suspension 50 µl of water, 500 µl of methanol, 250 µl of chloroform, and internal standard (1 µg palmitic-d31 acid) were added.
- Then the suspension was sonicated for 5 min and subsequently lipids were extracted on a shaker at 48 °C for 1 h.
- Via alkaline hydrolysis glycerolipids were degraded by adding 75 µl of 1 M potassium hydroxide in methanol.
- The suspension was sonicated for 5 min and then incubated at 37 °C for 1.5 h, after which the extract was neutralized with 6 µl of glacial acetic acid.
- To the extracts 2 ml of chloroform and 4 ml of water were added and then the extracts were vigorously vortexed for 30 s. Afterwards the extracts were centrifuged at 4000 g for 5 min at 4°C to separate layers.
- The organic phase was moved to a fresh tube and the upper phase was extracted by additionally adding 2 ml of chloroform.
- The combined organic phases were dried under a stream of nitrogen and residues were resolved in 300 µl of acetonitrile/water 2:1 (v/v) and sonicated for 5 min.
- Residues were centrifuged for 2 min at 4°C and 12000 g, after which 40 µl of the clear supernatants were moved to autoinjector vials.
- LC-ESI-MS/MS analysis was performed as performed previously [163].
- 10 µl of sample were loaded onto a Core-Shell Kinetex Biphenyl column (100 mm × 3.0 mm ID, 2.6 µm particle size, 100 Å pore size, Phenomenex), and fatty acids were detected using a QTRAP 6500 triple quadrupole/linear ion trap mass spectrometer (SCIEX).
- Fatty acids were eluted with the following gradient:

initial, 55 % B
4 min, 95 % B
7 min, 95 % B
7.1 min, 55 % B
10 min, 55 % B

Table 16: Elution gradient.

- Pseudo Multiple Reaction Monitoring (MRM) transitions[163] was used to monitor fatty acids in the negative ion mode.
- The following instrument settings were used:

nebulizer gas	60 psi
turbogas	90 psi
curtain gas	40 psi
collision gas	medium

Table 17: Gas settings.

Furthermore, the interface heater was on, the Turbo V ESI source temperature was 650 °C, and the ionspray voltage was -4 kV.

- MultiQuant 3.0.2 software was used to integrate the LC chromatogram peaks of the endogenous fatty acids and the internal standard palmitic-d31 acid were integrated using the MultiQuant 3.0.2 software (SCIEX).
- Quantification of endogenous fatty acids was achieved by normalizing their peak areas to those of the internal standards, where after the normalized peak areas were normalized to the protein content of the cell suspension.
- Fold changed were calculated as follows:

$$Fold\ change = \frac{\frac{Area\ ratio}{\mu g\ protein}\ upon\ illumination}{\frac{Area\ ratio}{\mu g\ protein}\ of\ non-illuminated\ Ctrl}$$

MEF co-culture with ferroptotic supernants

Ferroptotic cell culture supernatants were derived from two independent genetic systems:

- Tamoxifen inducible Pfa1[27] GPX4 KO cells treated with 1μM 4-hydroxytamoxifen or DMSO for 72h
- SCLC GPX4 knockout or control cells [161] were culture under Fer-1 withdrawal for 16h.

Supernatants were collected, centrifuged for 5 min at 1200 rpm and transferred to WT MEFs treated or not treated with 0.1 μM RSL3 or 1 μM Erastin +/-1 μM ferrostatin.

Statistical analysis

Depending on the number of compared groups and factors considered in each experiment, different statistical tests were performed to assess statistical differences. Non-parametric t-tests were used to compare two groups or conditions. When multiple t-tests were conducted within a single graph, corrections for multiple comparisons were applied by utilizing a multiple t-test. For analyzing more than two groups or conditions, a one-way ANOVA was used if a single factor was compared, and a three-way ANOVA was used if three factors were compared. Tukey's multiple comparison test was performed to correct for multiple comparisons. Hopkins statistics was performed to assess the clustering tendency of data sets [164].

Supplementary data

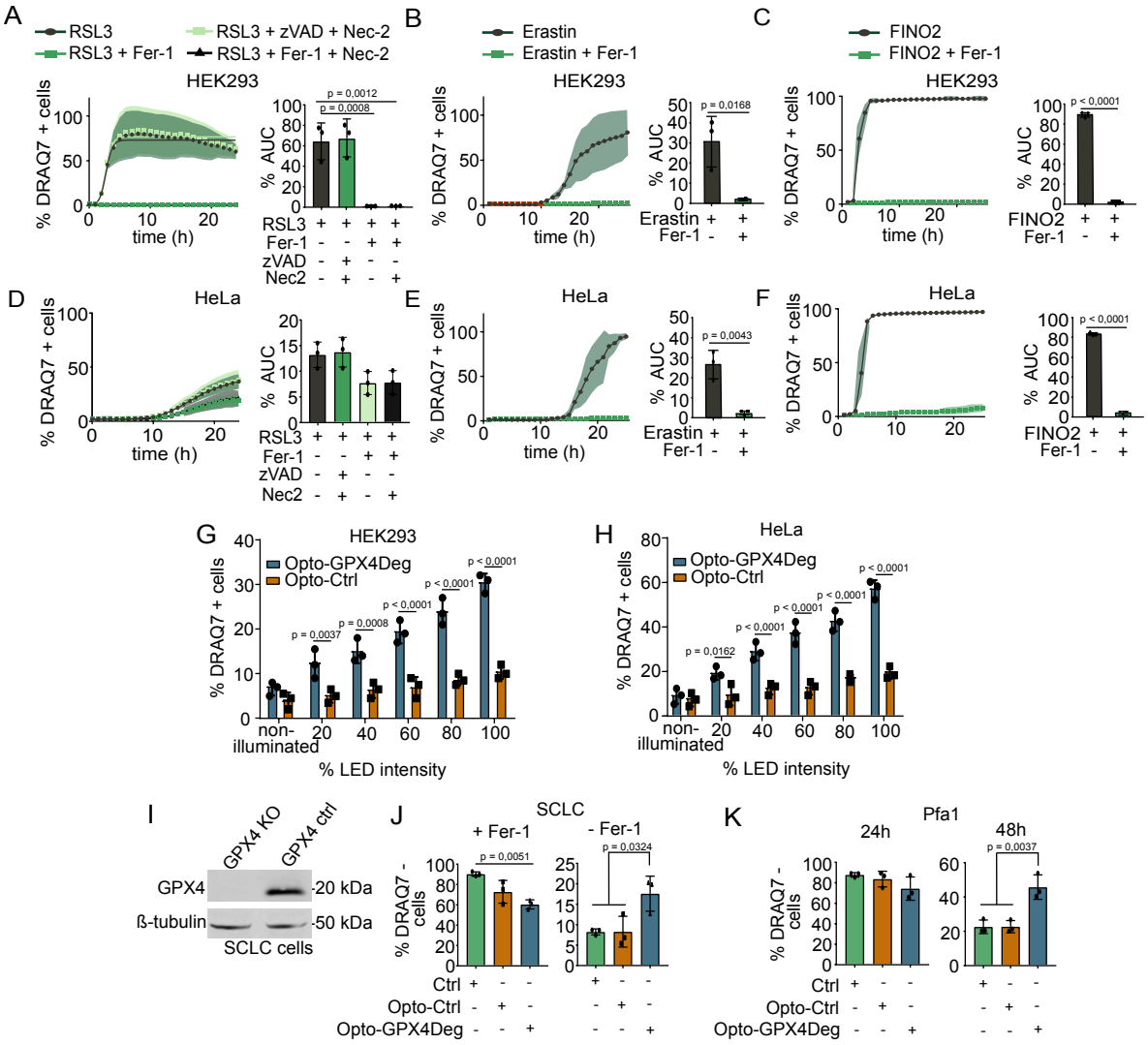

Fig. S1: Analysis of the Opto-GPX4Deg tool. (A-F) Kinetics of cell death of HeLa or HEK293 cell treated as indicated with the following drug concentrations: 4 µM RSL3, 4 µM Fer-1, 10µM zVAD, 10 µM Nec-2, 20 µM Erastin, 30 µM FINO2. Cell death was assessed by DRAQ7 staining utilizing an IncuCyte S3. %AUC of different treatments. Statistical analysis by parametric t-test or one-way ANOVA corrected for multiple comparisons using Tukey's multiple comparison test. Exact p-values are shown. All experiments were performed with three independent biological replicates (n=3). Values as mean ± SD. **(G, H)** Illumination intensity induces cell death in a proportional manner in Opto-GPX4Deg expressing cells, but not in Opto-Ctrl. Experimental design as in Fig. 1 except that a gradient of 465 nm LED intensities was used. Statistical analysis by multiple t-tests using the Holm-Sidak method. Exact p-values are shown. All experiments were performed with three independent biological replicates (n=3). Values as mean ± SD. **(I-K)** Opto-GPX4Deg retains partial GPX4 activity. **(I)** Representative WB proving that SCLC GPX4 KO cells are GPX4 deficient. **(J)** % DRAQ7 negative GPX4 KO SCLC cells transfected or not with Opto-GPX4Deg or Opto-Ctrl and treated or not with 5 µM Fer-1. Statistical analysis by one-way ANOVA corrected for multiple comparisons using Tukey's multiple comparison test. Exact p-values are shown. All

experiments were performed with three independent biological replicates (n=3). Values as mean ± SD. **(K)** Tamoxifen inducible Pfa1 GPX4 KO cells transfected with Opto-GPX4Deg exhibit increased viability compared to non-transfected cells 48h post-treatment with 1 µM tamoxifen. Statistical analysis by one-way ANOVA corrected for multiple comparisons using Tukey's multiple comparison test. Exact p-values are shown. All experiments were performed with three independent biological replicates (n=3). Values are displayed as mean ± SD.

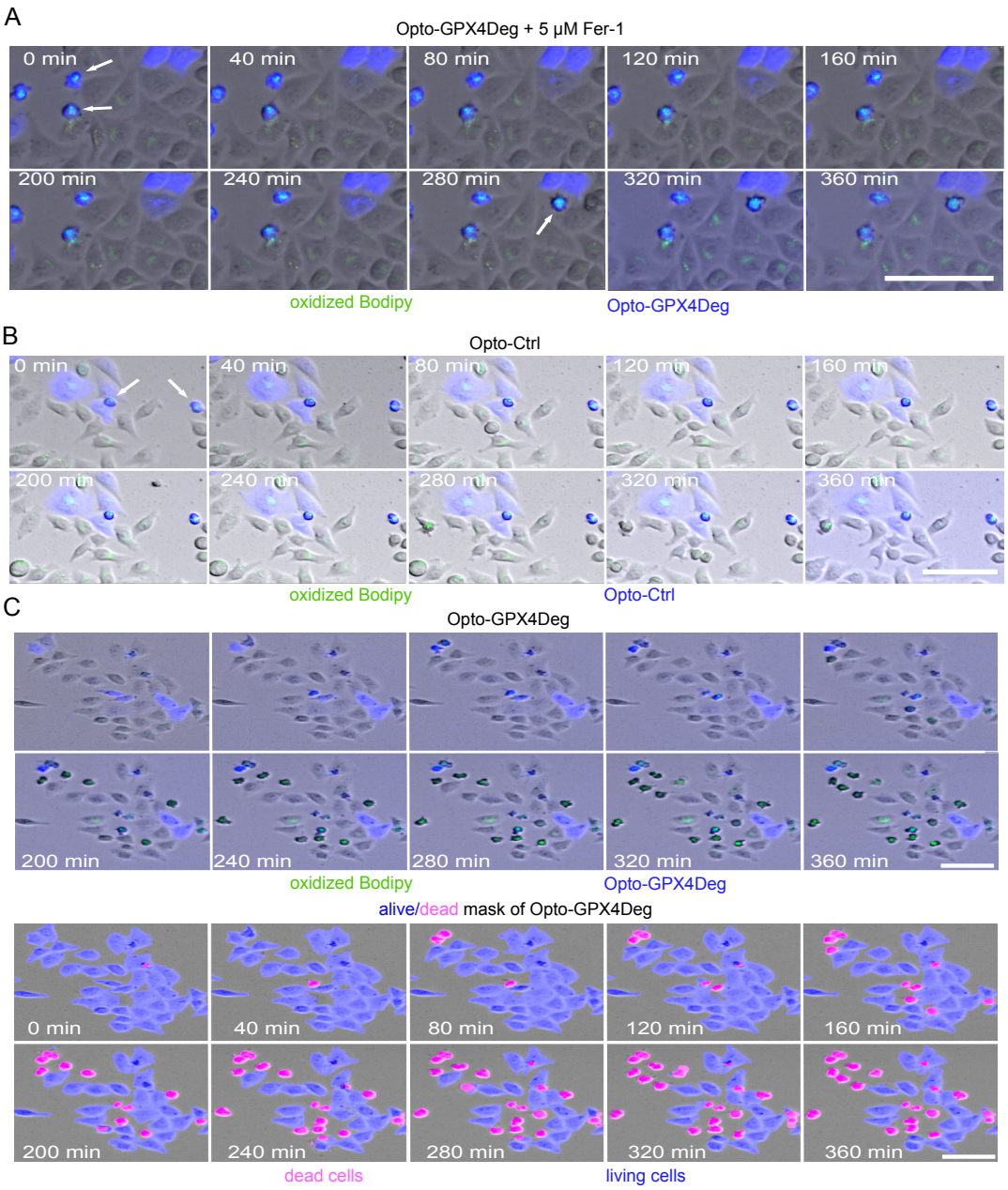

Fig. S2: Fer-1 treatment rescues cell death propagation to neighboring cells. (A,B) C11-Bodipy oxidation (green) and cell death time series for the indicated conditions. The blue signal indicates Opto-GPX4Deg or Opto-Ctrl expression. White arrows indicate dead, oxidized C11-Bodipy positive cells, whereas black arrows indicate dead, oxidized C11-Bodipy negative cells. Scale bar, 100 µm. **(C)** AI-derived alive/dead mask enables the quantitative analysis of cell death in microscopy images. Upper panel, the blue signal indicates Opto-GPX4Deg expression, green signal indicates C11-Bodipy oxidation. Lower panel, cell death detection by AI-based software. Living cells are indicated in blue and dead cells in pink. Scale bar, 100 µm.

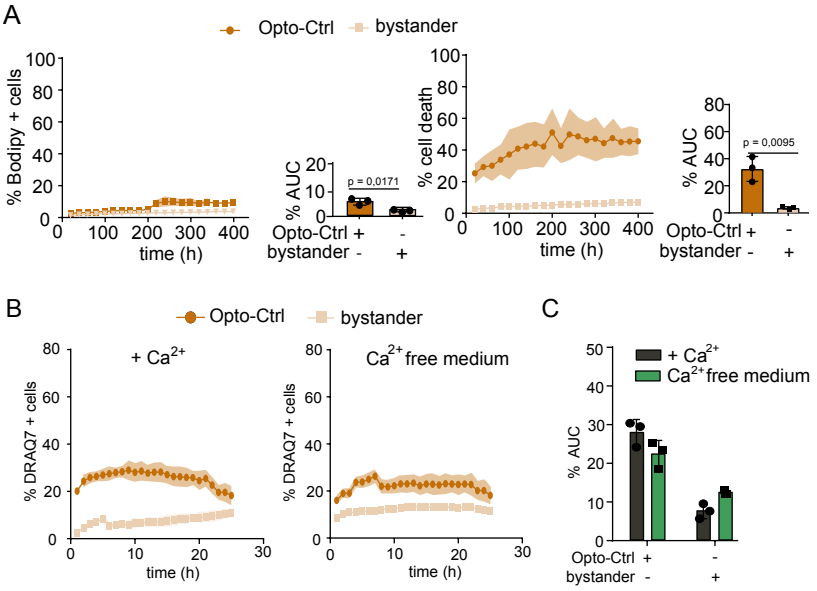

Fig. S3: Control conditions for assessing lipid peroxidation and cell death kinetics. (A) Quantification of C11-Bodipy oxidation and cell death kinetics of cells transfected with Opto-Ctrl and treated or not with 5 µM Fer-1. C11-Bodipy positive cells (left) and cell death (right) were quantified using custom-made software. %AUC for indicated conditions. Statistical analysis by parametric t-test. **(B,C)** Effect of calcium on ferroptosis sensitivity. **(B)** %DRAQ7 positive cells over time for indicated cell populations with or without extracellular Ca2+. **(C)** %AUC for populations in **(B)**. Statistical analysis by one-way ANOVA corrected for multiple comparisons using Tukey's multiple comparison test. Exact p-values are shown. All experiments were performed with three independent biological replicates (n=3). Values mean ± SD.

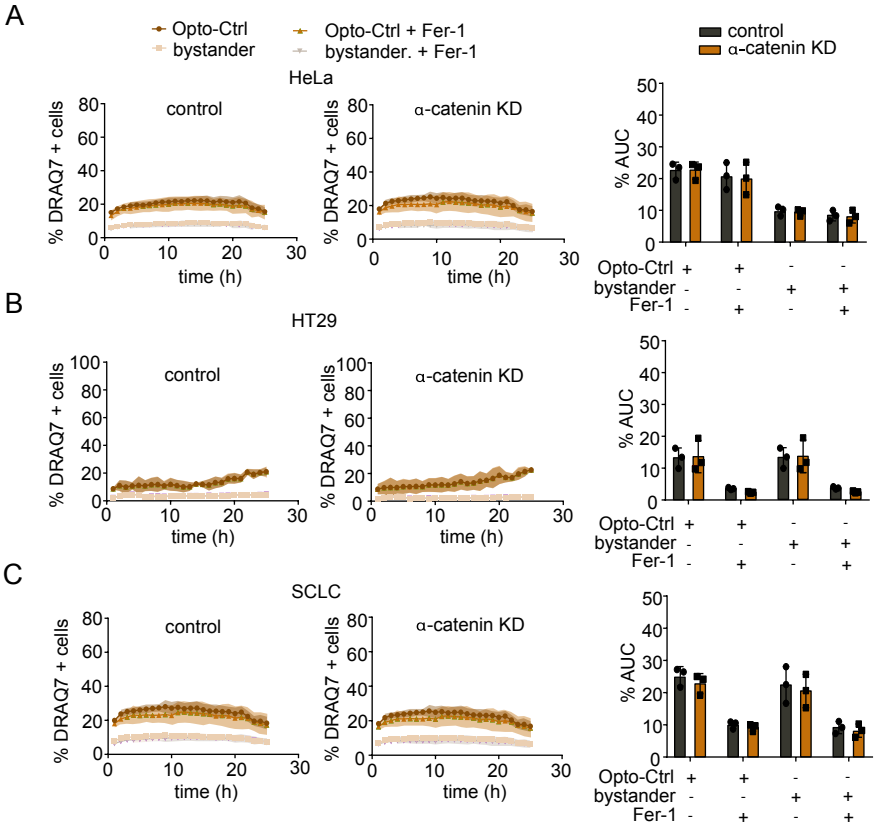

Fig. S4: Controls for α-catenin KD experiments. (A-C) Kinetics of cell death of activated Opto-Ctrl HeLa **(A)**, HT-29 **(B)** or SCLC **(C)** cells transfected with siRNA against α-catenin or scrambled siRNA and treated or not with 5 µM Fer-1. %AUC for the indicated conditions. Statistical analysis by one-way ANOVA corrected for multiple comparisons using Tukey's multiple comparison test. Exact p-values are shown. All experiments were performed with three independent biological replicates (n=3). Values mean ± SD.

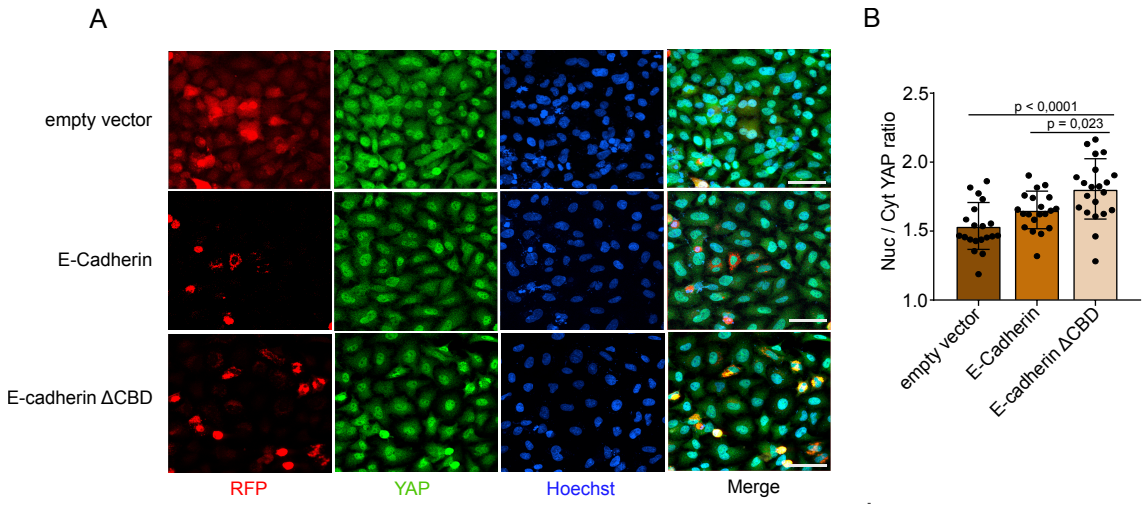

Fig. S5: Analysis of YAP activation. (A) Representative immunofluorescence images of YAP translocation to the nucleus in HeLa cells transfected with empty vector, E-cadherin or E-cadherin. Red, construct expression; green, YAP; blue, Hoechst as nuclear staining. **(F)** Quantification of the nucleus/cytosol (Nuc/Cyt) YAP ratio for the indicated conditions. Statistical analysis by one-way ANOVA corrected for multiple comparisons using Tukey's multiple comparison test. Exact p-values are shown. All experiments were performed with three independent biological replicates (n=3). Values as mean ± SD.

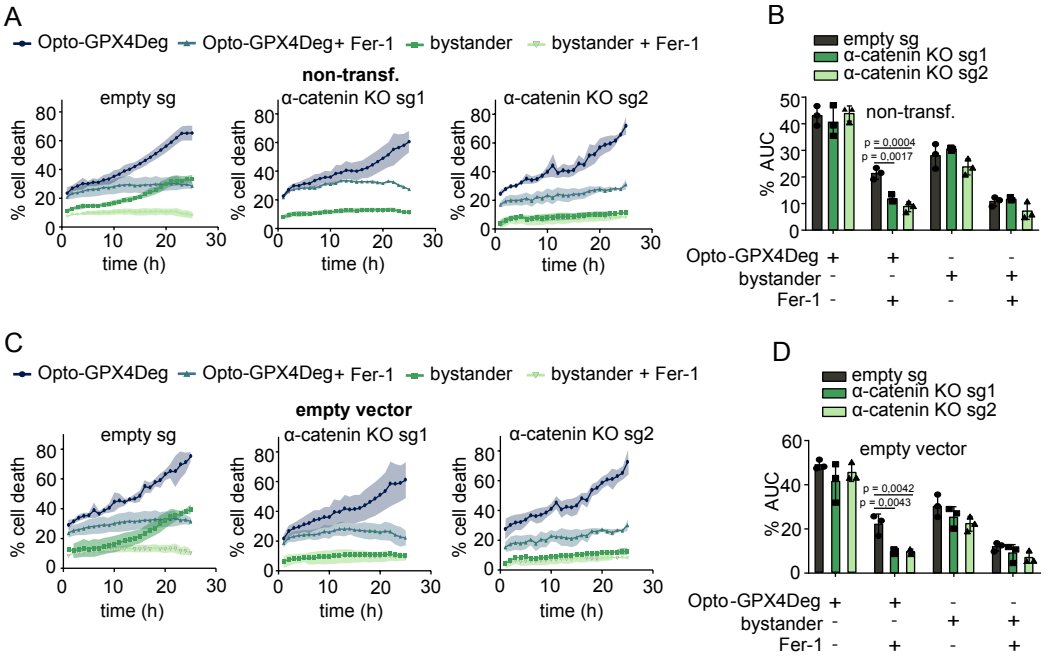

Fig. S6: HeLa α-catenin KO cells exhibit no ferroptosis propagation. (A,C) Cell death kinetics for activated Opto-GPX4Deg and bystander α-catenin KO HeLa clones (sg1, sg2) or CRISPR control (empty sg) not transfected or transfected with empty vector, treated or not with 5 µM Fer-1. **(B, D)** %AUC for the indicated cell populations. Statistical analysis by one-way ANOVA corrected for multiple comparisons using Tukey's multiple comparison test. Exact p-values are shown. All experiments were performed with three independent biological replicates (n=3). Values as mean ± SD.

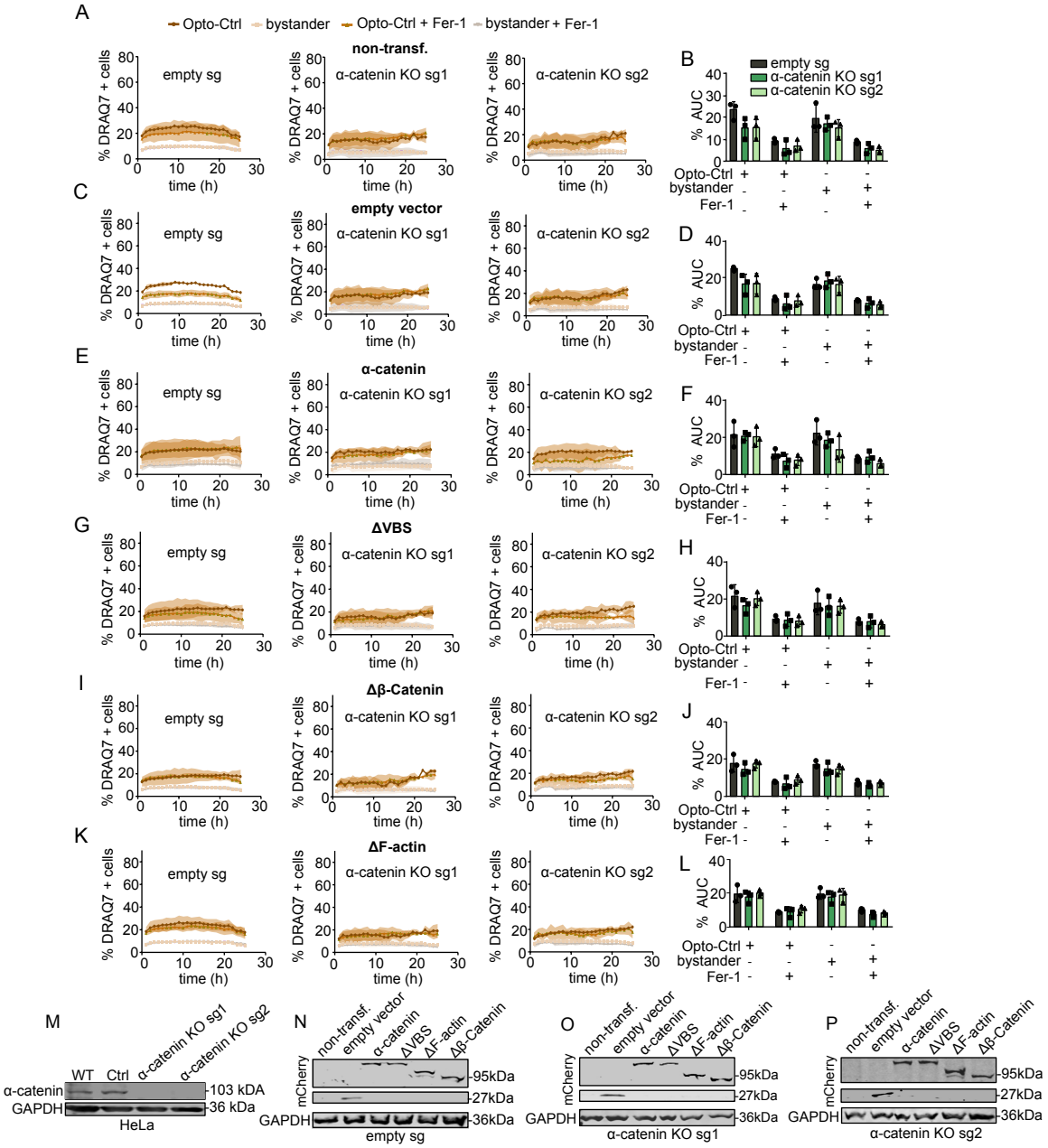

Fig. S7: Control conditions for α-catenin reconstitution experiments in α-catenin KO HeLa cells. (A, C, E, G, I, K) Cell death kinetics for activated Opto-Ctrl and bystander α-catenin KO HeLa clones (sg1, sg2) or CRISPR control (empty sg) not reconstituted with exogenous WT or mutant α-catenin treated or not with 5 μM Fer-1. (B, D, F, H, J, L) %AUC for the indicated cell populations. Statistical analysis by one-way ANOVA corrected for multiple comparisons using Tukey's multiple comparison test. Exact p-values are shown. All experiments were performed with three independent biological replicates (n=3). Values as mean ± SD. (M) WB of HeLa α-catenin KO cells. (N-P) WB showing comparable reconstitution levels for the indicated constructs.

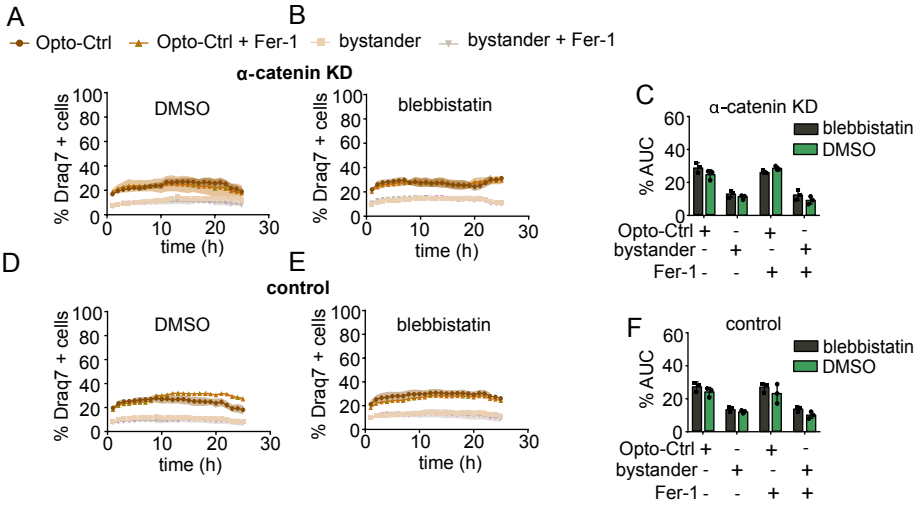

Fig. S8: Control conditions for blebbistatin experiment. Cell death kinetics for activated Opto-Ctrl and bystander HeLa cells transfected with siRNA against α-catenin **(A,B)** or scrambled siRNA **(D,E)** (control), and treated or not with 5 µM Fer-1 and/or 10 µM blebbistatin. **(C,F)** %AUC for the indicated populations in **(A,B,D,E)**. Statistical analysis by one-way ANOVA corrected for multiple comparisons using Tukey's multiple comparison test. Exact p-values are shown. All experiments were performed with three independent biological replicates (n=3). Values as mean ± SD.

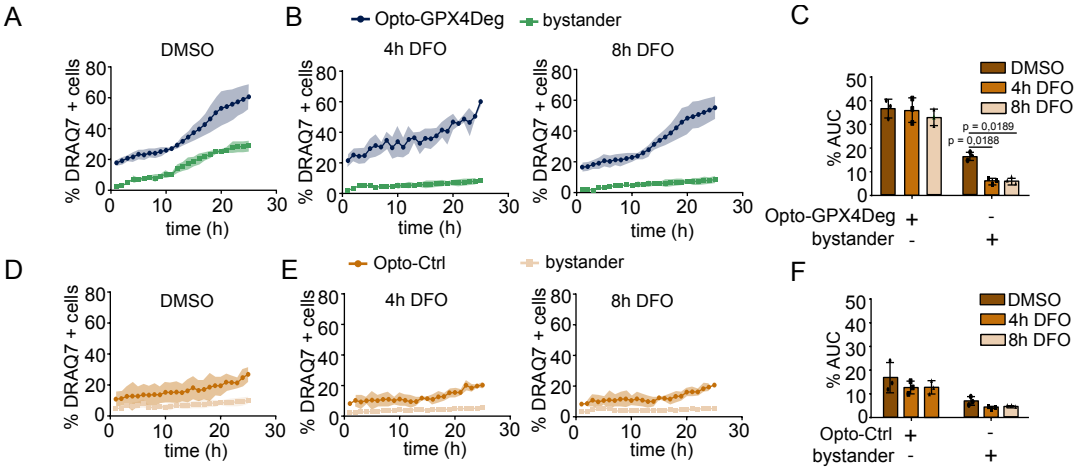

Fig. S9: DFO does not interfere with the intrinsic ferroptosis sensitivity of cells through potential endosomal uptake and accumulation. Cell death kinetics for activated Opto-GPX4Deg **(A,B)** or Opto-Ctrl HeLa **(D,E)** cells for 4h or 8h hours pretreatment with DMSO or 100 µM DFO. **(C,F)** %AUC for the indicated cell populations. Statistical analysis by one-way ANOVA corrected for multiple comparisons using Tukey's multiple comparison test. Exact p-values are shown. All experiments were performed with three independent biological replicates (n=3). Values as mean ± SD.

References

1. Dixon, S. J. *et al.* Ferroptosis: an iron-dependent form of nonapoptotic cell death. *Cell* **149**, 1060–1072 (2012).
2. Conrad, M. & Pratt, D. A. The chemical basis of ferroptosis. *Nat Chem Biol* **15**, 1137–1147 (2019).
3. Galluzzi, L. *et al.* Molecular mechanisms of cell death: recommendations of the Nomenclature Committee on Cell Death 2018. *Cell Death Differ* **25**, 486–541 (2018).
4. Ramos, S., Hartenian, E., Santos, J. C., Walch, P. & Broz, P. NINJ1 induces plasma membrane rupture and release of damage-associated molecular pattern molecules during ferroptosis. *EMBO J* 1–23 (2024).
5. Friedmann Angeli, J. P. *et al.* Inactivation of the ferroptosis regulator Gpx4 triggers acute renal failure in mice. *Nat Cell Biol* **16**, 1180–1191 (2014).
6. Skouta, R. *et al.* Ferrostatins inhibit oxidative lipid damage and cell death in diverse disease models. *J Am Chem Soc* **136**, 4551–4556 (2014).
7. Dixon, S. J. & Olzmann, J. A. The cell biology of ferroptosis. *Nat Rev Mol Cell Biol* 1–19 (2024).
8. Lei, G., Zhuang, L. & Gan, B. Targeting ferroptosis as a vulnerability in cancer. *Nat Rev Cancer* 1–16 (2022).
9. Liang, D. *et al.* Ferroptosis surveillance independent of GPX4 and differentially regulated by sex hormones. *Cell* **186**, 2748–2764 (2023).
10. Mishima, E. *et al.* DHODH inhibitors sensitize to ferroptosis by FSP1 inhibition. *Nature* **619**, E9–E18 (2023).
11. Li, Y. *et al.* 7-Dehydrocholesterol dictates ferroptosis sensitivity. *Nature* **626**, 411–418 (2024).
12. Zhou, Y. *et al.* Ferroptosis and Its Potential Role in the Nervous System Diseases. *J Inflamm Res* **15**, 1555–1574 (2022).
13. Hu, W. *et al.* Ferroptosis and its role in chronic diseases. *Cells* **11**, 2040 (2022).
14. Leng, Y., Luo, X., Yu, J., Jia, H. & Yu, B. Ferroptosis: a potential target in cardiovascular disease. *Front Cell Dev Biol* **9**, 3962 (2022).
15. Ou, M. *et al.* Role and mechanism of ferroptosis in neurological diseases. *Mol Metab* 101502 (2022).
16. Lin, Y. *et al.* The multifaceted role of ferroptosis in kidney diseases. *Chem Biol Interact* **365**, 110107 (2022).
17. Jiang, X., Stockwell, B. R. & Conrad, M. Ferroptosis: mechanisms, biology and role in disease. *Nat Rev Mol Cell Biol* **22**, 266–282 (2021).
18. Eagle, H. Nutrition needs of mammalian cells in tissue culture. *Science (1979)* **122**, 501–504 (1955).
19. Eagle, H., Piez, K. A. & Oyama, V. I. The biosynthesis of cystine in human cell cultures. *Journal of Biological Chemistry* **236**, 1425–1428 (1961).
20. Coltorti, M., RITIS, D. E. & Giusti, G. Enzymatic mechanisms of transsulfuration in biology and clinical practice. *G Clin Med* **37**, 285–323 (1956).
21. Golberg, L. & Smith, J. P. Changes associated with the accumulation of excessive amounts of iron in certain organs of the rat. *Br J Exp Pathol* **39**, 59 (1958).
22. Ursini, F., Maiorino, M., Valente, M., Ferri, L. & Gregolin, C. Purification from pig liver of a protein which protects liposomes and biomembranes from peroxidative degradation and exhibits glutathione peroxidase activity on phosphatidylcholine hydroperoxides. *Biochimica et Biophysica Acta (BBA)-Lipids and Lipid Metabolism* **710**, 197–211 (1982).

23. Sato, H., Tamba, M., Ishii, T. & Bannai, S. Cloning and expression of a plasma membrane cystine/glutamate exchange transporter composed of two distinct proteins. *Journal of Biological Chemistry* **274**, 11455–11458 (1999).
24. Tan, S., Schubert, D. & Maher, P. Oxytosis: a novel form of programmed cell death. *Curr Top Med Chem* **1**, 497–506 (2001).
25. Dolma, S., Lessnick, S. L., Hahn, W. C. & Stockwell, B. R. Identification of genotype-selective antitumor agents using synthetic lethal chemical screening in engineered human tumor cells. *Cancer Cell* **3**, 285–296 (2003).
26. Yang, W. S. & Stockwell, B. R. Synthetic lethal screening identifies compounds activating iron-dependent, nonapoptotic cell death in oncogenic-RAS-harboring cancer cells. *Chem Biol* **15**, 234–245 (2008).
27. Seiler, A. *et al.* Glutathione peroxidase 4 senses and translates oxidative stress into 12/15-lipoxygenase dependent-and AIF-mediated cell death. *Cell Metab* **8**, 237–248 (2008).
28. Banjac, A. *et al.* The cystine/cysteine cycle: a redox cycle regulating susceptibility versus resistance to cell death. *Oncogene* **27**, 1618–1628 (2008).
29. Pope, L. E. & Dixon, S. J. Regulation of ferroptosis by lipid metabolism. *Trends Cell Biol* (2023).
30. Liang, D., Minikes, A. M. & Jiang, X. Ferroptosis at the intersection of lipid metabolism and cellular signaling. *Mol Cell* **82**, 2215–2227 (2022).
31. Li, Z., Lange, M., Dixon, S. J. & Olzmann, J. A. Lipid quality control and ferroptosis: from concept to mechanism. *Annu Rev Biochem* **93**, (2023).
32. Wenzel, S. E. *et al.* PEBP1 wardens ferroptosis by enabling lipoxygenase generation of lipid death signals. *Cell* **171**, 628–641 (2017).
33. Dixon, S. J. & Pratt, D. A. Ferroptosis: A flexible constellation of related biochemical mechanisms. *Mol Cell* **83**, 1030–1042 (2023).
34. Pedrera, L. *et al.* Ferroptotic pores induce Ca2+ fluxes and ESCRT-III activation to modulate cell death kinetics. *Cell Death Differ* **28**, 1644–1657 (2021).
35. Hirata, Y. *et al.* Lipid peroxidation increases membrane tension, Piezo1 gating, and cation permeability to execute ferroptosis. *Current Biology* **33**, 1282–1294 (2023).
36. Wiernicki, B. *et al.* Excessive phospholipid peroxidation distinguishes ferroptosis from other cell death modes including pyroptosis. *Cell Death Dis* **11**, 1–11 (2020).
37. Yin, H., Xu, L. & Porter, N. A. Free radical lipid peroxidation: mechanisms and analysis. *Chem Rev* **111**, 5944–5972 (2011).
38. Conrad, M. & Pratt, D. A. The chemical basis of ferroptosis. *Nat Chem Biol* **15**, 1137–1147 (2019).
39. Rouzer, C. A. & Marnett, L. J. Mechanism of free radical oxygenation of polyunsaturated fatty acids by cyclooxygenases. *Chem Rev* **103**, 2239–2304 (2003).
40. Mascayano, C., Núñez, G., Acevedo, W. & Rezende, M. C. Binding of arachidonic acid and two flavonoid inhibitors to human 12-and 15-lipoxygenases: a steered molecular dynamics study. *J Mol Model* **16**, 1039–1045 (2010).
41. Pedrera, L. *et al.* Ferroptotic pores induce Ca2+ fluxes and ESCRT-III activation to modulate cell death kinetics. *Cell Death Differ* **28**, 1644–1657 (2021).
42. Dai, E., Meng, L., Kang, R., Wang, X. & Tang, D. ESCRT-III–dependent membrane repair blocks ferroptosis. *Biochem Biophys Res Commun* **522**, 415–421 (2020).
43. Gong, Y.-N. *et al.* ESCRT-III acts downstream of MLKL to regulate necroptotic cell death and its consequences. *Cell* **169**, 286–300 (2017).
44. Rühl, S. *et al.* ESCRT-dependent membrane repair negatively regulates pyroptosis downstream of GSDMD activation. *Science (1979)* **362**, 956–960 (2018).
45. Roveri, A., Maiorino, M., Nisii, C. & Ursini, F. Purification and characterization of phospholipid hydroperoxide glutathione peroxidase from rat testis mitochondrial

membranes. *Biochimica et Biophysica Acta (BBA)-Protein Structure and Molecular Enzymology* **1208**, 211–221 (1994).
46. Yang, W. S. *et al.* Regulation of ferroptotic cancer cell death by GPX4. *Cell* **156**, 317–331 (2014).
47. Forman, H. J., Zhang, H. & Rinna, A. Glutathione: overview of its protective roles, measurement, and biosynthesis. *Mol Aspects Med* **30**, 1–12 (2009).
48. Koppula, P., Zhang, Y., Zhuang, L. & Gan, B. Amino acid transporter SLC7A11/xCT at the crossroads of regulating redox homeostasis and nutrient dependency of cancer. *Cancer Commun* **38**, 1–13 (2018).
49. Feng, H. & Stockwell, B. R. Unsolved mysteries: How does lipid peroxidation cause ferroptosis? *PLoS Biol* **16**, e2006203 (2018).
50. Viswanathan, V. S. *et al.* Dependency of a therapy-resistant state of cancer cells on a lipid peroxidase pathway. *Nature* **547**, 453–457 (2017).
51. Ingold, I. *et al.* Selenium utilization by GPX4 is required to prevent hydroperoxide-induced ferroptosis. *Cell* **172**, 409–422 (2018).
52. Li, Z. *et al.* Ribosome stalling during selenoprotein translation exposes a ferroptosis vulnerability. *Nat Chem Biol* **18**, 751–761 (2022).
53. Greenough, M. A. *et al.* Selective ferroptosis vulnerability due to familial Alzheimer's disease presenilin mutations. *Cell Death Differ* **29**, 2123–2136 (2022).
54. Alborzinia, H. *et al.* LRP8-mediated selenocysteine uptake is a targetable vulnerability in MYCN-amplified neuroblastoma. *EMBO Mol Med* **15**, e18014 (2023).
55. Carlisle, A. E. *et al.* Selenium detoxification is required for cancer-cell survival. *Nat Metab* **2**, 603–611 (2020).
56. Doll, S. *et al.* ACSL4 dictates ferroptosis sensitivity by shaping cellular lipid composition. *Nat Chem Biol* **13**, 91–98 (2017).
57. Dixon, S. J. *et al.* Human haploid cell genetics reveals roles for lipid metabolism genes in nonapoptotic cell death. *ACS Chem Biol* **10**, 1604–1609 (2015).
58. Zou, Y. *et al.* A GPX4-dependent cancer cell state underlies the clear-cell morphology and confers sensitivity to ferroptosis. *Nat Commun* **10**, 1617 (2019).
59. Kim, J.-H., Lewin, T. M. & Coleman, R. A. Expression and characterization of recombinant rat acyl-CoA synthetases 1, 4, and 5: selective inhibition by triacsin C and thiazolidinediones. *Journal of Biological Chemistry* **276**, 24667–24673 (2001).
60. Li, Y. *et al.* Ischemia-induced ACSL4 activation contributes to ferroptosis-mediated tissue injury in intestinal ischemia/reperfusion. *Cell Death Differ* **26**, 2284–2299 (2019).
61. Bersuker, K. *et al.* The CoQ oxidoreductase FSP1 acts parallel to GPX4 to inhibit ferroptosis. *Nature* **575**, 688–692 (2019).
62. Doll, S. *et al.* FSP1 is a glutathione-independent ferroptosis suppressor. *Nature* **575**, 693–698 (2019).
63. Mishima, E. *et al.* A non-canonical vitamin K cycle is a potent ferroptosis suppressor. *Nature* **608**, 778–783 (2022).
64. Kraft, V. A. N. *et al.* GTP cyclohydrolase 1/tetrahydrobiopterin counteract ferroptosis through lipid remodeling. *ACS Cent Sci* **6**, 41–53 (2019).
65. Soula, M. *et al.* Metabolic determinants of cancer cell sensitivity to canonical ferroptosis inducers. *Nat Chem Biol* **16**, 1351–1360 (2020).
66. Jakaria, M., Belaidi, A. A., Bush, A. I. & Ayton, S. Vitamin A metabolites inhibit ferroptosis. *Biomedicine & Pharmacotherapy* **164**, 114930 (2023).
67. Freitas, F. P. *et al.* 7-Dehydrocholesterol is an endogenous suppressor of ferroptosis. *Nature* **626**, 401–410 (2024).
68. Qiu, B. *et al.* Phospholipids with two polyunsaturated fatty acyl tails promote ferroptosis. *Cell* (2024).

69. Morgan, P. K. *et al.* A lipid atlas of human and mouse immune cells provides insights into ferroptosis susceptibility. *Nat Cell Biol* 1–15 (2024).
70. Ma, X. *et al.* CD36-mediated ferroptosis dampens intratumoral CD8+ T cell effector function and impairs their antitumor ability. *Cell Metab* **33**, 1001–1012 (2021).
71. Kagan, V. E. *et al.* Oxidized arachidonic and adrenic PEs navigate cells to ferroptosis. *Nat Chem Biol* **13**, 81–90 (2017).
72. Lee, H. *et al.* Energy-stress-mediated AMPK activation inhibits ferroptosis. *Nat Cell Biol* **22**, 225–234 (2020).
73. Floros, K. V *et al.* MYCN-amplified neuroblastoma is addicted to iron and vulnerable to inhibition of the system Xc-/glutathione axis. *Cancer Res* **81**, 1896–1908 (2021).
74. Zhang, D.-L., Ghosh, M. C. & Rouault, T. A. The physiological functions of iron regulatory proteins in iron homeostasis-an update. *Front Pharmacol* **5**, 92341 (2014).
75. Andrews, N. C. & Schmidt, P. J. Iron homeostasis. *Annu. Rev. Physiol.* **69**, 69–85 (2007).
76. Hou, W. *et al.* Autophagy promotes ferroptosis by degradation of ferritin. *Autophagy* **12**, 1425–1428 (2016).
77. Gao, M. *et al.* Ferroptosis is an autophagic cell death process. *Cell Res* **26**, 1021–1032 (2016).
78. Gao, M., Monian, P., Quadri, N., Ramasamy, R. & Jiang, X. Glutaminolysis and transferrin regulate ferroptosis. *Mol Cell* **59**, 298–308 (2015).
79. Tuo, Q. Z. *et al.* Tau-mediated iron export prevents ferroptotic damage after ischemic stroke. *Mol Psychiatry* **22**, 1520–1530 (2017).
80. Zhang, T. *et al.* ENO1 suppresses cancer cell ferroptosis by degrading the mRNA of iron regulatory protein 1. *Nat Cancer* **3**, 75–89 (2022).
81. Alvarez, S. W. *et al.* NFS1 undergoes positive selection in lung tumours and protects cells from ferroptosis. *Nature* **551**, 639–643 (2017).
82. Wu, J. *et al.* Intercellular interaction dictates cancer cell ferroptosis via NF2–YAP signalling. *Nature* **572**, 402–406 (2019).
83. Schneider, M. *et al.* Absence of glutathione peroxidase 4 affects tumor angiogenesis through increased 12/15-lipoxygenase activity. *Neoplasia* **12**, 254–263 (2010).
84. Wenz, C. *et al.* Cell–cell contacts protect against t-BuOOH-induced cellular damage and ferroptosis in vitro. *Arch Toxicol* **93**, 1265–1279 (2019).
85. Eagle, H. The sustained growth of human and animal cells in a protein-free environment. *Proceedings of the National Academy of Sciences* **46**, 427–432 (1960).
86. Pan, D. The hippo signaling pathway in development and cancer. *Dev Cell* **19**, 491–505 (2010).
87. Zhao, B., Lei, Q.-Y. & Guan, K.-L. The Hippo–YAP pathway: new connections between regulation of organ size and cancer. *Curr Opin Cell Biol* **20**, 638–646 (2008).
88. Co, H. K. C., Wu, C.-C., Lee, Y.-C. & Chen, S. Emergence of large-scale cell death through ferroptotic trigger waves. *Nature* 1–9 (2024).
89. Linkermann, A. *et al.* Synchronized renal tubular cell death involves ferroptosis. *Proceedings of the National Academy of Sciences* **111**, 16836–16841 (2014).
90. Riegman, M. *et al.* Ferroptosis occurs through an osmotic mechanism and propagates independently of cell rupture. *Nat Cell Biol* **22**, 1042–1048 (2020).
91. Kim, S. E. *et al.* Ultrasmall nanoparticles induce ferroptosis in nutrient-deprived cancer cells and suppress tumour growth. *Nat Nanotechnol* **11**, 977–985 (2016).
92. Ma, Y. *et al.* Laser-ignited Lipid peroxidation nanoamplifiers for strengthening tumor photodynamic therapy through aggravating ferroptotic propagation and sustainable high immunogenicity. *Small* **20**, 2306402 (2024).

93. Li, X. *et al.* Small extracellular vesicles delivering lncRNA WAC-AS1 aggravate renal allograft ischemia–reperfusion injury by inducing ferroptosis propagation. *Cell Death Differ* **30**, 2167–2186 (2023).
94. Zhang, Q. *et al.* PAFAH2 suppresses synchronized ferroptosis to ameliorate acute kidney injury. *Nat Chem Biol* 1–12 (2024).
95. Wang, X., Zhou, Y., Min, J. & Wang, F. Zooming in and out of ferroptosis in human disease. *Front Med* **17**, 173–206 (2023).
96. Kolar, K., Knobloch, C., Stork, H., Žnidarič, M. & Weber, W. OptoBase: a web platform for molecular optogenetics. *ACS Synth Biol* **7**, 1825–1828 (2018).
97. Emiliani, V. *et al.* Optogenetics for light control of biological systems. *Nature Reviews Methods Primers* **2**, 55 (2022).
98. Fork, R. L. Laser stimulation of nerve cells in Aplysia. *Science (1979)* **171**, 907–908 (1971).
99. Zemelman, B. V, Lee, G. A., Ng, M. & Miesenböck, G. Selective photostimulation of genetically chARGed neurons. *Neuron* **33**, 15–22 (2002).
100. Nagel, G. *et al.* Channelrhodopsin-1: a light-gated proton channel in green algae. *Science (1979)* **296**, 2395–2398 (2002).
101. Li, X. *et al.* Fast noninvasive activation and inhibition of neural and network activity by vertebrate rhodopsin and green algae channelrhodopsin. *Proceedings of the National Academy of Sciences* **102**, 17816–17821 (2005).
102. Nagel, G. *et al.* Light activation of channelrhodopsin-2 in excitable cells of Caenorhabditis elegans triggers rapid behavioral responses. *Current biology* **15**, 2279–2284 (2005).
103. Schroll, C. *et al.* Light-induced activation of distinct modulatory neurons triggers appetitive or aversive learning in Drosophila larvae. *Current biology* **16**, 1741–1747 (2006).
104. Adamantidis, A. R., Zhang, F., Aravanis, A. M., Deisseroth, K. & De Lecea, L. Neural substrates of awakening probed with optogenetic control of hypocretin neurons. *Nature* **450**, 420–424 (2007).
105. Douglass, A. D., Kraves, S., Deisseroth, K., Schier, A. F. & Engert, F. Escape behavior elicited by single, channelrhodopsin-2-evoked spikes in zebrafish somatosensory neurons. *Current biology* **18**, 1133–1137 (2008).
106. Han, X. *et al.* Millisecond-timescale optical control of neural dynamics in the nonhuman primate brain. *Neuron* **62**, 191–198 (2009).
107. Taslimi, A. *et al.* An optimized optogenetic clustering tool for probing protein interaction and function. *Nat Commun* **5**, 4925 (2014).
108. Shkarina, K. & Broz, P. Selective induction of programmed cell death using synthetic biology tools. in *Seminars in Cell & Developmental Biology* (Elsevier, 2023).
109. Röck, B. F., Shalaby, R. & García-Sáez, A. J. Pyroptosis Induction and Visualization at the Single-Cell Level Using Optogenetics. in *NLR Proteins: Methods and Protocols* 135–147 (Springer, 2023).
110. Kramer, M. M., Lataster, L., Weber, W. & Radziwill, G. Optogenetic approaches for the spatiotemporal control of signal transduction pathways. *Int J Mol Sci* **22**, 5300 (2021).
111. Bugaj, L. J., Choksi, A. T., Mesuda, C. K., Kane, R. S. & Schaffer, D. V. Optogenetic protein clustering and signaling activation in mammalian cells. *Nat Methods* **10**, 249–252 (2013).
112. Kramer, M. M., Lataster, L., Weber, W. & Radziwill, G. Optogenetic approaches for the spatiotemporal control of signal transduction pathways. *Int J Mol Sci* **22**, 5300 (2021).

113. Wend, S. *et al.* Optogenetic control of protein kinase activity in mammalian cells. *ACS Synth Biol* **3**, 280–285 (2014).
114. Lan, T.-H., He, L., Huang, Y. & Zhou, Y. Optogenetics for transcriptional programming and genetic engineering. *Trends in Genetics* **38**, 1253–1270 (2022).
115. Younas, T., Vidallon, M. L. P., Tabor, R. F. & He, L. Open–Closed Structure of Light-Responsive Protein LOV2 Regulates Its Molecular Interaction with a Binding Partner. *J Phys Chem Lett* **11**, 8647–8653 (2020).
116. Niopek, D., Wehler, P., Roensch, J., Eils, R. & Di Ventura, B. Optogenetic control of nuclear protein export. *Nat Commun* **7**, 10624 (2016).
117. Niopek, D. *et al.* Engineering light-inducible nuclear localization signals for precise spatiotemporal control of protein dynamics in living cells. *Nat Commun* **5**, 4404 (2014).
118. Cavanaugh, K. E., Staddon, M. F., Munro, E., Banerjee, S. & Gardel, M. L. RhoA mediates epithelial cell shape changes via mechanosensitive endocytosis. *Dev Cell* **52**, 152–166 (2020).
119. Nadjar, J. *et al.* Optogenetically controlled inflammasome activation demonstrates two phases of cell swelling during pyroptosis. *Sci Signal* **17**, eabn8003 (2024).
120. Shkarina, K. *et al.* Optogenetic activators of apoptosis, necroptosis, and pyroptosis. *Journal of Cell Biology* **221**, e202109038 (2022).
121. Repina, N. A. *et al.* Engineered illumination devices for optogenetic control of cellular signaling dynamics. *Cell Rep* **31**, (2020).
122. Li, Y. *et al.* Spatiotemporal control of TGF-β signaling with light. *ACS Synth Biol* **7**, 443–451 (2018).
123. Zalocusky, K. A., Fenno, L. E. & Deisseroth, K. Current challenges in optogenetics. *Optogenetics* 23–33 (2013).
124. Jang, S. K. *et al.* A segment of the 5'nontranslated region of encephalomyocarditis virus RNA directs internal entry of ribosomes during in vitro translation. *J Virol* **62**, 2636–2643 (1988).
125. Pelletier, J. & Sonenberg, N. Internal initiation of translation of eukaryotic mRNA directed by a sequence derived from poliovirus RNA. *Nature* **334**, 320–325 (1988).
126. Sun, W. *et al.* Light-induced protein degradation in human-derived cells. *Biochem Biophys Res Commun* **487**, 241–246 (2017).
127. Guinn, M. T. & Balázsi, G. Noise-reducing optogenetic negative-feedback gene circuits in human cells. *Nucleic Acids Res* **47**, 7703–7714 (2019).
128. Bugaj, L. J. & Lim, W. A. High-throughput multicolor optogenetics in microwell plates. *Nat Protoc* **14**, 2205–2228 (2019).
129. Thomas, O. S., Hörner, M. & Weber, W. A graphical user interface to design high-throughput optogenetic experiments with the optoPlate-96. *Nat Protoc* **15**, 2785–2787 (2020).
130. Godwin, W. C., Hoffmann, G. F., Gray, T. J. & Hughes, R. M. Imaging of morphological and biochemical hallmarks of apoptosis with optimized optogenetic tools. *Journal of Biological Chemistry* **294**, 16918–16929 (2019).
131. Yan, B. *et al.* Membrane Damage during Ferroptosis Is Caused by Oxidation of Phospholipids Catalyzed by the Oxidoreductases POR and CYB5R1. *Mol Cell* **81**, 355-369.e10 (2021).
132. Lawson, R. G. & Jurs, P. C. New index for clustering tendency and its application to chemical problems. *J Chem Inf Comput Sci* **30**, 36–41 (1990).
133. Kobielak, A. & Fuchs, E. α-catenin: at the junction of intercellular adhesion and actin dynamics. *Nat Rev Mol Cell Biol* **5**, 614–625 (2004).
134. Herr, K. J. *et al.* Loss of α-catenin elicits a cholestatic response and impairs liver regeneration. *Sci Rep* **4**, 6835 (2014).

135. Wu, X. *et al.* Co-loaded lapatinib/PAB by ferritin nanoparticles eliminated ECM-detached cluster cells via modulating EGFR in triple-negative breast cancer. *Cell Death Dis* **13**, 557 (2022).
136. Fouzder, C., Mukhuty, A., Mukherjee, S., Malick, C. & Kundu, R. Trigonelline inhibits Nrf2 via EGFR signalling pathway and augments efficacy of Cisplatin and Etoposide in NSCLC cells. *Toxicology in Vitro* **70**, 105038 (2021).
137. Martins, W. K. *et al.* Parallel damage in mitochondria and lysosomes is an efficient way to photoinduce cell death. *Autophagy* **15**, 259–279 (2019).
138. Bacellar, I. O. L. *et al.* Membrane damage efficiency of phenothiazinium photosensitizers. *Photochem Photobiol* **90**, 801–813 (2014).
139. Harayama, T. & Riezman, H. Understanding the diversity of membrane lipid composition. *Nat Rev Mol Cell Biol* **19**, 281–296 (2018).
140. Bayır, H. *et al.* Achieving life through death: redox biology of lipid peroxidation in ferroptosis. *Cell Chem Biol* **27**, 387–408 (2020).
141. Forcina, G. C. & Dixon, S. J. GPX4 at the crossroads of lipid homeostasis and ferroptosis. *Proteomics* **19**, 1800311 (2019).
142. Shah, R., Shchepinov, M. S. & Pratt, D. A. Resolving the role of lipoxygenases in the initiation and execution of ferroptosis. *ACS Cent Sci* **4**, 387–396 (2018).
143. Takeichi, M. Cadherins: a molecular family important in selective cell-cell adhesion. *Annu Rev Biochem* **59**, 237–252 (1990).
144. Li, Y. *et al.* Ischemia-induced ACSL4 activation contributes to ferroptosis-mediated tissue injury in intestinal ischemia/reperfusion. *Cell Death Differ* **26**, 2284–2299 (2019).
145. Li, W. *et al.* Ferroptotic cell death and TLR4/Trif signaling initiate neutrophil recruitment after heart transplantation. *J Clin Invest* **129**, 2293–2304 (2019).
146. Fang, X. *et al.* Ferroptosis as a target for protection against cardiomyopathy. *Proceedings of the National Academy of Sciences* **116**, 2672–2680 (2019).
147. Gao, M., Monian, P., Quadri, N., Ramasamy, R. & Jiang, X. Glutaminolysis and transferrin regulate ferroptosis. *Mol Cell* **59**, 298–308 (2015).
148. DeGregorio-Rocasolano, N., Martí-Sistac, O. & Gasull, T. Deciphering the iron side of stroke: neurodegeneration at the crossroads between iron dyshomeostasis, excitotoxicity, and ferroptosis. *Front Neurosci* 85 (2019).
149. Ma, Y. *et al.* Laser-ignited Lipid peroxidation nanoamplifiers for strengthening tumor photodynamic therapy through aggravating ferroptotic propagation and sustainable high immunogenicity. *Small* **20**, 2306402 (2024).
150. Parker, J. B. *et al.* Chelating the valley of death: Deferoxamine's path from bench to wound clinic. *Front Med (Lausanne)* **10**, 1015711 (2023).
151. Tu, H. *et al.* Combination of ponatinib with deferoxamine synergistically mitigates ischemic heart injury via simultaneous prevention of necroptosis and ferroptosis. *Eur J Pharmacol* **898**, 173999 (2021).
152. Gao, M., Monian, P., Quadri, N., Ramasamy, R. & Jiang, X. Glutaminolysis and Transferrin Regulate Ferroptosis. *Mol Cell* **59**, 298–308 (2015).
153. Yang, L. *et al.* Deferoxamine treatment combined with sevoflurane postconditioning attenuates myocardial ischemia-reperfusion injury by restoring HIF-1/BNIP3-mediated mitochondrial autophagy in GK rats. *Front Pharmacol* **11**, 6 (2020).
154. Freret, T. *et al.* Delayed administration of deferoxamine reduces brain damage and promotes functional recovery after transient focal cerebral ischemia in the rat. *European Journal of Neuroscience* **23**, 1757–1765 (2006).
155. Hanson, L. R. *et al.* Intranasal deferoxamine provides increased brain exposure and significant protection in rat ischemic stroke. *Journal of Pharmacology and Experimental Therapeutics* **330**, 679–686 (2009).

156. Chan, W. *et al.* Effect of iron chelation on myocardial infarct size and oxidative stress in ST-elevation–myocardial infarction. *Circ Cardiovasc Interv* **5**, 270–278 (2012).
157. Paraskevaidis, I. A. *et al.* Deferoxamine infusion during coronary artery bypass grafting ameliorates lipid peroxidation and protects the myocardium against reperfusion injury: immediate and long-term significance. *Eur Heart J* **26**, 263–270 (2005).
158. McLachlan, D. R. C. *et al.* Intramuscular desferrioxamine in patients with Alzheimer's disease. *The Lancet* **337**, 1304–1308 (1991).
159. Li, J. *et al.* Alpha-catenins control cardiomyocyte proliferation by regulating Yap activity. *Circ Res* **116**, 70–79 (2015).
160. Vorndran, M. R. H. & Roeck, B. F. Inconsistency Masks: Removing the Uncertainty from Input-Pseudo-Label Pairs. *arXiv preprint arXiv:2401.14387* (2024).
161. Bebber, C. M. *et al.* Ferroptosis response segregates small cell lung cancer (SCLC) neuroendocrine subtypes. *Nat Commun* **12**, 1–19 (2021).
162. Doll, S. *et al.* FSP1 is a glutathione-independent ferroptosis suppressor. *Nature* **575**, 693–698 (2019).
163. Hellmuth, C., Weber, M., Koletzko, B. & Peissner, W. Nonesterified fatty acid determination for functional lipidomics: comprehensive ultrahigh performance liquid chromatography–tandem mass spectrometry quantitation, qualification, and parameter prediction. *Anal Chem* **84**, 1483–1490 (2012).
164. prathmachowksey. https://github.com/prathmachowksey/Hopkins-Statistic-Clustering-Tendency.